Scuola di Dottorato di Matematica e Fisica

DOTTORATO DI RICERCA IN FISICA
XXVI CICLO

Search for effects of an electric dipole moment of the τ lepton with the *BaBar* experiment

Tesi presentata da:
Silvia Martellotti

Relatore interno:
prof. Filippo Ceradini

Relatore esterno:
dott. Giuseppe Finocchiaro

a Giancarlo

Contents

Introduction **2**

1 Electric Dipole Moment **6**
1.1 Lepton Dipole Moment 6
1.1.1 P and T symmetries violation 7
1.2 Diplole moment measurements 8
1.2.1 τ EDM measurements 9
1.3 τ EDM theoretical prediction 10
1.4 τ dipole moment formalism 11
1.5 τ EDM effect in τ-pairs production 13
1.5.1 $e^+e^- \to \tau^+\tau^-$ spin density 14

2 τ lepton EDM Measurement Method **20**
2.1 Optimal Observables 20
2.1.1 Observables for EDM 21
2.2 Calculation of the observables 23
2.2.1 Tau flight direction reconstruction 23
2.2.2 Recontruction of the τ spin vector 27
2.2.3 Observables estimate from experimental data 30
2.3 Modeling the EDM effect in the MC 32
2.4 EDM sensitivity 33

3 The *BABAR* Experiment **35**
3.1 The PEP-II Accelerator 35
3.2 The e^+e^- interaction 37
3.3 The *BABAR* Detector 38
3.3.1 The Silicon Vertex Tracker 40
3.3.2 The Drift Chamber 43
3.3.3 The Cherenkov Detector 46
3.3.4 The Electromagnetic Calorimeter 50
3.3.5 The Instrumented Flux Return 53

3.3.6 Trigger 55

4 Data sample and event selection **58**
4.1 Data and MC samples 58
4.2 Preselection 61
4.2.1 Tau QED Skim 1-1 61
4.3 Event reconstruction 64
4.3.1 Charged particle reconstruction 64
4.3.2 Particle identification criteria 65
4.3.3 Additional requirements 70
4.4 ROOT's Boosted Decision Tree (BDT) 72

5 Results **88**
5.1 Sample composition 88
5.2 Data-MC comparison 90
5.3 Tau momentum reconstruction 91
5.4 Tau Spin Vector reconstruction 93
5.5 Observable distributions 93
5.6 EDM sensitivity evaluation 95
5.7 EDM measurement 99
5.8 Systematic errors evaluation 100

Conclusions **101**

A Optimal Observables **103**
A.0.1 Comparision with a likelihood fit 105

B τ spin vector reconstruction formula **106**

C Boosted Decision Tree **111**

Bibliography **116**

Acknowledgment **117**

Introduction

The Standard Model (SM) of elementary particles is the theory that describes three of the four fundamental interactions (strong, weak and electromagnetic) in a coherent framework. This theory gives an excellent description of almoust all the main phenomena observed in particle physics. Nevertheless the SM is incomplete, since it does not account for some experimental evidences, such as the presence of dark matter, the fermion masses hierarchy, the quantitative asymmetry between matter and antimatter in the universe and the neutrino masses different from zero. The explanation of these unsolved questions requires an extension of the SM.

Many searches for experimental evidence of new physics are now underway in the high energy field, following new theories beyond the SM hypotheses. A hint of new physics can be searched for by studying CP violation in the leptonic sector. CP violation phenomena in the hadron sector can indeed occur in the SM via the presence of the single complex phase in the Cabibbo-Kobayashi-Maskawa quark mixing matrix, and has been experimentally confirmed. On the contrary, the SM prediction for CP violation in the lepton sector is negligibly small and has never been observed so far. However, in some extensions of the SM there are terms that explicitly violate CP. The presence of physics beyond the SM could introduce these effects at experimentally accessible levels, making observation of CP violation in the leptonic sector a clear evidence of new physics.

CP violation in the lepton sector can be parametrized at the leading order in a model independent way with a lepton dipole moment. In the classical definition, an electric dipole moment different from zero, due to an asymmetric charge spatial distribution, leads to a parity violation. Similarly, with a dipole moment hypotesis for the case of an elementary particle, we can introduce a parity violation in the system. This dipole is proportional to the spin, the only quantity that spatially characterizes an elementary particle like a fermion.

While the electric dipole moment of the electron and the muon have been extensively investigated in matter physics, the electric dipole moment (EDM)

of the τ lepton can be investigated only in high energy physics due to the τ very short lifetime. The current upper bound on the electric dipole moment of the τ is the less stringent among leptons. On the other hand, at the high energies scale, the large τ mass makes the τ the most sensitive lepton to possible contributions to chirality-flip terms violating CP that could come from new physics. In some models such effects are expected to be enhanced, since new bosons and Higgs strongly couple with heavy particles through quantum loop effects. A non observation of the dipole moment with greater sensitivity would provide new bounds to the theories beyond the SM.

The copious τ-pair production at the B-factories working at the $\Upsilon(4S)$ center of mass energy, allows for a detailed investigation on the CP-violation at the electromagnetic $\tau^+\tau^-$ production vertex. The best τ EDM bound was set by Belle experiment with an analysis of the differential cross section of the $e^+e^- \to \tau^+\tau^-$ process with a data sample of 30 fb^{-1}.

The aim of the work presented in this thesis is the search of the τ EDM with the *BABAR* experiment data. The full *on-peak BABAR* data sample, corresponding to 425 fb^{-1}, will be used. In this thesis a subsample of 101 fb^{-1} is analysed due to time costraints.

CP-violation tests in the reaction $e^+e^- \to \tau^+\tau^-$ require an analysis of the final state spin correlations. The τ EDM presence indeed modifies the spin density matrix of the differential cross section of this process. Because of the τ short life time, the τ spin vector must be reconstructed starting from the daughters momenta. To calculate the cross section spin density matrix the τ flight direction is also needed and must be reconstructed. The channel selected for the analysis of this thesis is the one in which both tau leptons decay via $\tau^\pm \to \pi^\pm\nu_\tau$. This decay is chosen because the two body kinematics provides the best constraint for the τ flight direction reconstruction and the spin vector reconstruction formula is rather simple.

The analysis observables are chosen following the *Optimal Observables* method proposed by Atwood and Soni to obtain the highest sensitivity on any small coupling that modifies the differential cross section of a process. For the τ EDM case, the observables are related to the spin density matrix elements of the differential cross section and their mean values are characterized by a linear correlation with the dipole moment. To extract the dipole moment value, the parameters of this correlation must be found. The dependency of the observable means on the EDM is deduced by setting different EDM values in a full MC simulation that takes into account all systematic and detector effects. Once this relation is known, the τ EDM can be extracted from the mean values of the *Optimal Observables* measured on data. The search for the τ EDM effects is a MC-based analysis.

In this thesis the τ EDM measurement procedure is diffusely illustrated,

the signal selection criteria are discussed, the data sample obtained is studied and preliminary results are reported.

In the first chapter a theoretical introdution on the lepton dipole moment is presented and the τ EDM effect on the differential cross section of the $e^+e^- \to \tau^+\tau^-$ process is analysed. The τ EDM measurements done so far and the theoretical expectations are discussed.

In the second chapter the τ EDM measurement method is illustrated by means of his application on an ideal, pure signal, Monte Carlo sample with no detector effect simulated. This MC sample has been utilized to test and verify the EDM measurement method with optimal observables of the previous searches. In particular, the newest Belle analysis algorithms have been proved. The spin recostruction formulae have been obtained again with theoretician help and validated. This preliminary study of an ideal MC sample allows to verify the validity of the τ EDM search method.

In the third chapter the main *BABAR* detector characteristics and performance are described.

In the fourth chapter the MC and Data samples used for the analysis are presented and the signal ($e^+e^- \to \tau^+\tau^- \to \pi^+\pi^-\nu_\tau\bar{\nu}_\tau$) selection procedure is discussed. The τ-pairs events are selected with the *BABAR* standard preselection, the $\tau^\pm \to \pi^\pm\nu_\tau$ decays are then selected with a cut based analysis followed by a Boosted Decision Tree Multivariate Analysis.

Finally, in the last chapter preliminary results are shown. The results obtained for the real and imaginary part of the τ EDM are: $Re(d_\tau) = (2.32 \pm 3.66) \times 10^{-17}$ e cm and $Im(d_\tau) = (0.61 \pm 1.12) \times 10^{-17}$ e cm . The measurement has a statystical sensitivity higher than the one previously reported by Belle. The systematic errors are under evaluation. The good data-MC agreement make us confident that the systematics do not exceed the statystical errors, so that the extension of the analysis to the full *BABAR* data sample available will improve results.

Chapter 1

Electric Dipole Moment

CP violation phenomena in the hadron sector can occur in the Standard Model (SM) via the presence of a single complex phase in the Cabibbo-Kobayashi-Maskawa (CKM) [1] quark mixing matrix. Violations have been experimentally confirmed at the B-Factories by the *BABAR* [2] and Belle [3] experiments in the last decade. On the contrary, CP-violation in the lepton sector has never been observed and the SM prediction for this violation is negligibly small. However, the presence of physics beyond the SM (BSM) could bring these effects to experimentally accessible levels: any observation of CP violation in this sector would be a clear evidence of new physics. In some models such effects are expected to be enhanced for the τ lepton due to its very large mass compared to other leptons, since new bosons and Higgs would strongly couple with heavy particles through quantum loop effects.

The leptonic T and CP-violation in the electromagnetic and weak interactions can be parametrized, at the leading order, with a dipole moment. In the *BABAR* experiment the τ electric dipole moment (EDM) effect at the electromagnetic vertex in the τ-pair production process can be investigated.

In this chapter, after a brief theoretical introduction on the lepton dipole moment, the contribution of the τ EDM in the $e^+e^- \to \tau^+\tau^-$ interaction will be considered in detail. Past measurements done so far and theoretical EDM predictions will be illustrated.

1.1 Lepton Dipole Moment

There is no experimental evidence that any elementary particle, nucleus, or atom possesses a permanent EDM. Nevertheless, experimental searches for EDMs and theoretical investigations of their possible magnitudes have attracted great interest for many years, and continue to do so. The observa-

tion of a non-zero EDM would directly reveal the violation of time reversal (T) invariance as well as parity (P). As we will show in the next section, the possible existence of EDMs is intimately connected to these fundamental symmetries.

In the framework of local quantum field theories the CPT theorem states that a system must be invariant under the simultaneous transformation of T and CP. If T is violated, CP is violated as well. Our understanding of the nature and origin of CP-violation, one of the most intriguing phenomena of particle physics, would be greatly enhanced by detection of CP-violation in new places, like the leptonic sector.

1.1.1 P and T symmetries violation

Let us show that a particle cannot possess a dipole moment unless P and T are violated. Classically, the electric dipole moment of a system is given by:

$$\vec{d} = \int \rho(\vec{r})\, \vec{r}\, d^3r, \tag{1.1}$$

where $\rho(\vec{r})$ is the electric charge density. If there is an asymmetric structure of the charge distribution, the EDM is different from zero. Let us consider an elementary particle of spin 1/2 and suppose that it has an electric dipole moment $\vec{d}$ as well as a magnetic dipole moment $\vec{\mu}$. In this case the electric dipole moment lies as the magnetic one along the spin direction because the spin is the only vector available to orient an elementary particle. Thus $\vec{d}$ must be proportional to the spin as

$$\vec{d} = d\vec{S}. \tag{1.2}$$

Therefore, we write the Hamiltonians H_M and H_E that describe the interaction of $\vec{\mu}$ with a magnetic field $\vec{B}$, and of $\vec{d}$ with an electric field $\vec{E}$, in the non relativistic limit, as:

$$H_M = -\vec{\mu} \cdot \vec{B} = -\mu\vec{\sigma} \cdot \vec{B}, \tag{1.3}$$

$$H_E = -\vec{d} \cdot \vec{E} = -d\vec{\sigma} \cdot \vec{E}, \tag{1.4}$$

where $\vec{\sigma}$ is the Pauli spin operator. Under a space inversion or P transformation, the axial vectors $\vec{\sigma}$ and $\vec{B}$ remain unchanged, but the polar vector $\vec{E}$ changes sign. Hence H_M is invariant under P, but H_E is not. Similarly, under a T transformation, $\vec{E}$ remains invariant, but the angular momentum like $\vec{\sigma}$ changes sign, as does $\vec{B}$, which is generated by electric currents. Hence, while H_M is invariant, H_E changes sign under P and T transformations.

The experimental discovery of CP-violation phenomena in weak interactions authorizes the hypothesis of the existence of a CP violating lepton dipole moment. The weak interaction could induce an electric dipole moment by means of corrections to the, CP conserving, electromagnetic interactions.

In the SM case, the dipole moment is generated only at very high order in the coupling constant (three hadronic current loops with CKM-phase effect). This opens a way to efficiently test many models: CP-odd observables related to EDM would give no appreciable effect from the Standard Model and any experimental signal should be identified with physics BSM.

1.2 Diplole moment measurements

Extensive searches have been made for the electric dipole moment of electron, muon and nucleons and stringent limits exist.

The basic method for the EDM measurement of electron, neutron and proton is to search for a shift of the nuclear-spin resonances using the Nuclear Magnetic Resonance Spectroscopy technique under an external electric field which generates an energy shift due to the interaction with the EDM. The electron EDM was searched using atomic-beam magnetic resonance of the atomic thallium [4], because in heavy paramagnetic atoms the electron EDM effect is expected to be enhanced by some factor due to a relativistic effect. The proton EDM was also searched from the shift of the thallium spin resonance in the electric field [5] . The neutron EDM bound was obtained by measuring the shift of the Larmor frequency of ultra-cold neutrons, in an electric field parallel to a highly uniform magnetic field [6]. The muon EDM instead was searched at the dedicated muon storage ring [7], observing the spin precession of a relativistic free muon in a magnetic field. If the muon possesses an EDM, the precession angular velocity is slightly modified because in the muon's rest frame there is not only a magnetic field, but also a motional E field to which the EDM is coupled.

	Experimental results (e cm)	SM prediction (e cm)
e	$(6.9 \pm 7.4) \times 10^{-28}$ [4]	$\sim 8 \times 10^{-41}$ [8, 9]
μ	$(3.7 \pm 3.4) \times 10^{-19}$ [7]	$\sim 1.6 \times 10^{-38}$ [8, 9]
n	$(-1.0 \pm 3.6) \times 10^{-26}$ [6]	$1.4 \times 10^{-33} \div 1.6 \times 10^{-31}$[10]
p	$(-3.7 \pm 6.3) \times 10^{-23}$ [5]	-

Table 1.1: Experimental results and SM predictions for the EDM of elecron, muon, neutron and proton.

All the results are consistent with a zero EDM. The current best EDM

values for e, μ, n and p and the relative SM predictions are listed in Table 1.1. Presently, the best EDM upper limit is the one of the electron. While the EDM of the electron and muon have been extensively investigated both in experiment and theory, the case of the τ is somewhat different.

1.2.1 τ EDM measurements

The τ dipole moment can only be investigated in high-energy physics. The τ lepton has a relatively high mass: this means that τ lepton physics is expected to be more sensitive to contributions of chirality-flip terms coming from high energy scale and new physics. Furthermore, the τ has a very short lifetime ($\sim$ 3 ps) and immediately decays in other particles, so different techniques to those for the case of stable particles like electron and muon are needed in order to measure the dipole moment. Today, the stronger bound on the τ EDM comes from measurements of the angular distributions in the e^+e^- annihilation into τ-pairs.

Searches for the τ electric dipole moment have been performed at LEP analysing the reaction $e^+e^- \to \tau^+\tau^-\gamma$ at the Z^0 pole. The τ EDM was determined from the energy of the photon and its isolation from the τ decay products, using the likelihood method from the momentum information of the radiated photon. The following upper limits at 95% confidence level were obtained:

$$-3.1 < d_\tau < 3.1(10^{-16}e \text{ cm}) \text{ by L3 [11]},$$
$$-3.8 < d_\tau < 3.6(10^{-16}e \text{ cm}) \text{ by OPAL [12]}.$$

Measuring the distribution of the $\tau^+\tau^-$ decay products in the reaction $e^+e^- \to \tau^+\tau^-$, ARGUS experiment set for the real and imaginary part of the τ EDM the limits of [13]:

$$|Re(d_\tau)| < 4.6 \times 10^{-16}e \text{ cm},$$
$$|Im(d_\tau)| < 1.8 \times 10^{-16}e \text{ cm}.$$

As ARGUS, the Belle collaboration performed an analysis adopting the Atwood and Soni method [14], which is the optimal observable method adopted in this thesis, that will be illustrated in the next chapter, obtaining the best existing bound on d_τ to date [15]. Belle's EDM measurement was performed using 29.5 fb^{-1} of data collected with the Belle detector at the KEKB Collider at $\sqrt{s} = 10.58$ GeV and 95% confidence level limits were set at:

$$-2.2 < Re(d_\tau) < 4.5(10^{-17}e \text{ cm}),$$
$$-2.5 < Im(d_\tau) < 0.8(10^{-17}e \text{ cm}).$$

1.3 τ EDM theoretical prediction

In the SM, the CP and T-violation effects in the lepton sector arise from a three-loop QCD correction that involves the CKM matrix phase. This leads to a lepton EDM:

$$d_l \sim 1.6 \cdot m_l[\text{MeV}] \times 10^{-40} e \text{ cm},$$

where m_l is the mass of the lepton [8, 9]. Thus the estimate for the τ lepton is: $d_\tau \sim 3 \times 10^{-37} e$ cm. This SM τ EDM value is too small by many orders of magnitude to be detected by any experiment now or in a foreseeable future. However, in various well-motivated extensions of the SM, d_τ would be sufficiently large to be experimentally detectable.

In the simplest form of the SM there is only one Higgs boson. However, in varius extensions two or more Higgs bosons could appear and CP-violation could then arise in a variety of new ways. In particular, it could appear directly in the coupling of one Higgs field to another one, or by the interference of the tree-level production process $e^+e^- \to \gamma, X \to \tau^+\tau^-$, where X is some new Higgs boson. The strength of the interference term is proportional to the initial and final state fermion masses $m_e m_\tau$.

In some 2-Higgs models of CP-violation, containing neutrals spin-0 bosons which may couple to leptons through lepton-flavor-conserving scalar and pseudoscalar coupling, lepton flavor-diagonal amplitudes at the one-loop level can generate a lepton EDM proportional to the cube of the lepton mass [16]:

$$d_l \approx \frac{eG_F m_l^3}{4\pi^2 m_\phi^2}, \tag{1.5}$$

where m_ϕ is the Higgs mass. This might yield to a $d_\tau \simeq 10^{-19} \div 10^{-17} e$ cm.

In other Multi-Higgs-doublet models [17][18], the EDM arises through two-loop diagrams with the neutral Higgs bosons and the top quark loop. The CP-violation arises from the propagator of the neutral Higgs bosons. Because of the coupling constant of Higgs bosons to fermions, the EDM is proportional to the fermion mass. In this case the estimate for the τ is $d_\tau < 4 \times 10^{-21} e$ cm [19].

In supersymmetric models in which each fermion has a sumersymmetric bosonic partner, τ-$\tilde{\tau}$-neutralino coupling may contain the CP-violating phase and generate a non-zero EDM in one loop diagrams. The contribution to d_l from these diagrams is proportional to left-handed and right-handed slepton mixing matrices. In the minimal supersymmetric standard model (MSSM) predictions, the coupling is proportional to the fermion mass [19] and the τ EDM must be less than $4 \times 10^{-23} e$ cm. However, in the generic MSSM model,

the constraint of the parameters in the above estimation is not necessarily true. Under a particular parameter set, one model predicts $d_\tau \simeq 10^{-19}e$ cm[19].

In the scalar leptoquark doublet model [20][21], which assumes that the couplings of the scalar leptoquarks are of the Higgs boson type, the couplings of the leptoquarks would be proportional to the mass of the right-handed fermion involved. In this case, the corresponding quark is coupled with the leptoquark in the loop diagram and the EDMs of leptons scale following the relation:

$$d_e : d_\mu : d_\tau = m_u^2 m_e : m_c^2 m_e : m_t^2 m_e.$$

Therefore, the d_τ can be as large as $10^{-19}e$ cm, limited by the present d_e bound.

1.4 τ dipole moment formalism

Any deviation from the SM, at low energies, can be parametrized by an effective Lagrangian built with the standard model particle spectrum, having as zero order term just the SM Lagrangian, and containing higher dimension gauge invariant operators suppressed by the scale of new physics, Λ [22][23][24]:

$$\mathcal{L}_{eff} = \mathcal{L}_{SM} + \Delta\mathcal{L}. \tag{1.6}$$

Let us write a gauge-invariant, proper Lorentz-invariant formulation for the interaction of the dipole moment of a spin-1/2 fermion with an electromagnetic and a weak field. We can build CP and T-odd corrections not only considering the possibility of an electric dipole moment d_τ but also of a "weak" dipole moment $\tilde{d}_\tau$ (WDM) arising in the weak interactions. The leading non standard effects which contribute to the EDM and WDM come from dimension six operators [25].

We start from the analogous formulation used for the anomalous magnetic moment, given by the well-known Lagrangian density:

$$\mathcal{L}_{Pauli} = -k\frac{\mu_B}{2}\bar{\psi}\sigma^{\mu\nu}\psi F_{\mu\nu}, \tag{1.7}$$

where ψ is the Dirac field for the fermion, $\bar{\psi}$ is the Dirac conjugate field, $\sigma^{\mu\nu} = (i/2)(\gamma^\mu\gamma^\nu - \gamma^\nu\gamma^\mu)$ where γ^μ, γ^ν are the usual 4x4 Dirac matrices, $F_{\mu\nu}$ is the electromagnetic field tensor, μ_B is the Bohr magneton, and k is an appropriate constant. The Lagrangian density of Eq. 1.7 is invariant under P and T transformation. To make this expression P-odd and T-odd it is

sufficient to replace $\sigma^{\mu\nu}$ with $\gamma^5\sigma^{\mu\nu}$, where $\gamma^5 = i\gamma^0\gamma^1\gamma^2\gamma^3$. Also, we replace $k\mu_B$ by id, where d is the real dipole moment, and i is included to make the resulting Hamiltonian Hermitian.

Thus we obtain:

$$\Delta\mathcal{L} = -\frac{i}{2}\bar{\psi}\sigma^{\mu\nu}\gamma_5\psi d_\tau F_{\mu\nu} - \frac{i}{2}\bar{\psi}\sigma^{\mu\nu}\gamma_5\psi\tilde{d}_\tau Z_{\mu\nu}, \tag{1.8}$$

where $F_{\mu\nu} = \partial_\mu A_\nu - \partial_\nu A_\mu$ and $Z_{\mu\nu} = \partial_\mu Z_\nu - \partial_\nu Z_\mu$ are the field tensors of the photon and the Z gauge boson coupled with d_τ and $\tilde{d}_\tau$ respectively.

The τ lepton dipole moment can be investigated in the τ-pair production in e^+e^- collisions through the process:

$$e^+e^- \to \gamma, Z \to \tau^+\tau^-. \tag{1.9}$$

At the lowest order in perturbation theory two distinct amplitudes contribute to this reaction: single photon exchange (electromagnetic interaction) and single Z^0 exchange (neutral weak interaction). When the center of mass (CM) energy $\sqrt{s}$ in reaction 1.9 is greater than the τ-pair threshold of $2m_\tau = 2 \times 1.77$ GeV, but much less than the Z^0 mass $m_Z = 91$ GeV, the electromagnetic amplitude is by far more significant than the neutral weak amplitude (on the contrary, at $\sqrt{s} \approx m_Z$ the neutral weak amplitude greatly dominates). Therefore, at *BABAR* experiment $\sqrt{s} = 10.58$ GeV, we can search for the τ electric dipole moment d_τ neglecting the weak amplitude.

No explicit relationship exists between d_τ and $\tilde{d}_\tau$, however these are expected to be roughly the same in many models of CP violation. Thus from a limit on $\tilde{d}_\tau$ we may obtain a model-independent limit on d_τ and vice-versa. Furthermore an upper limit on d_τ can be obtained by the comparison of the observed partial width of the Z resonance decay into $\tau^+\tau^-$ with that predicted by the SM.

In principle d_τ and $\tilde{d}_\tau$ can depend on q^2, where q is the 4-momentum transfer, but in this effective Lagrangian approach, only higher dimension operators contribute to the difference $d_\tau(q^2) - d_\tau(0)$ and if $|q^2| \ll \Lambda^2$, as required for the consistency of the effective Lagrangian approach, their effects will be suppressed by powers of q^2/Λ^2. This allows to make no distinction between the *dipole moment* d_τ and the *dipole form factor* $d_\tau(q^2)$. The electric dipole form-factor is often expressed in terms of the dimensionless dipole moment a_τ, given as:

$$d_\tau = \frac{e}{2m_\tau}a_\tau, \tag{1.10}$$

then, for the first order τ EDM contribution Lagrangian we have:

$$\mathcal{L}_{EDM} = -i\frac{e}{2m_\tau}a_\tau\bar{\tau}\sigma^{\mu\nu}\gamma^5\tau F_{\mu\nu}. \tag{1.11}$$

A part of this EDM term can be calculated as

$$\sigma^{0i}\gamma_5 F_{0i} = \sigma^{i0}\gamma_5 F_{i0} = -i \begin{pmatrix} \sigma^i & 0 \\ 0 & \sigma^i \end{pmatrix}, \tag{1.12}$$

where E^i is the electric field and σ^i is the spin operator. At the non-relativistic limit, the Lagrangian $\mathcal{L}_{EDM}$ becomes:

$$\mathcal{L}_{EDM} = -id_\tau \bar{\tau}\sigma^{\mu\nu}\gamma^5 \tau F_{\mu\nu} \to -d_\tau \vec{\sigma} \cdot \vec{E}, \tag{1.13}$$

as expected for an electric dipole moment interaction.

1.5 τ EDM effect in τ-pairs production

In this section, we will show how the dipole moment effects can be studied at leading order in the $e^+e^- \to \tau^+\tau^-$ differential cross section. Let's start analysing the contribution to the τ-pair production coming from the SM and the one coming from the first order effective Lagrangian (1.11), i.e. the CP-violating (CPV) term induced by a non-zero d_τ. At *BABAR* energies the tree level contributions come from γ exchange (off the Υ peak) or Υ exchange (at the Υ peak) in the s-channel. The interferences with the Z exchange ($\gamma - Z$, $\Upsilon - Z$ at the Υ peak) are suppressed by powers of q^2/M_Z^2. At tree level then, the relevant diagrams are shown in Fig. 1.1, where diagrams (a) and (b) are SM contributions, and (c) and (d) come from BSM amplitudes.

The SM radiative corrections that may contribute to CP-odd observables (for example the ones that generate the SM electric dipole moment for the τ) appear in higher orders in the coupling constant, and at the present level of experimental sensitivity they are not measurable. On these grounds the bounds on the EDM that one may get are just coming from the physics beyond the SM.

The transition amplitude T for $e^+e^- \to \tau^+\tau^-$ reaction with taus decaying to a specific final state can be written rather generally as:

$$\mathrm{T} = \mathrm{T}_{SM} + \mathrm{T}_{CPV}, \tag{1.14}$$

where T_{SM} is the CP-conserving Standard Model part, and T_{CPV} is the CP-violating part. The differential cross section will be then proportional to:

$$|\mathrm{T}_{SM} + \mathrm{T}_{CPV}|^2 = (|\mathrm{T}_{SM}|^2 + |\mathrm{T}_{CPV}|^2) + (\mathrm{T}^*_{SM}\mathrm{T}_{CPV} + c.c.). \tag{1.15}$$

We will see that the interference term between SM and BSM amplitudes manifests itself in some CP-odd observables (correlations) in the differential

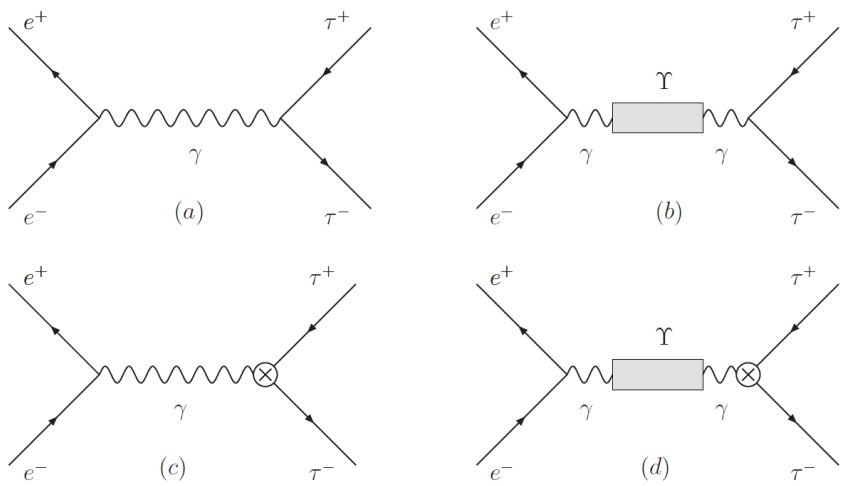

Figure 1.1: Diagrams for the tree level $\tau^+\tau^-$ production with: direct γ exchange (a), $\Upsilon(4S)$ production (b), EDM in γ exchange (c) and EDM in $\Upsilon(4S)$ production (d).

cross section. The EDM term only shows up in the spin-spin correlation matrix [26], thus these correlations are related to the spins of the outgoing $\tau^+\tau^-$.

In principle, the transition amplitude can have real and imaginary parts. The latter would arise from final state interactions and/or from absorptive components in the propagators of unstable particles among the decay products. In order to allow the T_{CPV} to have an imaginary part, we must assume that also d_τ could have an imaginary part.

The spin properties of the produced taus translate in the angular distribution of both tau decay products. As we will see in the next chapter, in order to have access to the EDM, one has to measure this angular distribution, looking for asymmetries.

1.5.1 $e^+e^- \to \tau^+\tau^-$ spin density

We now consider the τ-pair production in e^+e^- collissions through direct γ exchange (diagrams (a) and (c) in Fig. 1.1) and we show how to calculate the spin amplitudes for:

$$e^-(p,\lambda) + e^+(\bar{p},\bar{\lambda}) \to \tau^-(k,\sigma) + \tau^+(\bar{k},\bar{\sigma}), \tag{1.16}$$

where p ($\bar{p}$), k ($\bar{k}$) denote the 4-momenta for the initial electrons (positrons) and τ^- (τ^+) and $\lambda, \bar{\lambda}, \sigma, \bar{\sigma}$ denote the relative helicities. The helicities will be

represented by "$-$" and "$+$" for the left-handed and right-handed particles respectively.

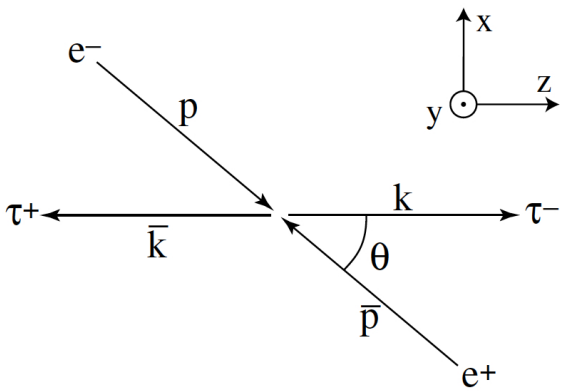

Figure 1.2: Coordinate system for the differential cross section calculation.

In order to simplify the calculation, the coordinate system defined in Fig.1.2 is used, which is the CM system ($\tau^+\tau^-$ rest frame), with the z-axis parallel to the τ^- momentum-vector. θ is the angle between the τ^- and e^- momentum-vectors. In this coordinate system, τ polarization along the directions x, y, z corresponds to what is called transverse (T), normal (N) and longitudinal (L) polarization respectively and the 4-momenta are defined as follows:

$$\begin{aligned} k^\mu &= E(1,0,0,\beta), \\ \bar{k}^\mu &= E(1,0,0,-\beta), \\ p^\mu &= E(1,-sin\theta,0,cos\theta), \\ \bar{p}^\mu &= E(1,sin\theta,0,-cos\theta). \end{aligned} \tag{1.17}$$

We give explicit formulas for the spin-density matrix of the τ leptons produced in this reference system, assuming unpolarized e^+ and e^- beams, neglecting the electron mass and only keeping linear terms in the EDM. From the effective Lagrangian (Eq. 1.8), the spin-dependent amplitudes are written as:

$$i\mathcal{M} = -ieQ_e(j_{L_\mu}+j_{R_\mu})\frac{-i}{s}\left[-ieQ_\tau(J_L^\mu + J_R^\mu) - i\frac{e}{2m_\tau}(a_\tau J_a^\mu + \tilde{a}_\tau J_{\tilde{a}}^\mu)\right] \tag{1.18}$$

where Q_e and Q_τ are the electron and τ charges respectively ($Q_e = Q_\tau = -1$), s is the square CM energy ($\sqrt{s} = 2E$). The charged currents are defined as

follows:

$$
\begin{aligned}
j_L^\mu &= \bar{v}_e(\bar{p}, \bar{\lambda} = +)\gamma^\mu \frac{1-\gamma_5}{2} u_e(p, \lambda = -), \\
j_R^\mu &= \bar{v}_e(\bar{p}, \bar{\lambda} = -)\gamma^\mu \frac{1+\gamma_5}{2} u_e(p, \lambda = +), \\
J_L^\mu &= \bar{u}_\tau(k, \sigma)\gamma^\mu \frac{1-\gamma_5}{2} v_\tau(\bar{k}, \bar{\sigma}), \\
J_R^\mu &= \bar{u}_\tau(k, \sigma)\gamma^\mu \frac{1+\gamma_5}{2} v_\tau(\bar{k}, \bar{\sigma}), \\
J_a^\mu &= -i\bar{u}_\tau(k, \sigma)\sigma^{\mu\nu} q_\nu v(\bar{k}, \bar{\sigma}), \\
J_{\tilde{a}}^\mu &= -\bar{u}_\tau(k, \sigma)\sigma^{\mu\nu} q_\nu v(\bar{k}, \bar{\sigma}).
\end{aligned}
\tag{1.19}
$$

where $q_\nu = (\sqrt{s}, 0, 0, 0)$ is the 4-momentum of the internal photon.

Performing the explicit calculations, the spin-dependent amplitudes $\mathcal{M}(\lambda\bar{\lambda}\sigma\bar{\sigma})$ are obtained as:

$$
\begin{aligned}
\mathcal{M}(+-++) &= \frac{e^2}{s}[-4Em_\tau sin\theta] + \frac{-e^2}{2m_\tau s}\tilde{a}_\tau[8iE^3\beta sin\theta], \\
\mathcal{M}(+-+-) &= \frac{e^2}{s}[-4E^2(1+cos\theta)], \\
\mathcal{M}(+--+) &= \frac{e^2}{s}[4E^2(1-cos\theta)], \\
\mathcal{M}(+---) &= \frac{e^2}{s}[4Em_\tau sin\theta] + \frac{-e^2}{2m_\tau s}\tilde{a}_\tau[8iE^3\beta sin\theta], \\
\mathcal{M}(-+++) &= \frac{e^2}{s}[-4Em_\tau sin\theta] + \frac{-e^2}{2m_\tau s}\tilde{a}_\tau[8iE^3\beta sin\theta], \\
\mathcal{M}(-++-) &= \frac{e^2}{s}[4E^2(1-cos\theta)], \\
\mathcal{M}(-+-+) &= \frac{e^2}{s}[-4E^2(1+cos\theta)], \\
\mathcal{M}(-+--) &= \frac{e^2}{s}[4Em_\tau sin\theta] + \frac{-e^2}{2m_\tau s}\tilde{a}_\tau[8iE^3\beta sin\theta].
\end{aligned}
\tag{1.20}
$$

The first term in each amplitude shows the lowest-order coupling and the second term shows the interference term of the lowest order and the EDM coupling. The EDM terms appear in the amplitude of the $(\sigma\bar{\sigma}) = (++)$ and $(--)$ states, while the $(\sigma\bar{\sigma}) = (+-)$ and $(-+)$ states are independent of the EDM. Schematic views of these spin states are shown in Fig. 1.3 and 1.4. These results indicate that the EDM coupling affects the interaction

between the left-handed and right-handed τ lepton, in this case we have a linear EDM contribution. The interference of the diagrams shown in Fig. 1.3 and 1.4 causes a first-order CPV effect.

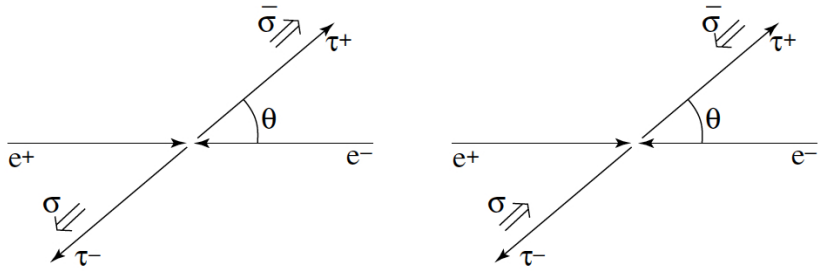

Figure 1.3: Spin states that induce the electric dipole moment.

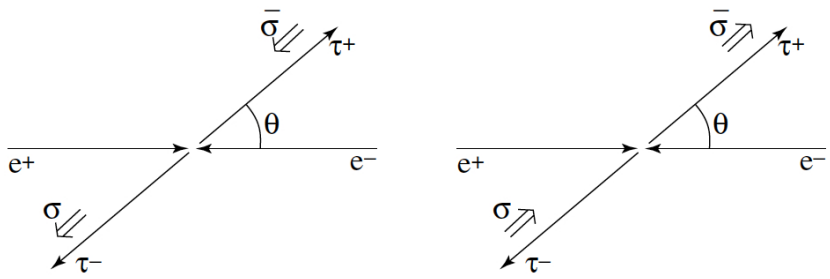

Figure 1.4: Spin states that are independent of the electric dipole moment.

Equal conclusions are reached considering the case of the τ-pair production mediated by the resonance: $e^+e^- \to \Upsilon \to \tau^+\tau^-$. It can be demostrated [27] that the EDM contribution introduces the same polarization matrix terms as in the γ exchange case. The only difference is an overall factor that is introduced in the cross section. There are no changes in the asymmetries, whose expressions remain the same in Eq. 1.20.

In order to express the amplitudes in terms of the experimental observables, it is convenient to transform the spin amplitude notation from the bispinor indices into the spin-vector:

$$e^+(\vec{p}) + e^-(-\vec{p}) \to \tau^+(\vec{k}, \vec{S}_+) + \tau^-(-\vec{k}, \vec{S}_-), \tag{1.21}$$

where $\vec{p}$ is the positron momentum in the CM frame (thus $-\vec{p}$ for the electron), $\vec{k}$ is the τ^+ momentum (thus $-\vec{k}$ for the τ^-) and $\vec{S}_+$, $\vec{S}_-$ are the τ^+ and τ^- spin vectors in the CM frame. The spin vectors are derivable from the τ flight direction and the momenta of the decay daughters.

The spin-density matrix of reaction 1.21 is given by [28]:

$$\mathcal{M}^2_{prod} = \mathcal{M}^2_{SM} + Re(d_\tau)\mathcal{M}^2_{Re} + Im(d_\tau)\mathcal{M}^2_{Im} + |d_\tau|^2\mathcal{M}^2_{d^2}, \tag{1.22}$$

where $\mathcal{M}^2_{SM}$ corresponds to the SM term, $\mathcal{M}^2_{Re}$ and $\mathcal{M}^2_{Im}$ correspond to the interference terms between the SM and the CPV amplitudes, proportional to the real and imaginary part of the EDM respectively.

Explicit expressions are [28]:

$$\begin{aligned}\mathcal{M}^2_{SM} =& \frac{e^4}{k_0^2}[k_0^2 + m_\tau^2 + |\vec{k}^2|(\hat{k}\cdot\vec{p})^2 - \vec{S}_+\cdot\vec{S}_-|\vec{k}|^2(1-(\hat{k}\cdot\vec{p})^2) \\ &+ 2(\hat{k}\cdot\vec{S}_+)(\hat{k}\cdot\vec{S}_-)(|\vec{k}|^2 + (k_0-m_\tau)^2(\hat{k}\cdot\vec{p})^2) + 2k_0^2(\hat{k}\cdot\vec{S}_+)(\hat{p}\cdot\vec{S}_-) \\ &- 2k_0(k_0-m_\tau)(\hat{k}\cdot\vec{p})((\hat{k}\cdot\vec{S}_+)(\hat{p}\cdot\vec{S}_-) + (\hat{k}\cdot\vec{S}_-)(\hat{p}\cdot\vec{S}_+))],\end{aligned} \tag{1.23}$$

$$\begin{aligned}\mathcal{M}^2_{Re} =& 4\frac{e^3}{k_0}|\vec{k}|[-(m_\tau + (k_0-m_\tau)(\hat{k}\cdot\hat{p})^2)(\vec{S}_+\times\vec{S}_-)\cdot\hat{k} \\ &+ k_0(\hat{k}\cdot\hat{p})(\vec{S}_+\times\vec{S}_-)\cdot\hat{p}],\end{aligned} \tag{1.24}$$

$$\begin{aligned}\mathcal{M}^2_{Im} =& 4\frac{e^3}{k_0}|\vec{k}|[-(m_\tau + (k_0-m_\tau)(\hat{k}\cdot\hat{p})^2)(\vec{S}_+-\vec{S}_-)\cdot\hat{k} \\ &+ k_0(\hat{k}\cdot\hat{p})(\vec{S}_+-\vec{S}_-)\cdot\hat{p}],\end{aligned} \tag{1.25}$$

$$\mathcal{M}^2_{d^2} = 4e^2|\vec{k}|^2\cdot(1-(\hat{k}\cdot\hat{p})^2(1-\vec{S}_+\cdot\vec{S}_-)), \tag{1.26}$$

where k_0 is the τ energy and the hat denotes unitary vectors.

The T-odd normal-transverse $(\vec{S}_+\times\vec{S}_-)_{N,T}$ and normal-longitudinal $(\vec{S}_+\times\vec{S}_-)_{N,L}$ correlation terms are porportional to the real part of the EDM. Under CP and T transformation for the spin-momentum correlation components in $\mathcal{M}^2_{Re}$ and $\mathcal{M}^2_{Im}$ respectively, we have (for $\vec{p}_\pm$ instead of $\vec{k}_\pm$ the expressions are the same):

$$\begin{aligned}&\mathcal{CP}((\vec{S}_+\times\vec{S}_-)\cdot\vec{k}_+) = (\vec{S}_-\times\vec{S}_+)\cdot(-\vec{k}_-) = -((\vec{S}_+\times\vec{S}_-)\cdot\vec{k}_+), \\ &\mathcal{T}((\vec{S}_+\times\vec{S}_-)\cdot\vec{k}_+) = ((-\vec{S}_+)\times(-\vec{S}_-))\cdot(-\vec{k}_-) = -((\vec{S}_+\times\vec{S}_-)\cdot\vec{k}_+),\end{aligned}$$

$$\begin{aligned}&\mathcal{CP}((\vec{S}_+-\vec{S}_-)\cdot\vec{k}_+) = (\vec{S}_--\vec{S}_+)\cdot(-\vec{k}_-) = -((\vec{S}_+-\vec{S}_-)\cdot\vec{k}_+), \\ &\mathcal{T}((\vec{S}_+-\vec{S}_-)\cdot\vec{k}_+) = ((-\vec{S}_+)-(-\vec{S}_-))\cdot(-\vec{k}_+) = ((\vec{S}_+-\vec{S}_-)\cdot\vec{k}_+).\end{aligned}$$

Therefore $\mathcal{M}^2_{Re}$ is CP-odd and T-odd, while $\mathcal{M}^2_{Im}$ is CP-odd and T-even. These properties demonstrate that the real part of the EDM is the CP-violating parameter. Moreover, the imaginary part of the EDM, if different from zero, would be responsible for the CPT-violation.

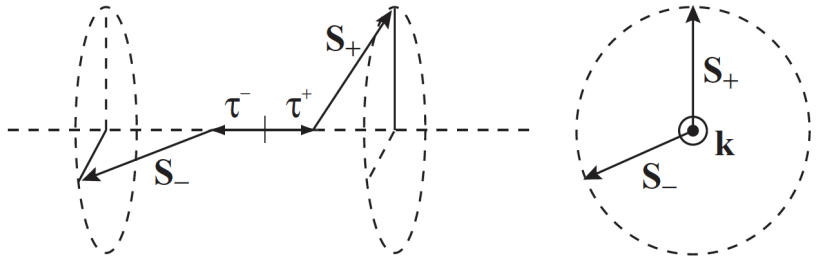

Figure 1.5: Configuration of the spin correlation for $(\vec{S}_+ \times \vec{S}_-) \cdot \vec{k}$ related to $\mathcal{M}^2_{Re}$. The sign depends on the transverse spin correlation.

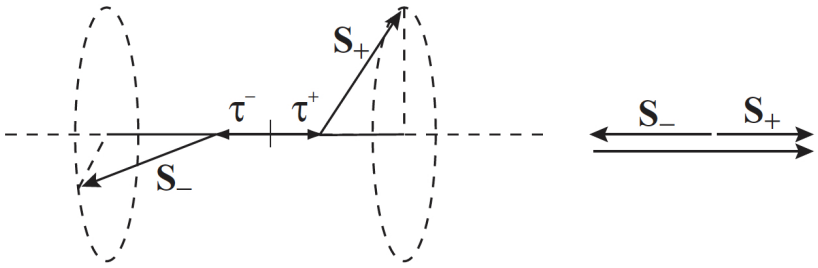

Figure 1.6: Configuration of the spin correlation for $(\vec{S}_+ - \vec{S}_-) \cdot \vec{k}$ related to $\mathcal{M}^2_{Im}$. The sign depends on the longitudinal spin correlation.

Figures 1.5 and 1.6 show the spin-momentum correlations for $(\vec{S}_+ \times \vec{S}_-) \cdot \vec{k}$ and $(\vec{S}_+ - \vec{S}_-) \cdot \vec{k}$ respectively. The sign of $(\vec{S}_+ \times \vec{S}_-) \cdot \vec{k}$ depends on the transverse spin correlation to $\vec{k}$, while the sign of $(\vec{S}_+ - \vec{S}_-) \cdot \vec{k}$ depends on the longitudinal spin correlation. Therefore, the EDM for the real part causes an angular asymmetry around $\vec{k}$ and $\vec{p}$, and the EDM for the imaginary part causes an asymmetry along $\vec{k}$ and $\vec{p}$. In the next chapter we will see how these asymmetries can be investigated.

Chapter 2

τ lepton EDM Measurement Method

As seen in the past chapter, the CP-odd quantities generated by the interference term between SM and BSM amplitudes in the differential cross section, are related to the correlations between the spins of the outgoing $\tau^+\tau^-$ and the τ momenta. The τ spin is not directly observable because of the τ lepton short lifetime. Nevertheless tau leptons transfer information about their spins to the energies and momenta of the decay products.

In the present analysis, the final state in which both tau leptons decay via $\tau^\pm \to \pi^\pm \nu_\tau$ has been chosen. In this decay channel, characterized by the presence of one charged track and only one neutrino, the reconstruction of the τ spin vector is relatively straightforward. In addition, the two body decay kinematics reduces the τ momentum reconstruction ambiguity.

In this chapter we will see how to measure d_τ observing the τ leptons decay products. Furthermore, starting from the spin density matrix measurement, *optimal observables* are constructed and used.

The EDM measurement method and the required algorithms have been tested with a MC simulating and ideal sample of 10^7 signal events. τ-pairs production is simulated with the KK2F MC event generator [29] and subsequent decays of τ leptons are modeled with TAUOLA [30]; detector effects are not simulated. The analysis method validation with this MC sample is reported in the following sections.

2.1 Optimal Observables

In this analysis, the *Optimal Observables method* proposed by Atwood and Soni [14] and Davier [31] is used, in order to obtain the highest sensitivity

on the τ EDM.

Starting from a differential cross section $\sigma(\phi)d\phi$, where ϕ represents the relevant phase-space variables being considered (including angular and polarization variables), we want to consider the general problem of observing the change in the differential cross section due to the addition of any small coupling. It can be demonstrated that if there is a small contribution to this differential cross section controlled by a parameter λ (in our case given by d_τ) such that we can expand the total differential cross section in terms of λ as

$$\sigma = \sigma_0 + \lambda\sigma_1, \tag{2.1}$$

the most effective observable to resolve λ is:

$$\mathcal{O} = \frac{\sigma_1}{\sigma_0}. \tag{2.2}$$

This statement is demostrated in Appendix A, where we also show that the sensitivity of this optimal observable is the same as the one obtained with the likelihood method.

2.1.1 Observables for EDM

In the total amplitude the τ-pair production and the tau leptons decay matrix elements ($\mathcal{M}^2_{prod}$ and $\mathcal{M}^2_{dec}$, respectively) can be factorized: $\mathcal{M}^2 = \mathcal{M}^2_{prod} \cdot \mathcal{M}^2_{dec}$. According to Eq. 1.22, we can therefore construct two optimal observables for our analysis, one for the real EDM part and one for the imaginary EDM part estimate, given respectively by:

$$\mathcal{O}_{Re} = \frac{\mathcal{M}^2_{Re}}{\mathcal{M}^2_{SM}}, \quad \mathcal{O}_{Im} = \frac{\mathcal{M}^2_{Im}}{\mathcal{M}^2_{SM}}, \tag{2.3}$$

where the matrix elements $\mathcal{M}^2_{SM}$, $\mathcal{M}^2_{Re}$ and $\mathcal{M}^2_{Im}$ are defined in Eq. 1.23, 1.24 and 1.25, respectively. These observables will be calculated event-by-event, as described later. Because of the properties of the matrix elements, $\mathcal{O}_{Re}$ is CP-odd and T-odd, while $\mathcal{O}_{Im}$ is CP-odd and T-even.

Using the squared matrix elements $\mathcal{M}^2_{prod}$, the differential cross section $d\sigma$ for the $e^+e^- \to \tau^+\tau^-$ process, is given as $d\sigma \propto \mathcal{M}^2_{prod} d\phi$.

We want to estimate the mean value of the observable $\langle\mathcal{O}_{Re}\rangle$ (and $\langle\mathcal{O}_{Im}\rangle$), expressed as:

$$
\begin{aligned}
\langle \mathcal{O}_{Re} \rangle &\propto \int \mathcal{O}_{Re} d\sigma \propto \int \mathcal{O}_{Re} \mathcal{M}^2_{prod} d\phi \\
&= \int \frac{\mathcal{M}^2_{Re}}{\mathcal{M}^2_{SM}} (\mathcal{M}^2_{SM} + Re(d_\tau)\mathcal{M}^2_{Re} + Im(d_\tau)\mathcal{M}^2_{Im} + |d_\tau|^2 \mathcal{M}^2_{d^2}) d\phi \\
&= \int \mathcal{M}^2_{Re} d\phi + Re(d_\tau) \int \frac{(\mathcal{M}^2_{Re})^2}{\mathcal{M}^2_{SM}} d\phi \\
&+ Im(d_\tau) \int \frac{\mathcal{M}^2_{Re}\mathcal{M}^2_{Im}}{\mathcal{M}^2_{SM}} d\phi + |d_\tau|^2 \int \frac{\mathcal{M}^2_{Re}\mathcal{M}^2_{d^2}}{\mathcal{M}^2_{SM}} d\phi,
\end{aligned}
\tag{2.4}
$$

where the third term is zero because the integrated elements, $\mathcal{M}^2_{Re}$ and $\mathcal{M}^2_{Im}$, are orthogonal and the fourth term, which includes $\mathcal{M}^2_{d^2}$, can be neglected since d_τ is small. For $\langle \mathcal{O}_{Im} \rangle$ an analogous expression is obtained.

From equation 2.4 we can see that $\langle \mathcal{O}_{Re} \rangle$ and $\langle \mathcal{O}_{Im} \rangle$ are approximately given by linear functions of d_τ:

$$
\begin{aligned}
\langle \mathcal{O}_{Re} \rangle &= \tilde{a}_{Re} \cdot Re(d_\tau) + \tilde{b}_{Re}, \\
\langle \mathcal{O}_{Im} \rangle &= \tilde{a}_{Im} \cdot Im(d_\tau) + \tilde{b}_{Im}.
\end{aligned}
\tag{2.5}
$$

Here, a_{Re} and a_{Im} express the sensitivity for $Re(d_\tau)$ and $Im(d_\tau)$ respectively, while b_{Re} and b_{Im} provide offsets. Since the coefficients are expressed as:

$$
\begin{aligned}
\int \frac{(\mathcal{M}^2_{Re})^2}{\mathcal{M}^2_{SM}} d\phi &\simeq \int \left(\frac{\mathcal{M}^2_{Re}}{\mathcal{M}^2_{SM}} \right)^2 \mathcal{M}^2_{prod}\, d\phi, \\
\int \frac{(\mathcal{M}^2_{Im})^2}{\mathcal{M}^2_{SM}} d\phi &\simeq \int \left(\frac{\mathcal{M}^2_{Im}}{\mathcal{M}^2_{SM}} \right)^2 \mathcal{M}^2_{prod}\, d\phi,
\end{aligned}
\tag{2.6}
$$

a_{Re} and a_{Im} are given by the mean of the square observables, $a_{Re} = \langle \mathcal{O}^2_{Re} \rangle$ and $a_{Im} = \langle \mathcal{O}^2_{Im} \rangle$. Therefore, the width of the observable distributions is directly correlated with the sensitivity.

Due to the CP-odd properties of $\mathcal{M}^2_{Re}$ and $\mathcal{M}^2_{Im}$ seen in Chapter 1, the offsets b_{Re} and b_{Im}, i. e. the observable means for $d_\tau = 0$, should be different from zero only if there are experimental asymmetries in the kinematics (like the one due to the boost) or in the apparatus acceptance.

Once known a_i and b_i, the EDMs $Re(d_\tau)$ and $Im(d_\tau)$ can be extracted from $\langle \mathcal{O}_{Re} \rangle$ and $\langle \mathcal{O}_{Im} \rangle$ using equations 2.5. The analysis method consists on the evaluation of a_i and b_i from the correlation between the observables

and d_τ obtained by a full MC simulation, in which different EDM values are introduced. Once a_i and b_i are estimated, $Re(d_\tau)$ and $Im(d_\tau)$ will be extracted from the measurement of $\langle \mathcal{O}_{Re} \rangle$ and $\langle \mathcal{O}_{Im} \rangle$ on experimental data.

2.2 Calculation of the observables

The observables in Eq. 2.3 are calculated with the matrix elements defined in Eq. 1.23, 1.24 and 1.25 which are expressed in terms of the e^+ beam direction $\hat{p}$, the τ^+ flight direction $\hat{k}$, and the τ^+ and τ^- spin vectors $\vec{S}_\pm$. All these vectors are expressed in the τ-pair rest frame.

Experimentally, a complete τ momentum reconstruction is not possible because of the presence of undetectable neutrinos. The quantities $\hat{k}$ and $\vec{S}_\pm$ are therefore not univocally defined, however they can be kinematically constrained.

The observables used in the analysis will be calculated using event-by-event the mean value of $\mathcal{M}^2_{SM}$, $\mathcal{M}^2_{Re}$ and $\mathcal{M}^2_{Im}$, averaging over the possible kinematic configurations for each event. In the following subsection we show how to calculate the possible τ directions and the τ spin vector starting from its decay products.

2.2.1 Tau flight direction reconstruction

The signal event chosen for this analysis is represented by the $e^+e^- \to \tau^+\tau^-$ process in which both tau leptons decay via $\tau \to \pi\nu$. This decay channel is a two body decay characterized by one charged track and one undetected neutrino. The flight direction of the mother τ lepton is constrained on the surface of the cone around the charged daughter flight direction with opening angle given by the kinematics of two body decays:

$$cos\theta_{cone} = \frac{2E_\tau E_\pi - m_\pi^2 - m_\tau^2}{2|\vec{k}||\vec{p}_\pi|}, \tag{2.7}$$

where E_π, $\vec{p}_\pi$ are the measured energy and momentum of the decay daughter. E_τ is the τ energy in the CM frame ($\sqrt{s}/2$), m_τ and m_π are the involved particle masses.

Then for the τ^+ and τ^- flight directions ($\vec{k}_+$, $\vec{k}_-$) we have respectively:

$$\begin{aligned} \hat{k}_+ \cdot \hat{p}_{\pi^+} &= cos\theta^+_{cone}, \\ \hat{k}_- \cdot \hat{p}_{\pi^-} &= cos\theta^-_{cone}. \end{aligned} \tag{2.8}$$

where the hats denote unitary vectors.

The geometry of the two conical surfaces allowed by the kinematics for the τ fligh directions is shown in figure 2.1.

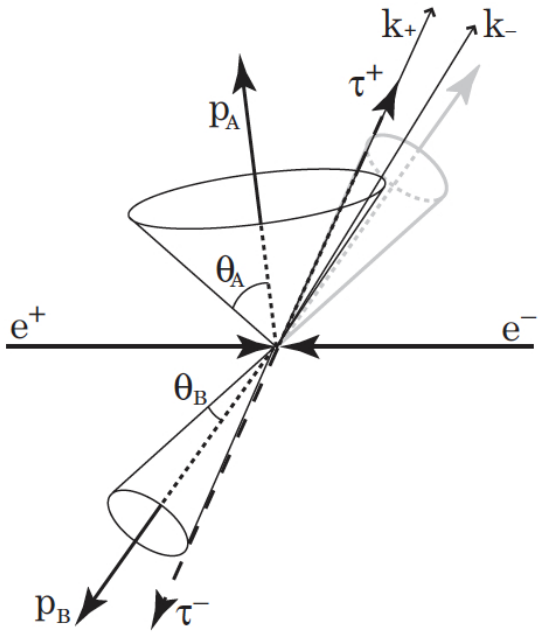

Figure 2.1: Schematic view of the τ pair event $e^+e^- \rightarrow \tau^+(\vec{k}_+)\tau^-(\vec{k}_-) \rightarrow \pi^+(\vec{p}_A)\pi^-(\vec{p}_B)\nu_\tau\bar{\nu}_\tau$. θ_A and θ_B are the opening angles between the momenta of the tau leptons and their charged decay products.

Since in the CM frame the two tau leptons are produced back-to-back, $\vec{k}_+ = -\vec{k}_- = \vec{k}$. So, in the case of both tau leptons decaying hadronically, the τ fligh direction must sit in the intersection of the two cones. Then we have just a twofold ambiguity given by the solutions of the second order equation obtained from Eq. 2.8 with the back-to-back condition:

$$\begin{cases} \hat{k} \cdot \hat{p}_{\pi^+} = cos\theta^+_{cone} \\ \hat{k} \cdot \hat{p}_{\pi^-} = -cos\theta^-_{cone} \end{cases} \tag{2.9}$$

Combinig the two equations and using the vector identity $\vec{A} \times (\vec{B} \times \vec{C}) = \vec{B}(\vec{A} \cdot \vec{C}) - \vec{C}(\vec{A} \cdot \vec{B})$ we obtain:

$$(\hat{p}_{\pi^+} \times \hat{p}_{\pi^-}) \times \hat{k} = \hat{p}_{\pi^+}\ cos\theta^-_{cone} + \hat{p}_{\pi^-}\ cos\theta^+_{cone}. \tag{2.10}$$

Defining $\vec{H} = \hat{p}_{\pi^+}\ cos\theta^-_{cone} + \hat{p}_{\pi^-}\ cos\theta^+_{cone}$ and $\vec{p}_\perp = \hat{p}_{\pi^+} \times \hat{p}_{\pi^-}$ the above equation becomes:

$$\vec{p}_\perp \cdot \hat{k} = \vec{H}. \tag{2.11}$$

Since $|\hat{k}| = 1$, finally we get:

$$k_z^2|p_\perp|^2 - 2(\vec{H}\cdot\vec{p}_\perp)_z k_z + H^2 - H_z^2 - p_{\perp z}^2 = 0. \tag{2.12}$$

The two solutions of this second order equation are given by:

$$\begin{aligned} k_z &= \frac{-b \pm \Delta}{a}, \\ k_x &= \frac{p_{\perp y}}{p_{\perp z}} k_z + \frac{H_x}{p_{\perp z}}, \\ k_y &= \frac{p_{\perp x}}{p_{\perp z}} k_z - \frac{H_y}{p_{\perp z}}, \end{aligned} \tag{2.13}$$

where $a = |p_\perp|^2$, $b = -(\vec{H}\times\vec{p}_\perp)_z$, $c = H^2 - H_z^2 - p_{\perp z}^2$ and $\Delta = \sqrt{b^2 - ac}$.

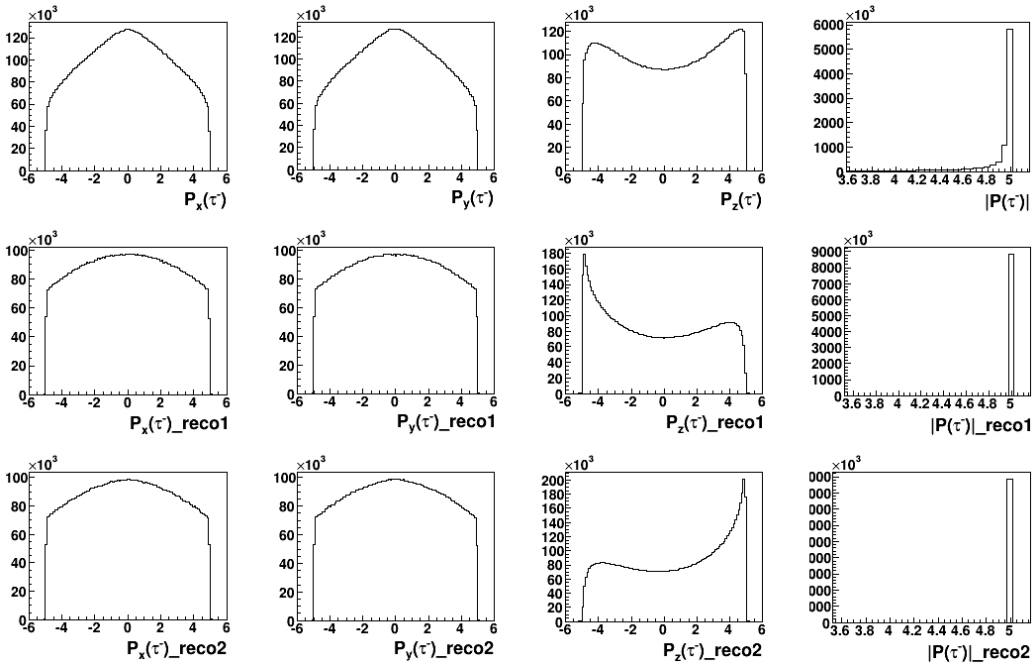

Figure 2.2: Distributions of the τ^- momentum components and module. Top: true τ^- momentum. Middle and bottom: reconstructed τ^- momentum, obtained for $+\Delta$ and $-\Delta$ solutions of Eq. 2.13, respectively.

In Fig. 2.2 and Fig. 2.3 we show the distributions of the components (k_x, k_y, k_z) and module $(|\vec{k}|)$ of the momentum in the CM frame obtained for τ^+ and τ^- respectively. On top is the true τ momentum, middle and bottom plots shown the two solutions obtained with the τ momentum reconstruction algorithm. On average each of the two solution is correct in 50% of cases.

The tail at low values visible in the true τ momentum module distribution (top right plot of Fig. 2.2 and Fig. 2.3) is caused by the initial state radiation which reduces the CM energy $\sqrt{s}$. On the contrary, in the τ momentum vector reconstruction procedure, the momentum module in the CM frame is always assumed to be $\sqrt{s}/2$, neglecting the radiation effect. Radiated photons indeed are not experimentally detected, therefore the radiation is ignored and its effect will be considered in the systematic errors evaluation.

The initial state radiation modifies the boost of the laboratory frame with respect to the τ pairs rest frame, leading to a not exactly Lorentz transformation. In case of hard radiation the error in the CM frame reconstruction is enhanced and we can have no solutions for the τ flight direction because Δ in Eq. 2.13 results to be negative and the two cones don't intersect. With this ideal MC sample about 13% of events are lost for this reason.

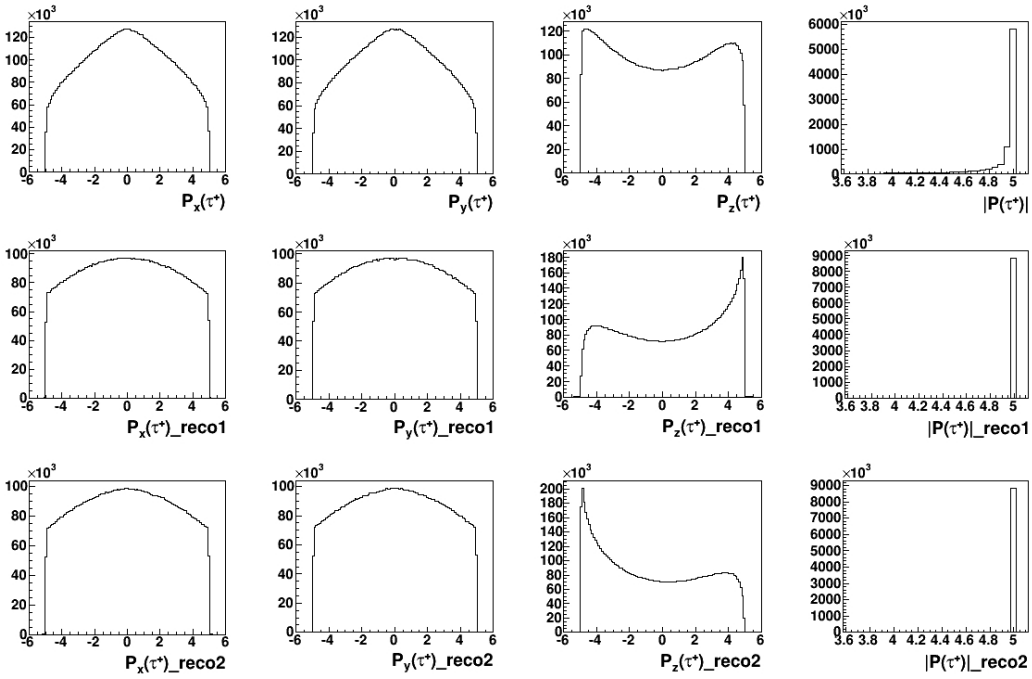

Figure 2.3: Distributions of the τ^+ momentum components and module. Top: true τ^+ momentum. Middle and bottom: reconstructed τ^+ momentum, obtained for $+\Delta$ and $-\Delta$ solutions of Eq. 2.13, respectively.

Fig. 2.4 shows the cosine of the angle θ_{diff}, which is the angle between the generated τ direction and the reconstructed one used for calculation, for one of the two solutions. The large tail is due to the 50% of incorrect solutions.

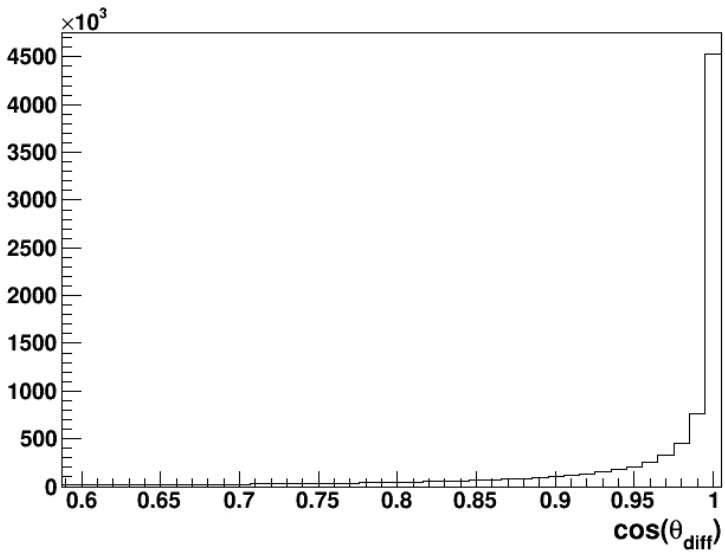

Figure 2.4: Cosine of the angle θ_{diff} between the generated τ momentum and the reconstructed τ flight direction for one of the two solutions (the plot for the other solution is similar).

2.2.2 Recontruction of the τ spin vector

The spin vectors can be calculated from the momenta of the decay particles and the τ flight direction [32]. For any decay of a polarized τ, the differential partial width is [33]:

$$d\Gamma = \frac{|\bar{\mathcal{M}}|^2}{2m_\tau}(1 - h_\mu S^\mu)dQ, \tag{2.14}$$

where $|\bar{\mathcal{M}}|^2$ is the spin-averaged squared matrix element, dQ is the Lorentz-invariant phase space factor and h_μ is the polarimeter vector, function of the momenta of the τ and the decay particles. The four vector S^μ reduces to the three-dimensional polarization vector $\vec{S}$ in the τ rest frame. In this frame the $1 - h_\mu S^\mu$ term becomes $1 + \vec{h} \cdot \vec{S}$ with $|\vec{S}| = \tau$ polarization.

For the decay channel we are considering

$$\tau^\pm(\vec{k}'_\pm, \vec{S}_\pm) \to \pi^\pm(\vec{p}'_\pi)\nu_\tau(\vec{q}'_\tau)$$

(where the prime symbol indicates momenta expressed in the single τ rest frame), the polarimeter vector $\vec{h}$ is given by the unit vector in the direction of flight of the pion:

$$\vec{h}_\pm = \pm\frac{\vec{p}'_\pi}{|\vec{p}'_\pi|}. \tag{2.15}$$

As it will be shown later, for the simulation of the EDM effect in the MC, it is necessary to reconstruct the τ spin vector also for the background events,

therefore the spin reconstruction formulae for the main τ decay channels characterized by just one charged particle are also reported.

For theτ leptonic decays,

$$\tau^{\pm}(\vec{k}'_{\pm}, \vec{S}_{\pm}) \to l^{\pm}(\vec{p}'_{l})\nu_{\tau}(\vec{q}'_{\tau})\nu_{l}(\vec{q}'_{l}),$$

where $l^{\pm} = \mu^{\pm}, e^{\pm}$ and momenta are expressed in the single τ rest frame, we have:

$$\vec{h}_{\pm} = \mp \frac{(4E'_l - m_l - \frac{3m_l^2}{m_\tau})/E'_l}{3m_l - 4E'_l - \frac{2m_l^2}{E'_l} + \frac{3m_l^2}{m_\tau}} \vec{p}'_l. \tag{2.16}$$

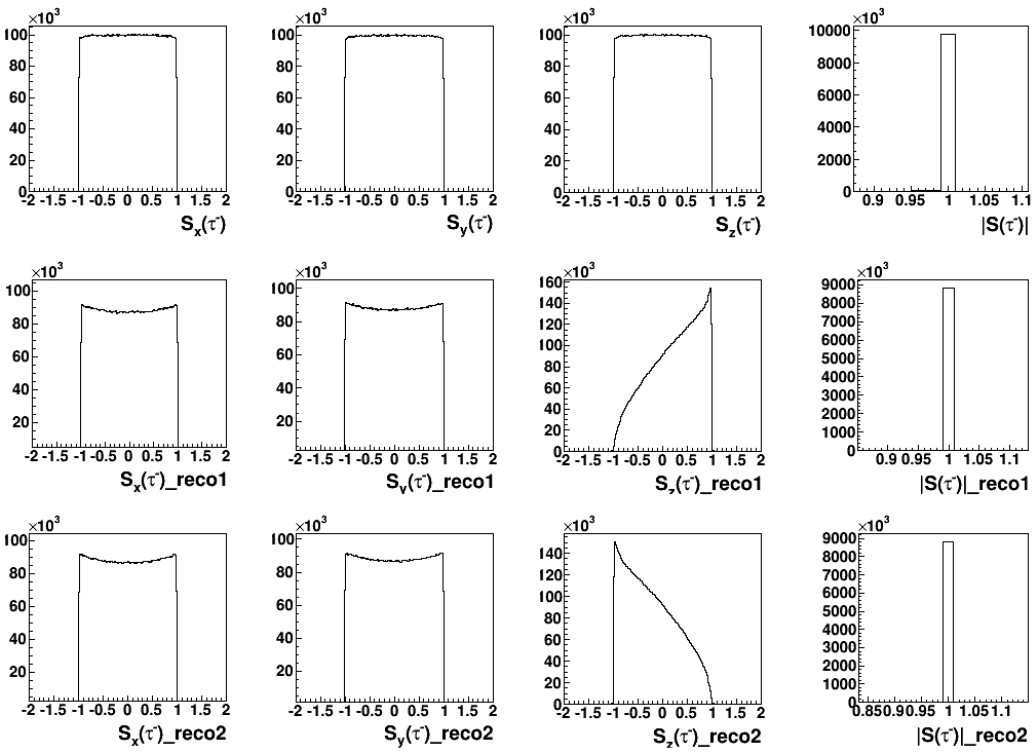

Figure 2.5: Distribution of the τ^- spin vector components and module, calculated in the $\tau^- \to \pi^-\nu_\tau$ case. Top: spin vector obtained with the true τ^- momentum. Middle and bottom: spin vectors obtained with the two τ^- momentum solutions ($+\Delta$ and $-\Delta$ in Eq. 2.13 respectively).

For the hadronic decay through ρ resonance,

$$\tau^{\pm}(\vec{k}'_{\pm}, \vec{S}_{\pm}) \to \rho^{\pm}(\vec{p}'_{\rho})\nu_{\tau}(\vec{q}'_{\tau}) \to \pi^{\pm}(\vec{p}_{\pi})\pi^{0}(\vec{p}_{\pi^0})\nu_{\tau}(\vec{q}'_{\tau}),$$

we have:

$$\vec{h}_{\pm} = \pm m_\tau \frac{2(\vec{p}\,' \cdot \vec{q}\,'_\tau)\vec{p}' - (p')^2 \vec{q}\,'_\tau}{2(\vec{p}\,' \cdot \vec{q}\,'_\tau)(\vec{p}\,' \cdot \vec{k}\,'_\pm) - (p')^2 (\vec{q}\,'_\tau \cdot \vec{k}\,'_\pm)}, \tag{2.17}$$

where $\vec{p}\,' = \vec{p}\,'_\pi - \vec{p}\,'_{\pi^0}$.

Transforming particle energies and momenta from the single τ rest frame to the τ-pair rest frame we are working on, we have:

$$\begin{aligned} \vec{p}\,' =& \vec{p} + \frac{\gamma - 1}{\beta^2}(\vec{\beta} \cdot \vec{p})\vec{\beta} + \gamma E \vec{\beta}, \\ E' =& \gamma(E + \vec{\beta} \cdot \vec{p}), \end{aligned} \tag{2.18}$$

with $\vec{\beta} = -\vec{k}_\pm / E_\tau$, $\gamma = E_\tau / m_\tau$ and $\vec{k}_\pm = \pm \vec{k}$. E and $\vec{k}$ being defined in the τ-pair rest frame.

Then, for the spin vector reconstruction formulae in the CM frame, sobstituting relations 2.18 in Eq. 2.15, 2.16 and 2.17, using the 4-vector formalism $k = (E_\tau, \vec{k})$, and considering that the relation between polarimeter and spin vector is $\vec{S} \equiv -\vec{h}$, we obtain for these decay modes:

- $\tau^\pm(\vec{k}_\pm, \vec{S}_\pm) \to \pi^\pm(\vec{p}_{\pi^\pm})\nu_\tau(\vec{q}_\tau)$

$$\vec{S}_\pm = \pm \frac{2}{m_\tau^2 - m_\pi^2} \left(-m_\tau \vec{p}_{\pi^\pm} + \frac{m_\tau^2 + m_\pi^2 + 2m_\tau E_{\pi^\pm}}{2(E_\tau + m_\tau)} \vec{k} \right), \tag{2.19}$$

- $\tau^\pm(\vec{k}_\pm, \vec{S}_\pm) \to l^\pm(\vec{p}_{l^\pm})\nu_\tau(\vec{q}_\tau)$, where $l^\pm = \mu^\pm, e^\pm$

$$\vec{S}_\pm = \frac{4c_\pm - m_\tau^2 - 3m_l^2}{3m_\tau^2 c_\pm - 4c_\pm^2 - 2m_l^2 m_\tau^2 + 3c_\pm m_l^2} \left(\pm m_\tau \vec{p}_l - \frac{c_\pm + E_{l^\pm} m_\tau}{E_\tau - m_\tau} \vec{k} \right), \tag{2.20}$$

  where $c_\pm = E_\tau E_l \mp \vec{k} \cdot \vec{p}_l$.

- $\tau^\pm(\vec{k}_\pm, \vec{S}_\pm) \to \rho^\pm(\vec{p}_{\rho^\pm})\nu_\tau(\vec{q}_\tau) \to \pi^\pm(\vec{p}_{\pi^\pm})\pi^0(\vec{p}_{\pi^0})\nu_\tau(\vec{q}_\tau)$

$$\vec{S}_\pm = \mp \frac{1}{(k_\pm H_\pm) - m_\tau^2 (p_{\pi^\pm} - \vec{p}_{\pi^0})^2} \left(-H_0^\pm \vec{k} + m_\tau \vec{H}^\pm + \frac{\vec{k}(\vec{k} \cdot \vec{H}^\pm)}{E_\tau + m_\tau} \right), \tag{2.21}$$

  where $(\vec{H}^\pm)^\nu = 2(p_{\pi^\pm} - \vec{p}_{\pi^0})^\nu (p_{\pi^\pm} - \vec{p}_{\pi^0})^\mu (k_\pm)_\mu + (p_{\pi^\pm} + \vec{p}_{\pi^0})^\nu (p_{\pi^\pm} - \vec{p}_{\pi^0})^2$.

The full procedure to obtain these formulae is illustrated in Appendix B for the case $\tau^{\pm} \to \rho^{\pm}\nu_{\tau}$ [34].

In Fig. 5.6 and 5.5 we show the distribution of the spin vectors components (S_x, S_y, S_z) and module $(|\vec{S}|)$, for τ^- and τ^+, respectively, in the case of $\tau^{\pm} \to \pi^{\pm}\nu_{\tau}$ decay. On top are the spins obtained with the true τ momentum MC information. Middle and bottom plots represent the two spins obtained with the two possible τ momentum solutions. In half cases the correct solution is the first, in half cases is the second one. The asymmetry observed in the two distributions of the z-component is due to the opposite behaviour of the two solutions along the boost axis.

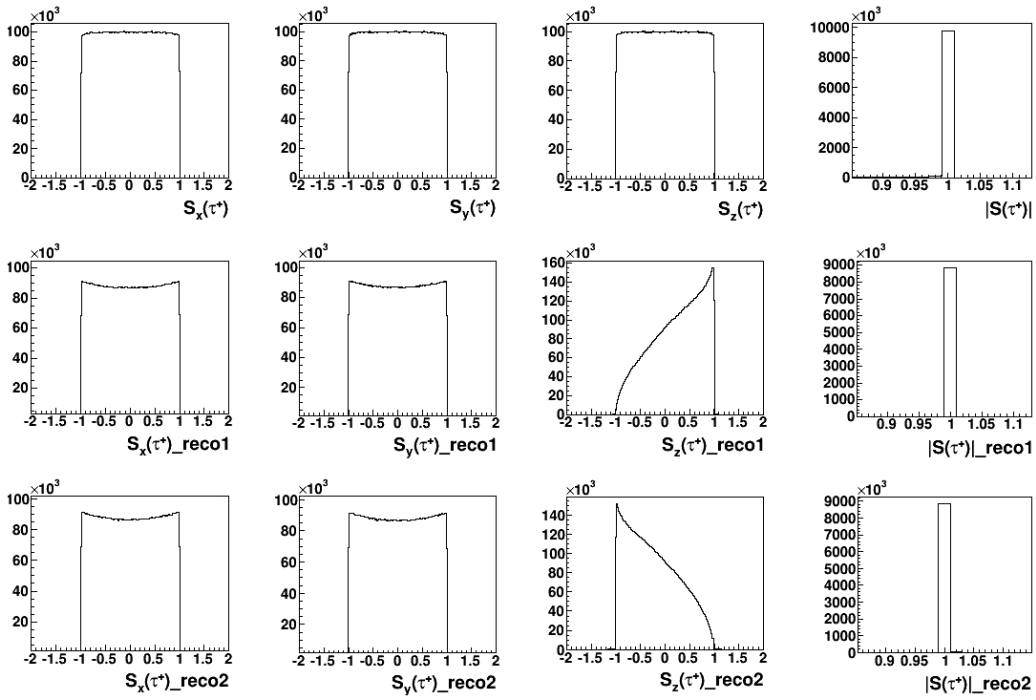

Figure 2.6: Distribution of the τ^+ spin vector components and module, calculated in the $\tau^+ \to \pi^+\bar{\nu}_{\tau}$ case. Top: spin vector obtained with the true τ^+ momentum. Middle and bottom: spin vectors obtained with the two τ^+ momentum solutions ($+\Delta$ and $-\Delta$ in Eq. 2.13 respectively).

2.2.3 Observables estimate from experimental data

With the two hypothesis of τ^+ flight direction $\hat{k}$ and spin τ^+ and τ^- vectors $\vec{S}_{\pm}$, two different values of the matrix elements $\mathcal{M}^2_{SM}$, $\mathcal{M}^2_{Re}$ and $\mathcal{M}^2_{Im}$ are calculated event-by-event. To build up the observables given by Eq.2.3 the average over the two matrix values is used:

$$\mathcal{M}_i^2 = \frac{(\mathcal{M}_i^2)_{reco1} + (\mathcal{M}_i^2)_{reco2}}{2}, \tag{2.22}$$

where i stands for SM, Re, Im.

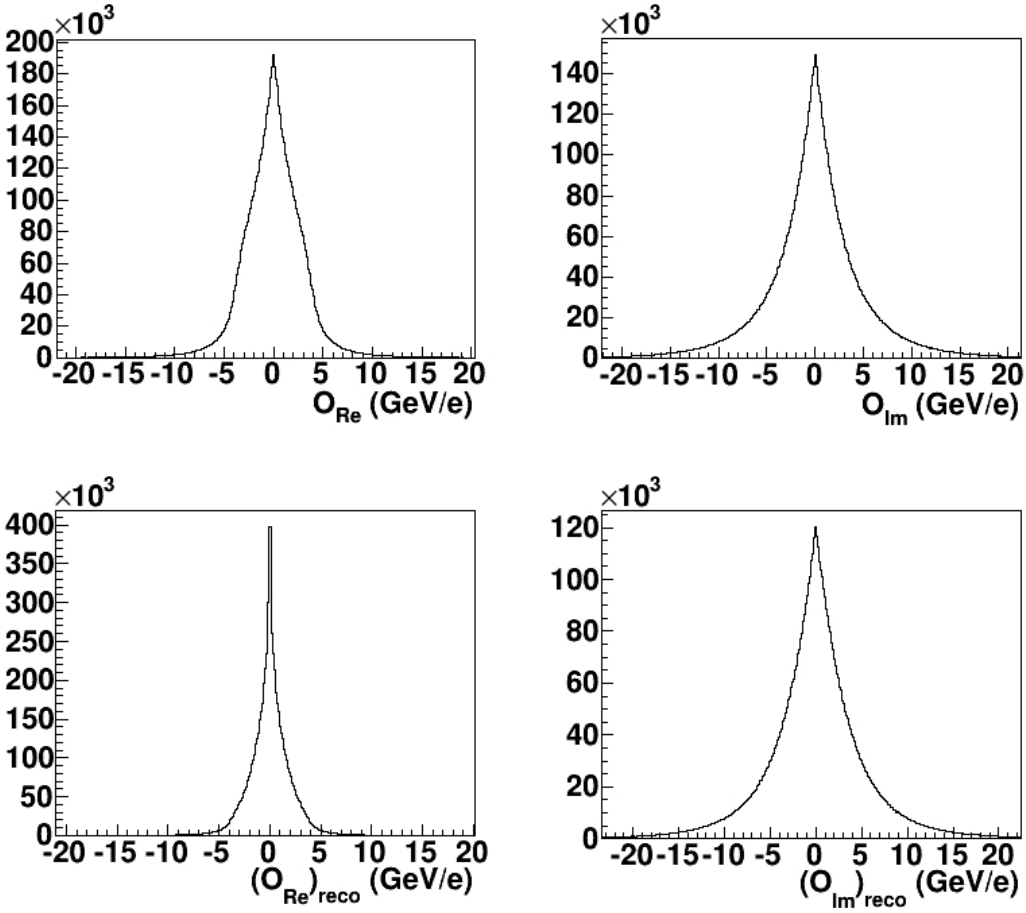

Figure 2.7: Real (left) and imaginary (right) observable distributions obtained with the real τ generated momentum (up) and with the spin density matrix averaged over the matrix elements given by the two possible τ momentum solutions (down).

In Fig. 2.7 we show the real (left) and imaginary (right) observable distributions obtained with a pure $e^+e^- \to \tau^+\tau^- \to \pi^+\pi^-\nu_\tau\bar{\nu}_\tau$ MC sample of 10^7 events. In the first line the observables calculated with the true τ momentum are displayed, in the second line the observables obtained with the spin density matrix averaged over the two values obtained with the τ momentum reconstruction are displayed. In the real observable case the average between the correct and uncorrect solutions brings to a significanlty shrinked distribution.

2.3 Modeling the EDM effect in the MC

The real and imaginary EDMs can be extracted using the linear relation of Eq. 2.5 as described in the section 2.1. The sensitivity a_j and the offset b_j can be expressed by the following equations (where j stands for Re, Im):

$$\tilde{a}_j = \int \frac{(\mathcal{M}_j^2)^2}{\mathcal{M}_{SM}^2} d\phi \ , \ \ \tilde{b}_j = \int \mathcal{M}_j^2 d\phi. \tag{2.23}$$

However, the measurable mean value of the observable depends on the experimental acceptance $\eta(\phi)$, as (analogous expression for the imaginary part):

$$\begin{aligned} \langle \mathcal{O}_{Re} \rangle &\propto \int \mathcal{O}_{Re}\, \eta(\phi) \mathcal{M}_{prod}^2 d\phi \\ &= \int \eta(\phi) \mathcal{M}_{Re}^2 d\phi + Re(d_\tau) \int \eta(\phi) \frac{(\mathcal{M}_{Re}^2)^2}{\mathcal{M}_{SM}^2} d\phi \\ &= b_{Re} + Re(d_\tau) \cdot a_{Re}, \end{aligned} \tag{2.24}$$

where a_{Re} and b_{Re} represent the experimental conversion parameters given by:

$$a_j = \int \eta(\phi) \frac{(\mathcal{M}_j^2)^2}{\mathcal{M}_{SM}^2} d\phi \ , \ \ b_j = \int \eta(\phi) \mathcal{M}_j^2 d\phi. \tag{2.25}$$

These parameters, necessary to extract the EDM from the observables, cannot be calculated analytically, but must be extracted from the correlation between $\langle \mathcal{O}_{Re} \rangle$ ($\langle \mathcal{O}_{Im} \rangle$) and $Re(d_\tau)$ ($Im(d_\tau)$) obtained by a full MC simulation including the acceptance effects of the *BABAR* detector.

Events characterized by the EDM effect are simulated by using the standard MC sample weighted by:

$$w = \frac{(\mathcal{M}_{prod}^2)_{EDM}}{\mathcal{M}_{SM}^2} = \frac{\mathcal{M}_{SM}^2 + Re(d_\tau)\mathcal{M}_{Re}^2 + Im(d_\tau)\mathcal{M}_{Im}^2 + |d_\tau|^2 \mathcal{M}_{d^2}^2}{\mathcal{M}_{SM}^2}, \tag{2.26}$$

where different values of $Re(d_\tau)$ and $Im(d_\tau)$ are introduced.

Since in the final analysis the MC events are generated and reconstructed with the all conceivable experimental effects, such as undetected radiative photons, detector resolution and apparatus acceptance, the extracted parameters, a_j and b_j, can be applied to the experimental data. We will estimate in the last chapter the systematic uncertainties associated with this procedure.

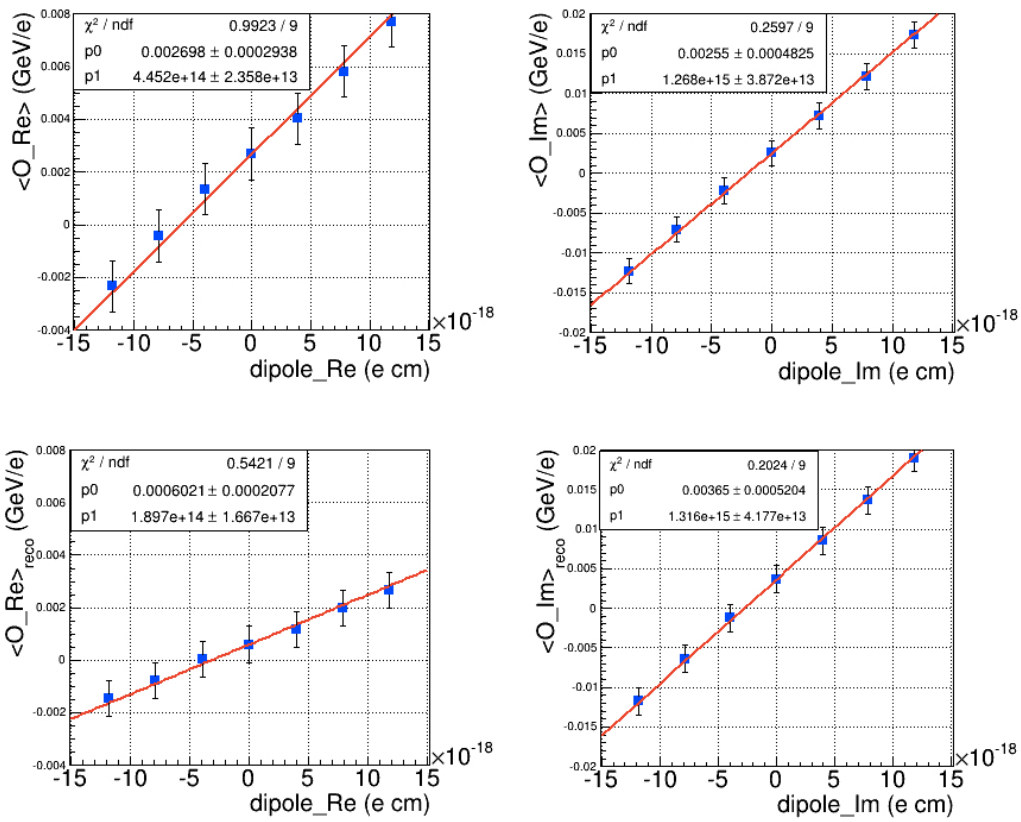

Figure 2.8: Real (left) and imaginary (right) observable mean vs real and imaginary dipole moment variation. Top: observable distributions obtained with the real τ generated momentum. Bottom: observable distributions obtained with the τ momentum reconstruction and matrix element averaged.

2.4 EDM sensitivity

Fig 2.8 shows the correlation between $\langle \mathcal{O}_{Re} \rangle$ (left) and $\langle \mathcal{O}_{Im} \rangle$ (right) and $Re(d_\tau)$ and $Im(d_\tau)$ respectively. In the upper plots the mean is calculated on the observable distribution obtained with the true τ generated momentum. The lower plots represent the experimentally measurable case, where the mean is calculated on the observable distribution obtained with the average of the two reconstructed matrix elements.

In the Eq. 2.26 the dipole moment is expressed in $[\mathrm{GeV}^{-1} \cdot e]$, $\mathcal{M}^2_{Re}$ and $\mathcal{M}^2_{Im}$ dimensions are $[\mathrm{GeV} \cdot e^3]$, $\mathcal{M}^2_{SM}$ has the amplitude dimensions $[e^4]$. In the plots of Fig.2.8 we employ the conversion factor $1\,\mathrm{GeV}^{-1} = 0.1976 \cdot 10^{-13}$ cm to be coherent with the conventional electric dipole moment units used in literature.

The points $\langle \mathcal{O}_j \rangle$ reported in the plot are given by the mean of the ob-

servable distributions illustrated in Fig. 2.7 obtained for the different EDM values. These points are correlated because the EDM effect is evaluated on the same MC sample using different weights.

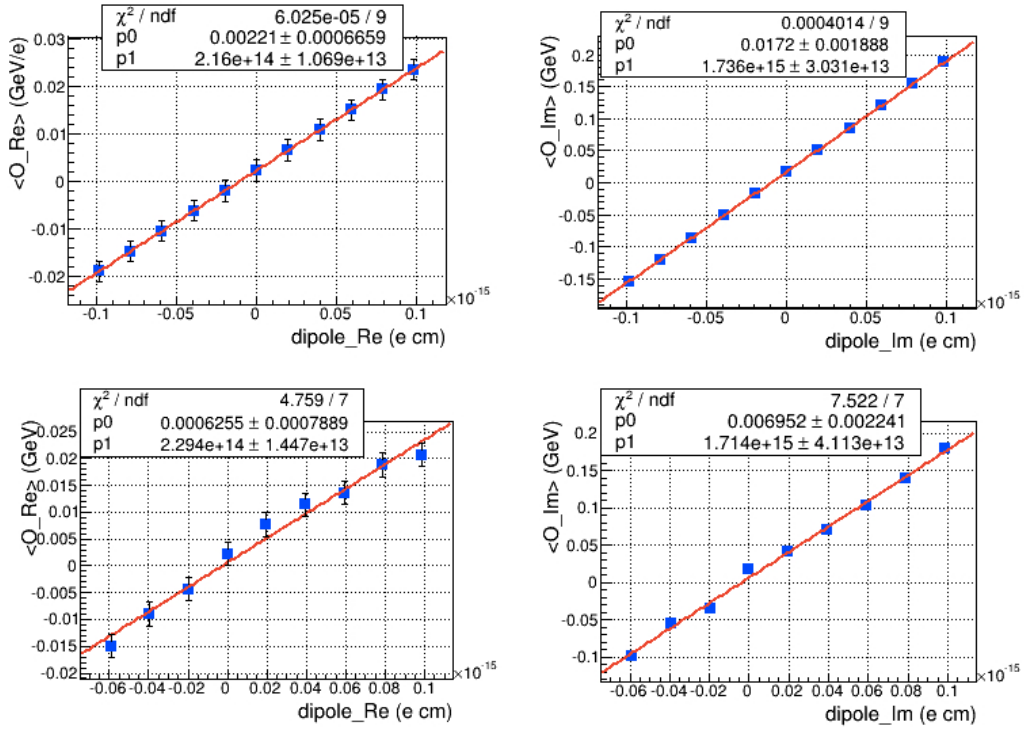

Figure 2.9: Real (left) and imaginary (right) observable means vs real and imaginary dipole moment variation. Top: the same 10^6 MC sample is used. Bottom: for each EDM value a different MC sample of 10^6 events is used.

In Fig.2.9 the case of the same MC sample (10^6 events) in which different EDM values are introduced is compared with the case of different MC samples (10^6 events) used for each EDM value.

The EDM sensitivity a_j is determined by the slope and the statistical error of the single mean measurement. The offset b_j is given by the observable mean in the EDM = 0 case.

For the real part of EDM, the sensitivity is significantly reduced by the τ momentum ambiguity. Indeed, as shown with the Eq.2.6, the wider distribution reflects the higher sensitivity and the width becomes smaller when the average of the amplitudes over the τ direction is taken (see Fig.2.7). On the contrary, the imaginary EDM sensitivity is not affected by the average procedure. From the left bottom plot we can see that an ideal sample of 10^7 signal events would be sensitive at 2σ to a $Re(d_\tau)$ of the order of 10^{-17} e cm.

Chapter 3

The *BaBar* Experiment

The *BABAR* experiment, located at the Stanford Linear Acceletator Center (SLAC) in California, collected data between October 1999 and April 2008, with a primary aim of measuring CP violation in the decay of neutral B mesons. The experiment consisted of a detector [35] built around the interaction region of the high luminosity e^+e^- asymmetric collider PEP-II [36] running at and around the $\Upsilon(4S)$ resonance. Although designed primarily for B physics, the high luminosity of the PEP-II accelerator coupled with the relatively large cross section for τ pairs at a center of mass energy 10.58 GeV made the *BABAR* facility also a τ factory, allowing a large secondary physics program in this area.

In this chapter the main features and the performance of PEP-II accelerator and the *BABAR* detector will be described.

3.1 The PEP-II Accelerator

The PEP-II Accelerator, shown in Fig. 3.1, is an asymmetric electron positron collider. Electrons and positrons are accelerated in the 3.2 Km long SLAC linac and accumulated into two storage rings 2.2 Km long, called HER (high-energy ring), in which electrons with energy of 9.0 GeV circulate, and LER (low-energy ring), in which 3.1 GeV positrons, produced in the linac by collisions of 30 GeV electrons on a target, circulate. In the centre-of-mass frame, the collision energy corresponds to the mass of the $\Upsilon(4S)$ particle, a resonant state composed by a b and $\bar{b}$ quark with a mass of 10.58 GeV/c^2.

The $\Upsilon(4S)$ mass is slightly above the energy threshold for $B\bar{B}$ production, resulting in a decay rate greater than 96% into $B^0\bar{B}^0$ and B^+B^- particles, providing the large sample of B mesons required for the *BABAR* physics goals. The collision products experience a Lorentz boost of $\beta\gamma = 0.56$ in the

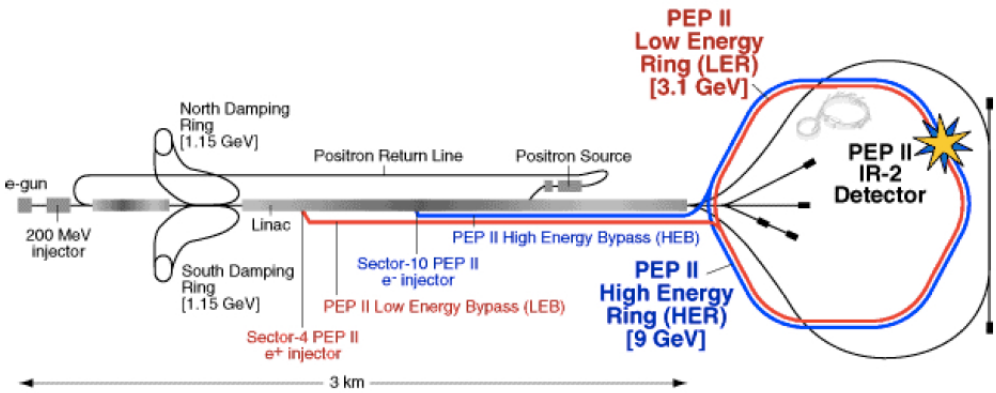

Figure 3.1: Diagram illustrating the linear accelerator and the PEP-II storage rings.

laboratory frame, which implies that the two B mesons travel a measurable distance ($\sim 250\mu$m) before decaying. This allows the determination of their relative decay times and enables a study of CP violation.

At $\sqrt{s} = 10.58$ GeV, e^+e^- collisions also produce a large number of τ lepton pairs. Cross sections for the main physics processes are given in table 3.1.

$e^+e^- \to$	σ (nb)
$b\bar{b}$	1.05
$c\bar{c}$	1.30
$s\bar{s}$	0.35
$d\bar{d}$	0.35
$u\bar{u}$	1.39
$\mu^+\mu^-$	1.16
$\tau^+\tau^-$	0.92
$e^+e^-(17^\circ < \theta < 160^\circ)$	21.2
$e^+e^-(20^\circ < \theta < 120^\circ)$	14.4

Table 3.1: Production cross sections for e^+e^- colliding at 10.58 GeV.

BABAR has recorded an integrated luminosity of about 531 fb^{-1}, including about 54 fb^{-1} collected at an energy approximately 40 MeV below the $\Upsilon(4S)$ resonance, 433 fb^{-1} recorded at $\Upsilon(4S)$ and 44 fb^{-1} at the $\Upsilon(3S)$ and $\Upsilon(2S)$ resonances. The luminosity recorded during the *BABAR* lifetime is shown in Fig. 3.2. PEP-II surpassed its design performance of 3×10^{33} cm^{-2} s^{-1} and

achieved a maximum instantaneous luminosity of 1.2×10^{34} cm^{-2} s^{-1} during the last Run-Cycle.

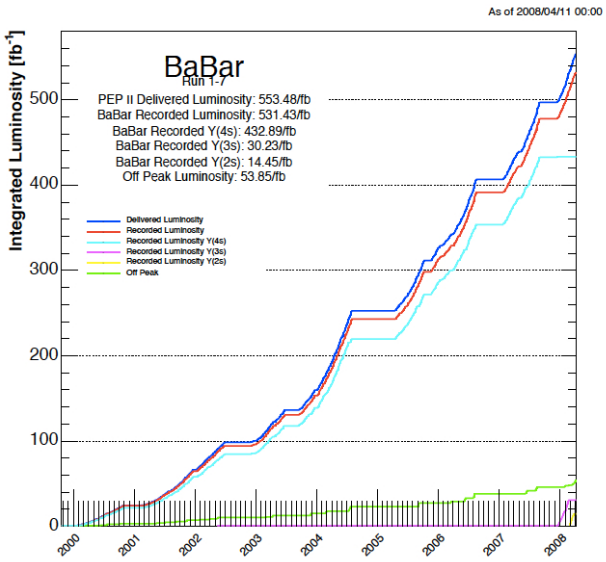

Figure 3.2: PEP-II delivered and *BABAR* recorded integrated luminosity in Run 1 to Run 7 (from October 1999 to April 2008)

3.2 The e^+e^- interaction

The *BABAR* detector was located at the second interaction region of the PEP-II main rings. The electron and positron beams are manipulated through bending, by dipole magnets and focused by quadrupole magnets so that they collide approximately along the central axis of the *BABAR* detector at the *interaction point* (IP). CsI(Tl) scintillating crystals positioned beside the beam pipe are utilized to monitor the focusing of the beams. The interaction region is enclosed in a water-cooled beam pipe consisting of two thin layers of beryllium with a water channel in between. Its outer radius is about 28 mm. The total thickness of the central beam pipe at normal incidence corresponds to 1.06% of radiation length.

In a high current machine like PEP-II, the interaction region produces several significant sources of background. The quadrupole and dipole magnets, which are located close to the interaction region to maximize the focusing of the beam, produce sychrotron radiation as the trajectory of the beam is altered to stop the radiation interacting with the beam pipe. Another major source of beam-induced background is beam-gas scattering, where beam

particles lose energy through bremsstrahlung and Coulomb scattering with gas molecules in the beam pipe. With a lower energy, these *lost* particles are deflected of different amounts by the magnets and can interact with the beam pipe causing electromagnetic showers. This background is reduced by maintaining a vacuum of order of 10^{-10} torr in the beam pipe and by installing collimators upstream the detector. The final major source of beam background is generated by off-energy outgoing electrons and positrons from radiative Bhabha scattering ($e^+e^- \to e^+e^-\gamma$). The resulting energy-degraded particles can interact with the beam pipe, causing electromagnetic showers within a few metres of the IP. This background source is strictly linear with the luminosity. In addition there are other sources of background such as the beam particles not at the correct momentum for stable storage in the ring that interact with the magnets and the beam pipe. To reduce the accumulation of unnecessary doses to the detector, potential high radiation regions are shielded by the addition of extra material.

3.3 The *BaBar* Detector

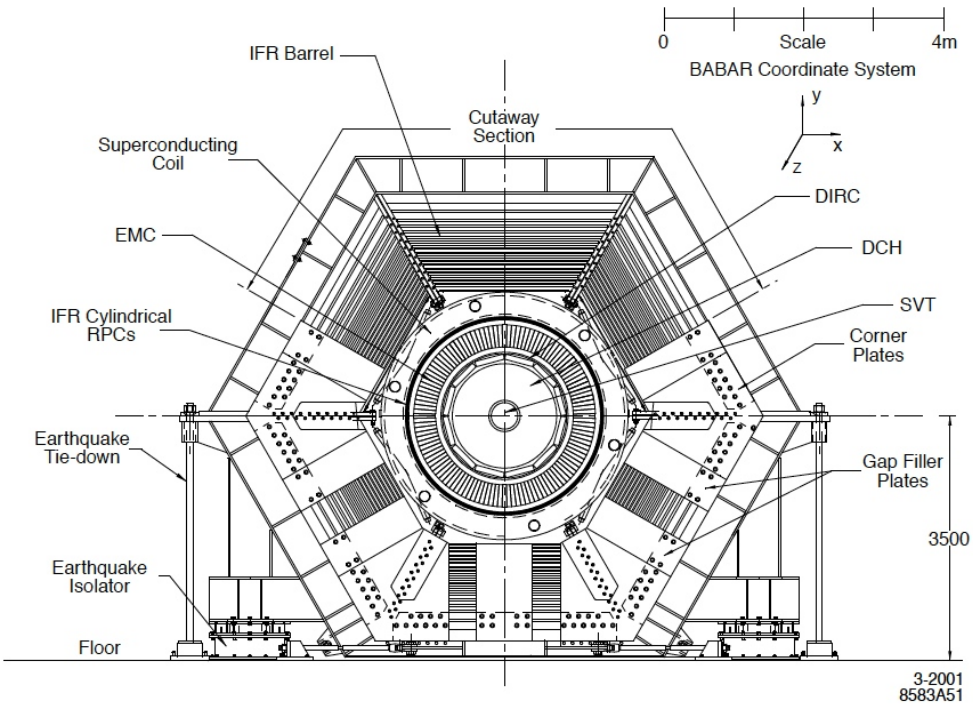

Figure 3.3: Transverse section of the *BABAR* detector. Distances are in mm and the components are described in the text.

The *BABAR* physics program required a detector with a large and uniform acceptance, in particular down to small polar angles relative to the boost direction, to avoid particle losses. The performance optimization led to an asymmetric design of the detector characterized by good vertex resolution; excellent detection efficiency and precision on the momentum measurement for charged particles with transverse momentum ranging between 60 MeV/c and 4 GeV/c; excellent energy and angular resolution for photons and π^0 with energy down to 20 MeV and up to 5 GeV; good discrimination between e, μ, π, K, p over a wide kinematic range and neutral hadrons identification capability.

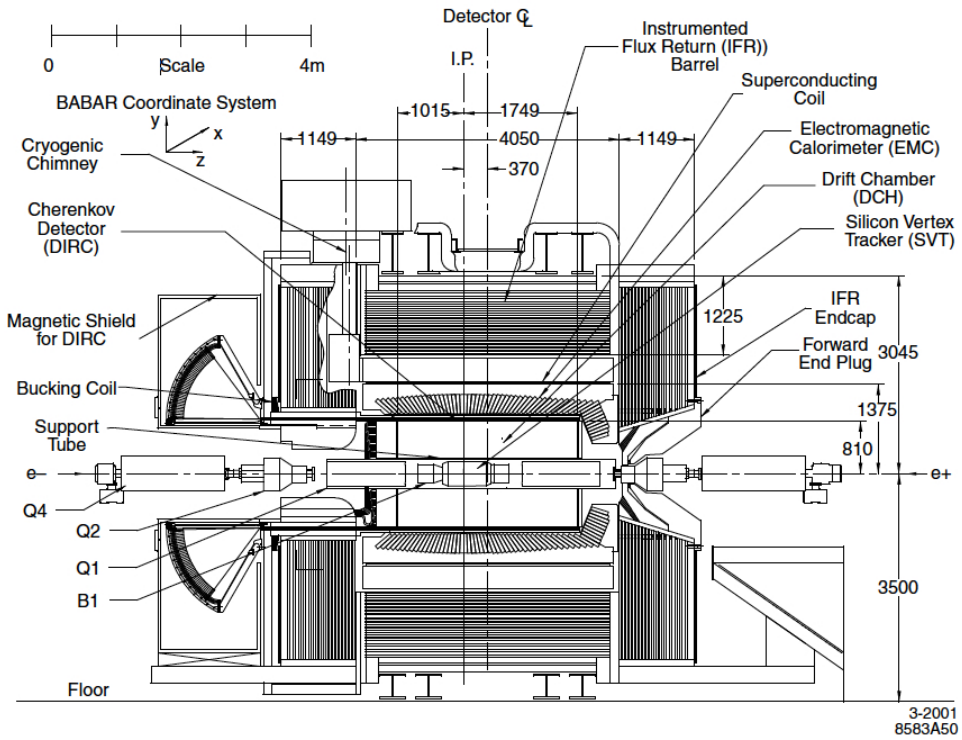

Figure 3.4: Longitudinal section of the *BABAR* detector. Distances are in mm and the components are described in text.

The detector is made up of several subsystems, as shown in Fig. 3.3 and Fig. 3.4. From the beam pipe and working outwards these systems are:

- The Silicon Vertex Tracker (SVT) - for charged particles detection and momentum measurement;
- The Drift Chamber (DCH) - for charged particles detection and momentum measurement;

- The Internally Reflected Cherenkov radiation Detector (DIRC) - for particle identification;
- The Electromagnetic Calorimeter (EMC) - for detection of photons and electrons;
- The Superconducting Solenoid - which produces a 1.5 T axial magnetic field;
- The Instrumented Flux Return (IFR) - for muon identification and detection of penetrating neutral hadrons.

The right-handed coordinate system is indicated in Fig. 3.3 and Fig. 3.4. The z axis corresponds to the magnetic field axis and is offset relative to the beam axis by $\sim$ 20 mrad in the horizontal plane (tilt). It is oriented in the direction of electrons. The positive y-axis points upward and the positive x-axis points away from the center of the PEP-II storage rings.

3.3.1 The Silicon Vertex Tracker

The Silicon Vertex Tracker (SVT) is the innermost detector positioned around the beam pipe and, toghether with the drift chamber, represent the *BABAR* charged particle tracking system. Both detectors are immersed in the 1.5 T axial magnetic field. The SVT provides a precise measurement of the decay vertices and of the charged particle trajectories near the interaction region. The average vertex resolution along the z-axis for a fully reconstructed B decay is required to be better than 80 μm in order to avoid a significant impact on the time-dependent CP asymmetry measurement precision; a 100 μm resolution in the xy transverse plane was obtained in reconstructing decays of bottom and charm mesons, as well as τ leptons.

The SVT also provides standalone tracking for particles with transverse momentum $<$ 120 MeV/c, too low to reach the drift chamber, like soft pions from D^* decays and many charged particles produced in multi-body B meson decays.

Finally, the SVT supplies particle identification (PID) information, both for low and high momentum tracks, through the measurement of the specific ionization loss derived from the total charge deposited in the detector layers. For low momentum tracks the SVT dE/dx measurement is the only PID information available. It can achieve a 2σ separation between kaons and pions up to a momentum of 500 MeV/c, and between kaons and protons up to a momentum of 1 GeV/c. For high momentum tracks the SVT provides the

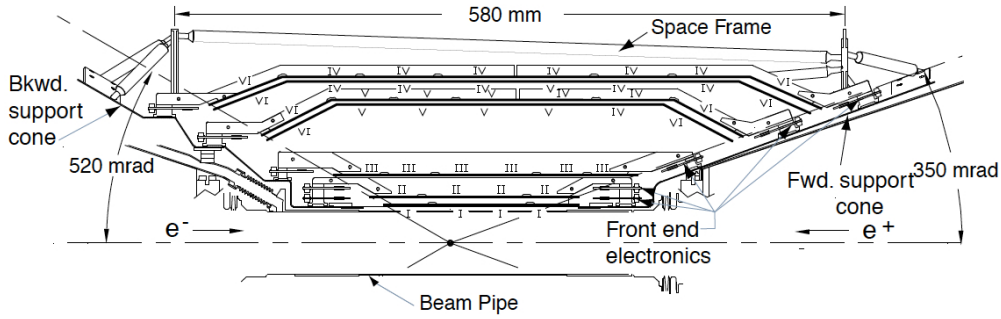

Figure 3.5: Schematic longitudinal section of the SVT.

best measurement of the track angles, which are critical for the uncertainties in the measurement of the Cherenkov angle by the DIRC.

The design of the SVT was constrained by the components of the storage ring which have been arranged so as to maximize the acceptance. The angular coverage of the SVT extends from 20° to −150° in the polar angle from the beam line in the forward direction. Furthermore, it was required to be light in order to reduce the multiple scattering affecting the performance of the outer subdetectors. The readout electronics is mounted entirely outside the active detector volume to minimize the material within the acceptance of the detector.

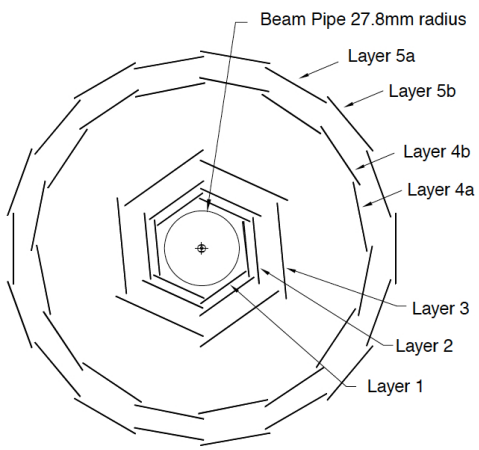

Figure 3.6: Schematic transverse section of the SVT showing how the silicon strip modules are arranged into layers.

The SVT consists of 5 layers of double-sided, 300 μm thick, silicon strip sensors. The strips on the two sides of the sensors are aligned perpendicularly

to each other, giving ϕ and z coordinates. The sensors are organized into modules arranged in 5 concentric layers, as shown in Fig.3.5 and 3.6, resulting in a total active silicon area of 0.96 m^2

The three inner layers provide angle and position information for the measurement of the vertex position. In order to minimize the effect of multiple scattering in the beam pipe, they are mounted as close to the beam pipe as possible with the innermost layer only 32 mm from the IP. To fulfil the physics requirements, the spatial resolution for perpendicular tracks is 10-15 μm. Each layer is composed of 6 planar modules tilted by 5° in ϕ to allow overlap between adjacent modules. This provides full azimuthal coverage and is advantageous for alignment.

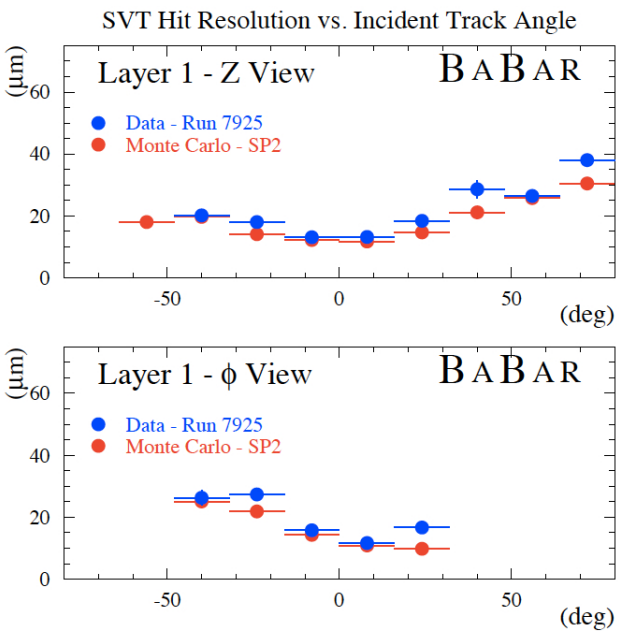

Figure 3.7: SVT resolution (layer 1) on the single hit, as a function of the track incident angle.

The outer two layers provide position and angle measurements to link the tracks with the DCH measurements and they are necessary for pattern recognition and low transverse momentum tracking. The spatial resolution for perpendicular tracks in these outer layers is $\sim$ 40μm. There are 16 modules in the inner and 18 in the external one, placed at radii between 91 mm and 144 mm from the IP.

The SVT efficiency is calculated for each section of the modules by comparing the number of hits associated to a reconstructed track to the number of tracks crossing the active area of the module and is found to be 97%.

The spatial resolution of SVT hits is determined by measuring the distance between the track trajectory and the hit for high-momentum tracks in two-prong events: it is generally better than 40 μm in all layers for all track angles (see Fig. 3.7), allowing a precise determination of decay vertices to better than 70 μm.

The SVT provides stand-alone tracking for low momentum particles that do not reach the drift chamber, with an efficiency estimated to be 20% for particles with transverse momentum of 50 MeV/c, rapidly increasing to over 80% at 70 MeV/c.

3.3.2 The Drift Chamber

The Drift Chamber (DCH) is the main tracking device for charged particles with transverse momenta p_T above $\sim$ 120 MeV/c, providing the measurement of p_T from the curvature of the particle's trajectory in the magnetic field. The DCH also allows the recostruction of secondary vertices located outside the silicon detector volume, such as those from $K_s \to \pi^+\pi^-$ decays. For this purpose, the chamber is able to measure not only the transverse coordinates, but also the longitudinal one (z) with a good resolution (about 1 mm). Good z resolution is also important for matching DCH and SVT tracks, and in projecting tracks to the DIRC and the calorimeter.

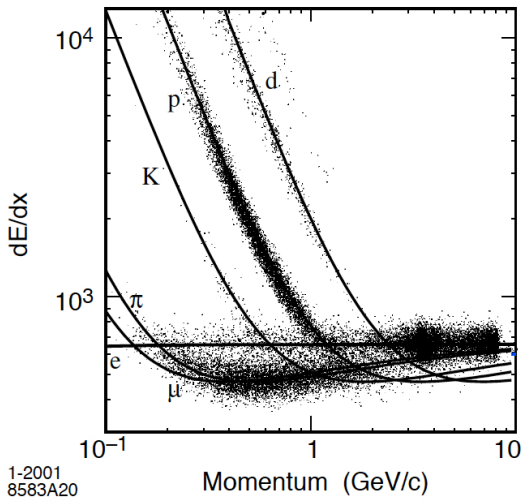

Figure 3.8: Measurement of dE/dx in the DCH versus track momentum. The superimposed Bethe-Bloch curves for particles of different masses have been determined from selected control samples. The large number of protons and deuterons come from beam-background events.

For low momentum particles the DCH complements the DIRC by providing additional PID information. In the extreme backward and forward directions which fall outside the geometrical acceptance of the DIRC, the DCH provides the only particle identification. This is done by measuring the energy lost by ionization (dE/dx), from the measurement of total charge deposited in each drift cell. The type of particle can be determined by the relationship between the value of dE/dx and the momentum, as shown in Fig. 3.8. A dE/dx resolution of $\sim 7\%$ allows a 3σ K/π separation up to 700 MeV/c momenta [37]. In Fig. 3.9 the resolution measured for $e^{\pm}$ from Bhabha scattering is shown.

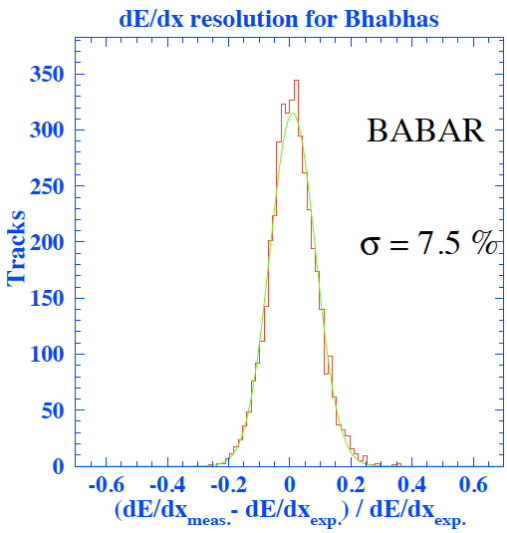

Figure 3.9: Resolution dE/dx for $e^{\pm}$ from Bhabha scattering.

Finally, the DCH provides real-time information used in the first level trigger system.

The DCH is a 2.80 m long cylinder with an inner radius of 23.6 cm and an outer radius of 80.9 cm (Fig. 3.10). To cope with the asymmetry of the beam energies, the DCH center is displaced by about 37 cm with respect to the interaction point in the forward direction. The active volume provides charged particle tracking over the polar angle range $-0.92° < \theta < 0.96°$.

The DCH walls are kept thin to reduce background, improve the matching with the SVT tracks and not to degrade the DIRC and EMC performance. Overall the DCH material corresponds to less than 0.2% radiation lenght.

Inside the DCH there are 7104 hexagonal drift cells filled with a He based gas mixture. Each of them is about 12 mm in the radial direction and 19 mm in the azimuthal one and consists of one sense wire sorrounded by six field wires The drift cells are arranged in 10 superlayers of 4 layers each,

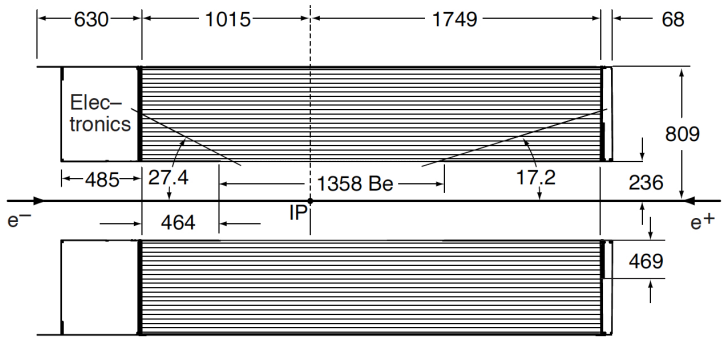

Figure 3.10: Longitudinal section of the DCH with dimensions in mm.

for a total of 40 concentric layers. Sequential layers are staggered by half a cell, enabling left-right ambiguity resolution within a super-layer, even if one of the four signals is missing. Longitudinal position information is obtained aligning part of the wires along the z-axis and part at small angles with respect to the z-axis.

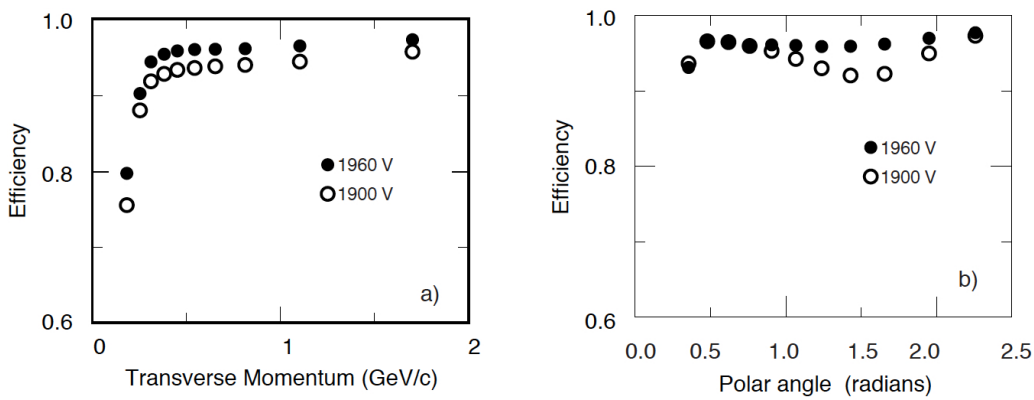

Figure 3.11: Track reconstruction efficiency in the drift chamber at operating voltage of 1900 V and 1960 V, as a function of transverse momentum (a) and polar angle (b).

The drift chamber reconstruction efficiency has been measured in selected samples of multi-track events by exploiting the fact that tracks can be reconstructed independently in the SVT and the DCH. The absolute drift chamber tracking efficiency is determined as the fraction of all tracks detected in the SVT which are also reconstructed by the DCH when they fall within its acceptance. Its dependence on the transverse momentum and polar angle is shown in Fig. 3.11. At the standard operation voltage of 1960 V applied

to the sense wire, the reconstruction efficiency of the drift chamber averages $98 \pm 1\%$ for tracks above 200 MeV/c and polar angle $\theta > 500$ mrad.

The p_T resolution was measured as a function of p_T in cosmic ray studies:

$$\frac{\sigma_{p_T}}{p_T} = (0.13 \pm 0.01)\% \cdot p_T + (0.45 \pm 0.03)\%, \tag{3.1}$$

where p_T is expressed in GeV/c. The first contribution, dominating at high p_T, comes from the curvature error due to finite spatial measurement resolution; the second contribution, dominating at low momenta, is due to multiple Coulomb scattering.

3.3.3 The Cherenkov Detector

The PID at low momenta exploits the dE/dx measurements in the DCH and SVT. However, above the threshold of 700 MeV/c, the dE/dx information does not allow to separate pions and kaons. The Detector of Internally Reflected Cherencov radiation (DIRC) is employed primarily for the separation of pions and kaons from about 500 MeV/c to the kinematic limit of 4 GeV/c reached in rare B decays like $B \to \pi^+\pi^-/K^+K^-$.

Cherenkov light is generated by a charged particle in a medium of refractive index n, when the particle velocity v is greater than c/n. The Cherenkov photons are emitted on a cone of half-angle θ_C with respect to the particle direction, where $cos\theta_C = 1/\beta n$ with $\beta = v/c$. Knowing the particle momentum thanks to the SVT and the DCH, the measurement of θ_C allows the mass measurement and then the particle identification, with the relation:

$$m^2c^2 = \frac{1-\beta^2}{\beta^2}p^2 \tag{3.2}$$

The relationship between the Cherenkov angle and the particle momentum as measured in the DIRC for an inclusive sample of multi-hadron events, is reported in Fig. 3.12.

The DIRC is based on the principle that the angles are maintained upon reflection from a flat surface, as shown in Fig.3.13 which illustrates light production, transport, and imaging. The DIRC has a geometrical acceptance from 25.5° to 147° in the laboratory frame.

For particles with β approximately equal to one, some photons will always lie within the limit for total reflection. This radiation will then be transported via internal reflections preserving the Cherenkov angle.

The radiator material used is synthetic fused silica because of its resistance to ionizing radiation, its long attenuation length, large refraction

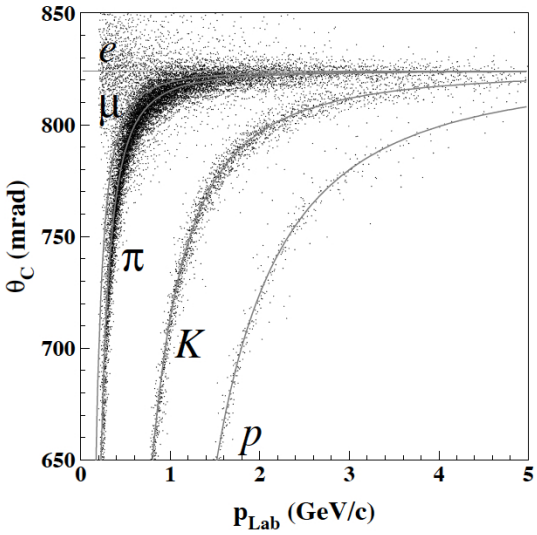

Figure 3.12: The Cherenkov angle, θ_C, of tracks from an inclusive sample of multi-hadron events plotted vs the momentum of the tracks at the entrance of the DIRC. The lines are the predicted values of θ_C for different particle types.

index ($n = 1.437$), low chromatic dispersion and because it allows an excellent optical polishing of the reflecting surfaces. The DIRC is composed of 12 hermetically sealed containers called bar boxes, each containing 12 bars 17 mm thick, 35 mm wide and 4.9 m long. The bars are optically isolated and act as radiator and light pipe transporting the light trapped by total internal reflection.

To avoid interference with other detector systems in the forward region, only the backward end of the bars is instrumented with photon detectors, while a mirror is placed at the forward end to reflect incident photons.

Once photons arrive at the instrumented end, most of them emerge into an expansion region filled with 6000 litres of purified water ($n = 1.364$), called the stand-off box (see also Fig. 3.14). The photons are detected by an array of densely packed photo-multipliers (PMTs) arranged in 12 sectors of 896 phototubes each, placed at a distance of about 1.2 m from the bar end. The expected Cherenkov light pattern at the detection surface is essentially the section of a cone whose opening-angle is the Cherenkov production angle modified by refraction at the exit from the fused silica window. By knowing the location of the PMT that observes a Cherenkov photon and the charged particle direction from the tracking system, the Cherenkov angle can be determined.

In addition, the time taken for the photon to travel from its point of origin to the PMT is used to effectively suppress hits from beam-generated

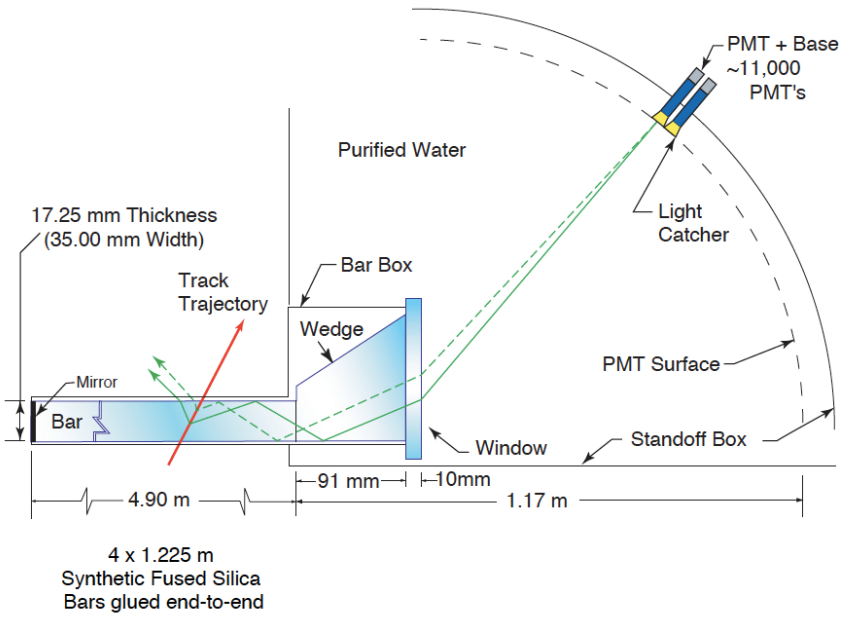

Figure 3.13: Schematic of DIRC fused silica radiator bar and imaging region.

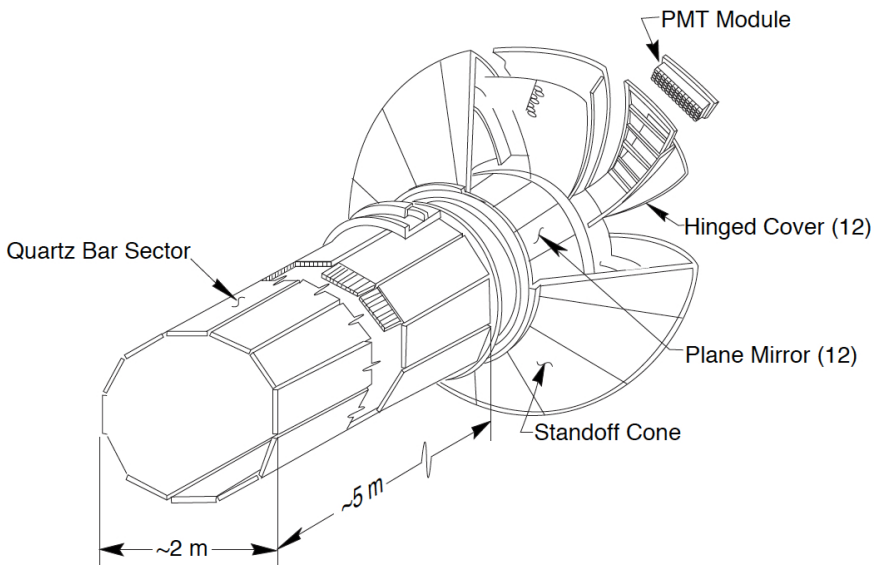

Figure 3.14: Schematic view of the DIRC components.

background and from other tracks in the same event. The difference between the measured and expected time, δ_t, is calculated for each photon and has a resolution, as measured in di-muon events, of 1.7 ns. Applying the time information substantially improves the correct matching of photons with tracks and reduces the number of background hits by approximately a factor 40, as can be seen in Fig. 3.15 [38].

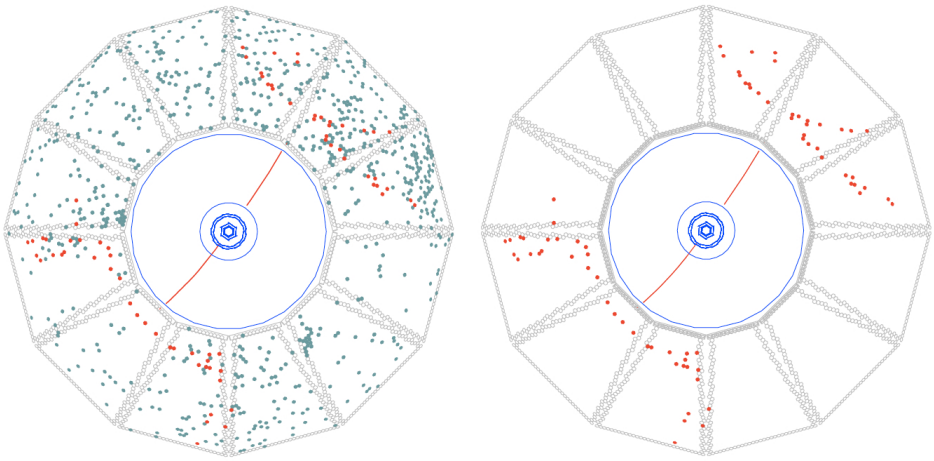

Figure 3.15: Display of one $e^+e^- \to \mu^+\mu^-$ event reconstructed in *BABAR* with two different time cuts. On the left, all DIRC PMTs that where hit within the ± 300 ns trigger window are shown. On the right, only those PMTs that where hit within 8 ns from the expected Cherenkov photon arrival time are displayed.

The number of photons detected increases from a minimum of about 20 for a track crossing at the center of the barrel (polar angle $\theta \simeq 90°$) to well over 50 in the forward and backward directions, corresponding to the fact that the path-length in the radiator is longer for these tracks and the fraction of photons trapped by total internal reflection rises.

The combination of the single photon Cherenkov angle resolution, the distribution of the number of detected photons versus polar angle and the polar angle distribution of charged tracks, yields a typical track Cherenkov angle resolution which is about 2.5 mrad in di-muon events.

The pion-kaon separation power is defined as the difference of the mean Cherenkov angles for pions and kaons assuming Gaussian-like distribution, divided by the measured track Cherenkov angle resolution. As shown in Fig. 3.16, left, the separation between kaons and pions at 3 GeV/c is about 4.3σ. The kaon identification efficiency and pion mis-identification probability, shown as a function of track momentum in Fig. 3.16, right, are on average 96% and 2%, respectively.

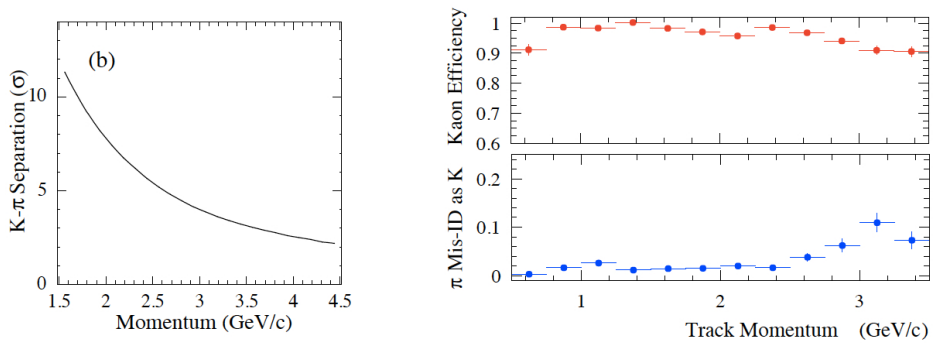

Figure 3.16: Left plot: average difference between the expected value of θ_C for kaons and pions, divided by the uncertainty, as a function of momentum. Right plot: efficiency and misidentification probability for the selection of charged kaons as a function of track momentum.

3.3.4 The Electromagnetic Calorimeter

The Electromagnetic Calorimeter (EMC) is a hermetic, total-absorption calorimeter, made up of 6580 thallium doped cesium-iodide (CsI(Tl)) crystals which are read out with silicon photodiodes. It identifies electrons and photons measuring their energy.

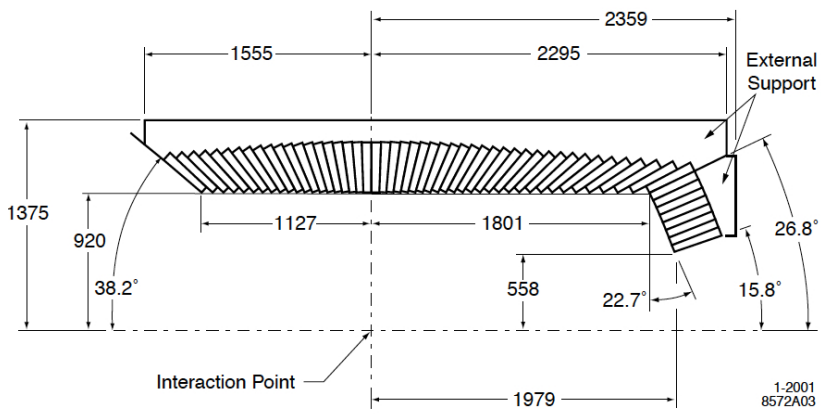

Figure 3.17: Longitudinal section of the top half of the EMC showing the crystals arrangement. Dimensions are in mm.

The EMC measures electromagnetic showers over the energy range from 20 MeV to 9 GeV, where the lower bound is set by the requirement to efficiently reconstruct the $\pi^0 \to \gamma\gamma$ and $\eta \to \gamma\gamma$ decays where the photons can have a very low energy. The upper bound comes from the requirement to

measure quantum electrodynamic (QED) processes (such as $e^+e^- \to e^+e^-(\gamma)$ and $e^+e^- \to \gamma\gamma$) important for calibration and luminosity determination, where the electron and photon energies can be as large as 9 GeV. A typical electromagnetic shower spreads over many adjacent crystals, forming a *cluster* of energy deposit. Pattern recognition algorithms identify these clusters and differentiate between single clusters with one energy maximum and merged clusters with more than one local energy maximun, called *bumbs*. Energy deposit clusters with lateral shape consistent with the expected pattern from an electromagnetic shower, are identified as photons when they are not associated to any charged tracks extrapolated from SVT and DCH, and identified as charged particles if they are matched to an extrapolated track. The separation of electrons and charged hadrons is based primarily on shower energy, lateral shower moments and track momentum. Also, dE/dx energy losses in the DCH and the DIRC Cherenkov angle are required to be consistent with the values that an electron would be expected to produce. The most important variable for the discrimination of hadrons from electrons is the ratio of the shower energy E to the track momentum p, required to be $E/p \sim 1$ for the electrons.

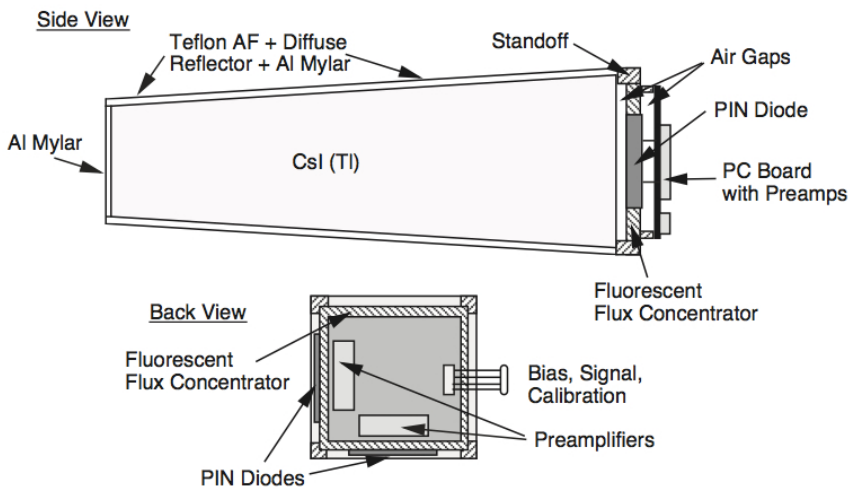

Figure 3.18: A schematic of the wrapped CsI(Tl) crystal and the front-end read-out package mounted on its rear surface (top) and the photo diode (bottom).

Overall the EMC extends from an inner radius of 91 cm to an outer radius of 136 cm and is positioned asymmetrically with respect to the interaction point. It consists of a cylindrical barrel and a forward endcap, as shown in Fig. 3.17; the barrel contains 4760 crystals arranged in 48 rings, while the

endcap holds 820 crystals arranged in 8 rings. The CsI(Tl) crystals have a high light yield (50000 photons/MeV) and a small Molière radius (3.8 cm), providing the required energy and angular resolution; their radiation lenght of 1.86 cm guarantees a complete shower containment at the *BABAR* energies. Each crystal is a truncated trapezoidal pyramid, as shown in Fig. 3.18, with variable heights (16 to 17.5 radiation lenghts). The crystals are arranged to give a 90% solid-angle coverage in the center-of-mass frame. The crystals are read out by two independent 1 cm^2 PIN photodiodes, glued to their rear face, which are connected to low-noise preamplifiers that shape the signal with a short shaping time (400 ns) to reduce soft beam-related photon background.

The efficiency of the EMC exceeds 96% for the detection of photons with energy above 20 MeV. The energy resolution is usually parametrized by:

$$\frac{\sigma_E}{E} = \frac{\sigma_1}{E^{1/4}(GeV)} + \sigma_2 \tag{3.3}$$

where $\sigma_1 = 2.32 \pm 0.30\%$ and $\sigma_2 = 1.85 \pm 0.12\%$. The first term in Eq.3.3 arises from fluctuations in photon statistics and is dominant for energies below about 2.5 GeV, while the constant term takes into account several effects such as fluctuations in shower containment, non-uniformities, calibration uncertainties and electronic noise.

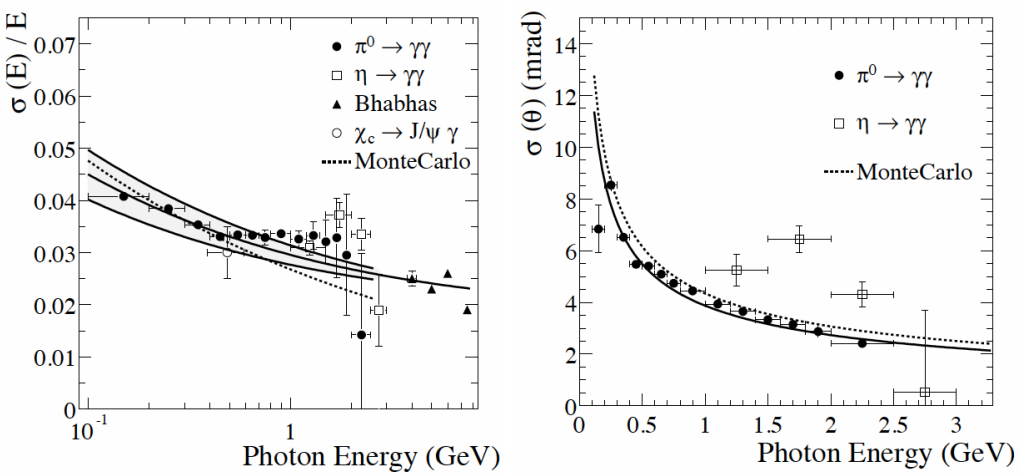

Figure 3.19: Energy (left) and angular (right) resolutions measured using a variety of data. The solid curves represent a fit to the data using Equation 3.3 and 3.4 respectively.

The decays of π^0 and η candidates in which the two photons have approximately equal energy are used to infer angular resolution. It varies between 12 mrad at low energy and 3 mrad at high energy. The data fit the empirical parametrization:

$$\sigma_{\theta,\phi}[\text{mrad}] = \left(\frac{(3.87 \pm 0.07)}{\sqrt{E[\text{GeV}]}} + (0.00 \pm 0.04) \right) \tag{3.4}$$

Fig. 3.19 shows the energy and angular resolution measured as a function of the photon energy [39].

3.3.5 The Instrumented Flux Return

The Instrumented Flux Return (IFR) is the magnetic flux return for the 1.5 T super conducting magnet, instrumented to identify muons and neutral hadrons (primarily K_L and neutrons). The main requirements for IFR were large solid angle coverage, good efficiency and high background rejection for muons down to momenta below 1 GeV/c. For neutral hadrons, high efficiency and good angular resolution are most important.

The IFR is composed by one barrel and two endcaps and uses the steel flux return of the magnet as muon filter and hadron absorber, limiting pion contamination in the muon identification. The IFR has hexagonal shape. The barrel is divided in sextants each 3.75 m in lenght and between 1.88 m and 3.23 m in width, while the forward and backward endcaps are divided in two half End Doors as shown in Fig. 3.20.

The absorbed material in the barrel is segmented in 18 iron plates, increasing in thickness from 2 cm for the inner plates to 10 cm for the outer plates. The gaps between the steel plates are 3.5 cm wide in the inner layers of the barrel and 3.2 cm everywhere else, and are filled with detectors. The variation in the plate thickness with the radius is to allow low momentum muons to be detected, while insuring that hadrons are completely absorbed.

Originally, all the detectors were chosen to be resistive plate chambers (RPCs) and a total of 806 RPC modules were installed [40]; 19 RPC layers in the barrel, 18 layers in the end doors and 2 layers of cylindrical RPCs between the EMC and the magnet to detect particles exiting the EMC.

The hit position in each layer can be reconstructed through a two-coordinate readout: z and ϕ in the barrel section, x and y in the end plates. The hits are matched with the SVT and DCH tracks during recostruction.

The RPC is a type of capacitor, a device in which two conducting plates, with different potentials, are separated by a dielectric material composed of two layers of Bakelite separated by a 2 mm gap filled with gas (a mixture of argon, freon and isobutane). An high electric field of ~ 8 kV/gap is applyed across the dielectric. When charged particles pass through, the gas is ionized and the ions are accelerated by the high electric field. The signal is read out capacitively, on both sides of the gap, by external electrodes made of

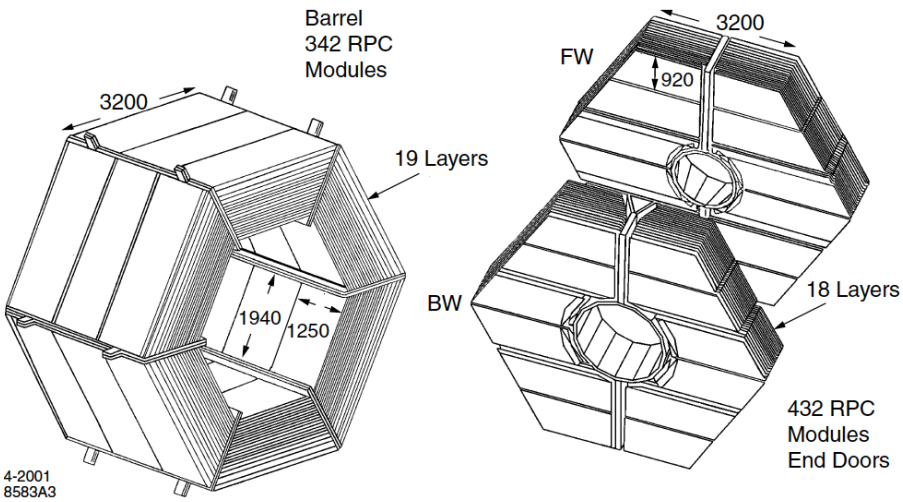

Figure 3.20: Overview of the IFR Barrel sectors and forward and backward end-doors; the shape of the RPC modules and the way they are stratified is shown.

aluminum strips. The strips on the two sides are aligned perpendicularly to each other, to give two coordinates. The RPCs were chosen because they are low cost (important when instrumenting a so large area), they produce large signals and have a fast response, allowing for simple electronics and good time resolution. They can also be constructed to cover irregular shapes so each module was built to match the gaps in the steel with very little dead space.

Unfortunately, it was found that the RPC performance rapidly degraded. Therefore, the muon detection system was upgraded with Limited Streamer Tubes (LST) [41] during the *BABAR* shutdown periods from 2004-2006. The RPCs in the barrel have been replaced by 12 LST detectors and 6 layers of brass to compensate for the loss of absorbing material by removing the RPC detectors. The LSTs are made fron PVC tubes, coated with a layer of graphite paint and filled with a gas mixture (CO2 ISO-butane and Argon), with a silver-plated wire running down the centre. Charged particles passing through the tube ionize atoms of the gas, creating a streamer, inducing signals on the capacitive readout strips surronding the tube. The LSTs have consistently outperformed the RPCs they replaced, achieving muon identification efficiencies of all layers up to the geometrically expected level of 90%. The pion rejection versus muon efficiency is shown in Fig. 3.21 for the LSTs and RPCs. The LSTs efficiency is better than the efficiency that the RPCs had, even during the Run1.

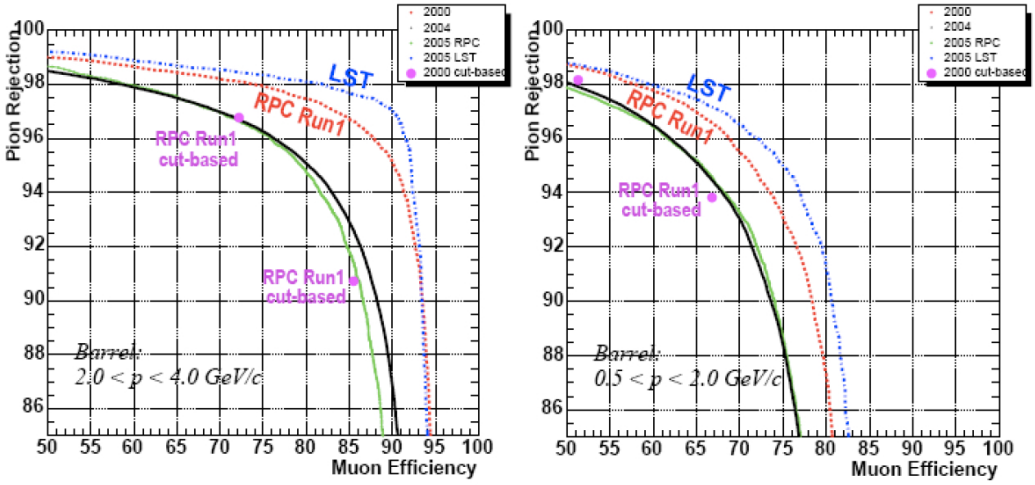

Figure 3.21: Pion rejection versus muon efficiency for two different momentum ranges (left: $2 < p < 4$ GeV/c, right $0.5 < p < 2$ GeV/c). The LST efficiency (blu) is compared with the RPC one for different Runs. We see the deterioration of the RPC performance with time, from 2000 (red) and 2005 (green).

3.3.6 Trigger

The *BABAR* trigger was designed to select a large variety of physics processes while rejecting background events and keeping the total acquired event rate under 120 Hz to satisfy computing limitations of the offline processing farms. The total trigger efficiency was required to be at least 99% for $B\bar{B}$ events, at least 95% for continuum events ($e^+e^- \to q\bar{q}$) and at least 90% for $\tau^+\tau^-$ events. At the design luminosity, beam-induced background rates are ~ 20 Hz for events with at least one track in the drift chamber with $p_T > 120$ MeV/c, and ~ 20 Hz for events with at least one EMC cluster with $E > 100$ MeV.

The trigger reduces the rate of the main physics sources to ~ 90 Hz and also identifies and flags ~ 30 Hz of events used for luminosity determination, and diagnostic and calibration purposes.

The trigger was implemented with a two level hierarchy, a hardware based Level 1 (L1) and a software based trigger called for historical reasons Level 3 (L3) Trigger.

Level 1 Trigger

The L1 Trigger accepts information from the DCH, EMC and IFR, as shown in Fig. 3.22. A signal consisting of one bit from each of the 7104 cells in the DCH is processed by the Drift Chamber Trigger (DCT) to identify tracks.

The Electromagnetic Trigger (EMT) receives input from 280 towers in the EMC, and identifies the energy deposits in the EMC. The IFR is partitioned into ten sections from which eight of the ϕ readout layers provide input for the IFR Trigger (IFT). These sections are the six sextants of the barrel and the four half End Doors. The main tasks of the IFT are to veto cosmic ray events and to identify muons from the interaction $e^+e^- \rightarrow \mu^+\mu^-$ which can be used for measuring luminosity and other detector parameters.

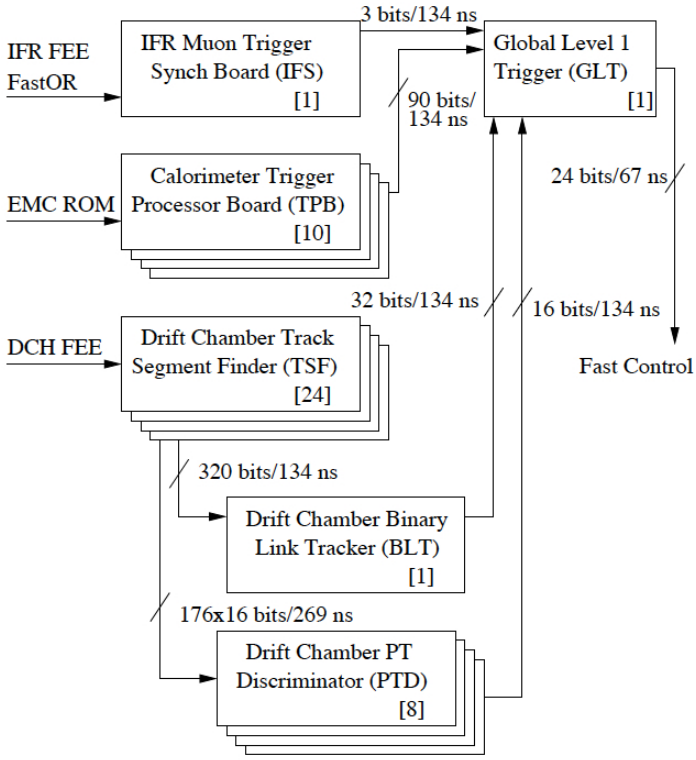

Figure 3.22: Simplified schematic of the L1 trigger system. The number of components are given in the square brackets.

These 3 trigger processors generate a summary of the position and energy of particles, which is transmitted to the Global Level Trigger (GLT), that selects physics events.

The frequency at which the events are accepted by the L1 Trigger is of the order of 1 kHz to 3 kHz, depending on the luminosity and background conditions. This output rate includes $\sim$ 130 Hz from Bhabha and annihilation physics events, 100 Hz of cosmic ray triggers and 20 Hz of random beam crossing triggers. The remaining triggers are mostly due to 'lost' particles interacting with the beam pipe or other components.

Level 3 Trigger

The L3 Trigger, which runs on a farm of Linux machines, has the primary purpose of reducing the selected events from the maximun input rate, to less than 120 Hz with a high efficiency for physics events of interest. The L3 Trigger also supports the online fast monitoring, and selects calibration samples. The L3 Trigger receives input from the L1 Trigger and two subdetectors, the DCH and the EMC. After an initial reconstruction of the charged tracks in the DCH and the neutral clusters in the EMC, the physics content of the event is evaluated. The *Physics Filters* are designed to select $\tau^+\tau^-$, two photons, $B\bar{B}$ and $c\bar{c}$ events with a high efficiency. In addition to the *Physics Filters*, the *Bhabha Filter* isolates the unique topology of electron-positron scattering and rejects Bhabha events. This selection reduces the rate to a level where the entire information from all the subdetectors and the triggers can be written to tape for storage and later processed, for a complete reconstruction of the events.

Tab. 3.2 shows the L3 and and L1+L3 trigger efficiency for some relevant physics processes, derived from simulated events.

L3 Trigger	$\epsilon_{b\bar{b}}$	$\epsilon_{c\bar{c}}$	ϵ_{uds}	$\epsilon_{\tau\tau}$
Combined DCH filters	99.4	97.1	95.4	95.5
Combined EMC filters	93.5	87.4	85.6	46.3
Combined DCH+EMC filters	> 99.9	99.0	97.6	97.3
Combined L1 + L3	> 99.9	98.9	95.8	92.0

Table 3.2: L3 Trigger efficiency (%) for various physics processes, derived from Monte Carlo simulation.

Chapter 4

Data sample and event selection

The τ EDM measurement is performed on the events for which both tau leptons decay via $\tau^{\pm} \to \pi^{\pm}\nu_{\tau}$. This decay is chosen because the two body decay kinematics provides the best constraint for the τ flight direction reconstruction and because the spin reconstruction formula is straightforward. An interesting analysis extension can be done including $\tau^{\pm} \to \rho^{\pm}\nu_{\tau}$ decays.

This chapter describes the procedure used to select $\tau^{+}\tau^{-} \to \pi^{+}\pi^{-}\nu_{\tau}\bar{\nu}_{\tau}$ candidate events from the data set.

The Data and Monte Carlo (MC) simulated samples used to perform the selection and validate *BABAR* event reconstruction procedure, track list composition and particle identification are briefly described.

Starting from the vast *BABAR* data set, numerous more manageable subsets of events, known as *Skimmed*, are produced. Each subset is composed of events which are candidates of a particular physical process. The analysis described here is based on data produced with the *TauQED Skim*. τ-pair data and MC events we are interested in, are selected with the dedicated Tau11 skim, applyed to select $e^{+}e^{-} \to \tau^{+}\tau^{-}$ events in which both tau leptons decay in one prong, i.e. in only one charged particle.

After a brief description of the Skim cuts, the selection of the specific $\tau^{+}\tau^{-} \to \pi^{+}\pi^{-}\nu_{\tau}\bar{\nu}_{\tau}$ channel is described. This selection is performed with a cut-based procedure followed by a Multivariate Analysis with the Boosted Decision Tree (BDT) method [42].

4.1 Data and MC samples

The whole data sample recorded by *BABAR* starting from October 1999 up to September 2007 corresponds to an integrated luminosity of 469 ± 2 fb^{-1}: 425 fb^{-1} of $e^{+}e^{-}$ collisions were collected at the $\Upsilon(4S)$ resonance energy of 10.58

GeV and 44 fb^{-1} at a center of mass energy 40 MeV below. The luminosities integrated in the different periods are detailed in Table 4.1. The analysis will be performed with all the on-peack available data. The total number of analysed τ pairs is of about 3.9×10^8, calculated using the average τ cross section of 0.919 ± 0.003 nb estimated with Kk2f[29].

Run-cycle	On-peak $\mathcal{L}$ [fb^{-1}]	Off-peak $\mathcal{L}$ [fb^{-1}]
Run 1	20.02	2.62
Run 2	61.08	6.92
Run 3	31.85	2.47
Run 4	100.28	10.12
Run 5	133.26	14.49
Run 6	78.37	7.83
Total	424.86	44.44

Table 4.1: Luminosities of all the *BABAR* data sample.

In this thesis work, only the 100 fb^{-1} of Run 4 data are analysed due to time costraints, corresponding to 1.593.363.661 events. The production of all the other selected events is almost ready.

For the analysis, MC simulated samples for signal and background events have been also produced to understand the background, to estimate the selection efficiency and to evaluate the τ lepton EDM sensitivity. The MC samples are produced by combining simulated events according to their relative cross section at *BABAR*, given in reference [43] and reported in Table.4.2.

$e^+e^- \to$	Cross section σ (nb)
$\tau^+\tau^-$	0.9
$\mu^+\mu^-$	1.1
e^+e^-	25
$u\bar{u}, d\bar{d}, s\bar{s}$	2.1
$c\bar{c}$	1.3
B^+B^-	0.55
$B^0\bar{B}^0$	0.55

Table 4.2: Production cross section for various processes at $\sqrt{s} = M(\Upsilon(4S))$. The $e^+e^+ \to e^+e^-$ cross section is the effective cross section for the experimental angular acceptance $15° < \theta < 165°$. The total bhabha cross section of the events with one or both $e^\pm$ inside the calorimeter acceptance is of ~ 53 nb [44].

MC samples of τ lepton events are produced using the Kk2f generator [29] and Tauola decay library [30]. B meson decays are simulated with EvtGen

generator [45], and $q\bar{q}$ events, where $q = u, d, s, c$, with JETSET generator [46]. Two different samples are generated for $q\bar{q}$ events, one for $c\bar{c}$ and one for $u\bar{u}$, $d\bar{d}$ and $s\bar{s}$, generally referred to as uds sample. Radiative corrections are simulated using PHOTOS [47]. Bhabha events are generated only within the polar angle $15° < \theta < 165°$ in the lab system. Simulated events are then processed using the detailed model of *BABAR* detector created using GEANT4 simulation package [48]. Therefore, for MC samples, all the reconstructed variables are available exactly as for real data, together with the information about the original processes, decays and kinematical quantities (so called MC-truth). MC samples are produced proportionally to the luminosity integrated during each Run-cycle. The *BABAR* experiment has a database that keeps track of all the changes in conditions and calibrations occurred during the data taking, therefore, for each Run-cycle a different MC is produced, to simulate events in the conditions as close as possible to the real status of the detector.

The size of the MC samples associated to the Run4 used in this thesis are listed in Table 4.3. Due to the large cross section of bhabha process it would not be feasible to produce a simulated sample corresponding to the integrated luminosity of the data. Only one MC sample for all the Run-cycles is eventually used for the bhabha, confirming that bhabha events result in a negligible contamination to the final sample of signal events.

MC collection	Generated events	$\mathcal{L}$ [fb^{-1}]
$e^+e^- \to \tau^+\tau^-$	180077000	200
$e^+e^- \to \mu^+\mu^-$	121574000	110.5
$e^+e^- \to u\bar{u}, d\bar{d}, s\bar{s}$	416151000	198
$e^+e^- \to c\bar{c}$	267308000	205
$e^+e^- \to B^+B^-$	169801000	309
$e^+e^- \to B^0\bar{B}^0$	166784000	303
$e^+e^- \to$ bhabha ($15° < \theta < 165°$)	441630000	17.66

Table 4.3: Summary of the MC samples used in this thesis. The equivalent luminosities of the MC samples are calculated using the cross sections given in Table 4.2.

For the analysis, each MC sample is rescaled according to the corresponding data/MC luminosity ratio. A detailed comparison of data and MC distributions has been performed during each selection stage to ensure that MC sample properly reproduces real data.

4.2 Preselection

The purpose of the preselction is to remove most of the background events saving most of the signal events, increasing the purity and reducing at the same time the sample to a manageable size. The MC and data samples are both processed using a standard Skim.

The Skim is a collection of recontructed events obtained applying physics-motivated loose selection cuts to the sample of all reconstructed events. Numerous selections, defined by the *TauQED Physics Group* are used to produce collections of events that are of particular interest for τ physics studies. The τ-pair topologies accounted for by the TauQED Skim selection include 1-1, 1-3, 3-3, and 1-5 configurations. The notation 1-3, for example, indicates that one τ decays into a single prong final state, appearing as a single charged track in the detector and that the other τ decays into a three prong final state, producing three charged tracks in the detector.

The Skim 1-1 preselection must be used for our analysis of the τ-pair events decaying via $\tau^{\pm} \rightarrow \pi^{\pm}\nu_{\tau}$. The selection criteria of this Skim are summarized in the following.

4.2.1 Tau QED Skim 1-1

The selection criteria used in the TauQED Skim 1-1 were determined by Swagato Banerjee et al. [49, 50]. The purpose of this Skim was to reduce $q\bar{q}$, $\mu^+\mu^-$ and Bhabha events while keeping a large percentage of $\tau^+\tau^-$ events.

The selection begins by choosing events having a shape consistent with the kinematic constraints from $e^+e^- \rightarrow \tau^+\tau^-$ events with both taus decaying into one charged particle. The events are therefore required to have two well reconstructed tracks, which do not originate from conversions in the material of the detectors, and have a net charge of zero. The selection takes also advantage of the separation of the τ^+ and τ^-, the small number of particles in $\tau^+\tau^-$ events compared to $q\bar{q}$ events, and the lower measurable invariant mass of the event due to the undetected neutrinos.

In the CM frame, the τ^+ and τ^- decay back to back and, since the tau leptons are energetic ($P_T \simeq 3$ GeV), their daughters are boosted and decay in two separate hemispheres forming a jet-like event structure. The hemispheres are defined by the plane perpendicular to the thrust axis of the event, where the thrust axis is defined by the unit vector that maximizes the projected momentum from all the charged and neutral reconstructed particle tracks in the event. Thrust magnitude gives a measure of how an event is jet-like: magnitude 1 means that all tracks are aligned along a preferred direction, 0.5 means that there is no preferred direction, i.e. the event has a spherical

symmetry. Most of the $\tau^+\tau^-$ events are above 0.9 as can be seen in Fig. 4.1 and Fig. 4.2.

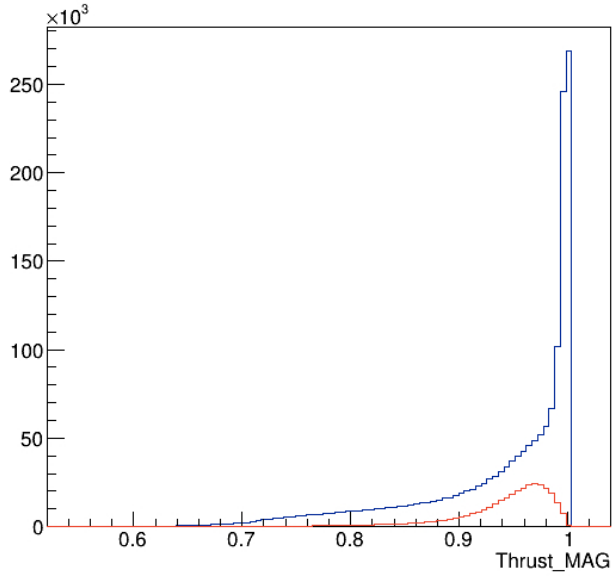

Figure 4.1: Thrust magnitude distribution for 1 fb^{-1} of skimmed Data (blue) and for 1 fb^{-1} of $\tau^+\tau^-$ skimmed MC events (red).

The selection criteria for the TauQED Skim 1-1 are defined as follows:

- L3 Trigger;
- The *BABAR* event tag BGFTAG must have one of the following bit on:

  (BGFMultiHadron || BGFNeutralHadron || BGFTau || BGFMuMu || BGFTwoProng),

  where each bit indicates a specific event topology;
- Number of tracks in ChargedTracks list ≤ 10 (how a track list is formed is illustrated in 4.3 section);
- Number of neutrals (with energy > 50 MeV) in each hemisphere ≤ 6, to keep up to $3\pi^0$ decays from each τ;
- Total number of primary tracks $= 2$ with 1 track in each hemisphere. Primary tracks requirements are similar to the GoodTracksVeryLoose conditions that will be illustrated in 4.3.1 subsection: minimum transverse momentum $0 < P_T < 10$ GeV, minimum number of DCH hits ≥ 0, maximum distance of closest approach (DOCA) in z-plane < 10 cm and in xy-plane < 0.2 cm;

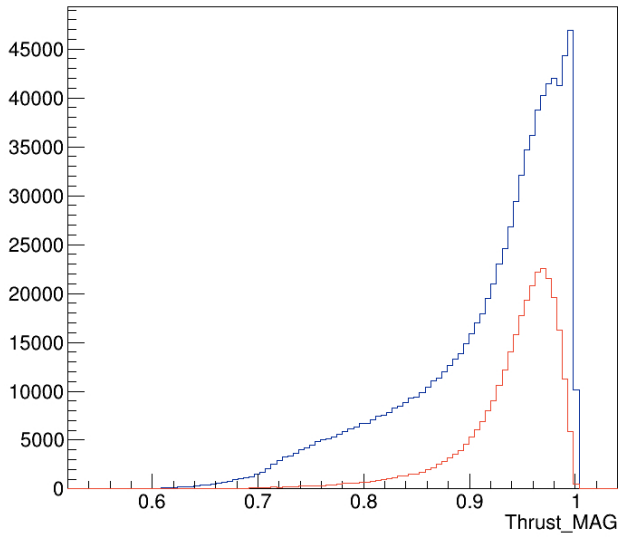

Figure 4.2: Thrust magnitude distribution for 1 fb^{-1} of skimmed Data (blue) and for 1 fb^{-1} of $\tau^+\tau^-$ skimmed MC events (red) with the additional condition that BGFTau bit is 1 and BGFMuMu bit is 0.

- $Cos\theta$ of the 2 most energetic tracks are required to lie within the calorimeter acceptance ($-0.76 < cos\theta < 0.96$);
- A constraint on the event missing energy is also required: (MissingMass/$\sqrt{s} < 0.2$ || $-log(2\times\text{MissingP}_T/\sqrt{s}) < 0.4$).

Topology	TauQED Skim 1-1 Efficiency
Data	17%
$\tau^+\tau^-$	47%
$\mu^+\mu^-$	64%
e^+e^-	1%
$u\bar{u}, d\bar{d}, s\bar{s}$	7.3%
$c\bar{c}$	4.7%
B^+B^-	0.8%
$B^0\bar{B}^0$	0.8%

Table 4.4: Skim 1-1 efficiencies for the Data and the different MC collections.

We shown in Table 4.4 the Skim 1-1 efficiencies obtained by the ratios between the number of events selected and dumped in the Data and MC ntuples and the total number of events listed in Table 4.3. With the prong 1-1 topology requirement, a lot of $\mu^+\mu^-$ events are also selected. To reduce

this large contamination we tightened the BGFTAG condition, selecting only the events for which the BGFMuMu bit is 0 and the BGFTau bit is 1. The BGFTau filter is optimized to be efficient in selecting τ-pairs whilst reducing contamination, in particular from μ-pairs events, with an additional condition on the missing energy of the event. We remind that $\tau^+\tau^-$ events are characterized by neutrinos in the final state. BGFTau requires a missing momentum vector $P_{Miss} > 0.5$ GeV with $-0.91 \leq cos\theta_{P_{miss}} \leq 0.89$ (within the angular acceptance of the EMC). Efficiencies on Data and MC obtained with the additional condition on BGFTAG are shown in Table 4.5

Efficiency for (BGFTau = 1 & BGFMuMu = 0)	
Data	9.5%
$\tau^+\tau^-$	43.7%
$\mu^+\mu^-$	3.6%
e^+e^-	0.8%
$u\bar{u}, d\bar{d}, s\bar{s}$	4.1%
$c\bar{c}$	2.1%
B^+B^-	0.3%
$B^0\bar{B}^0$	0.3%

Table 4.5: Resulting efficiencies for the data and MC collections with the condition on BGFTAG.

The important effect on the Data sample after applying the additional condition on BGFTAG can be also appreciated comparing the thrust magnitude distribution of Fig 4.1 and Fig. 4.2 where the new condition eliminates most of the muon contamination with very high thrust magnitude. To increase the sample purity we also require thrust magnitude > 0.9.

4.3 Event reconstruction

4.3.1 Charged particle reconstruction

Charged particle tracks are reconstructed by processing the information from both tracking systems, the SVT and the DCH. The track finding and the fitting procedures use the *Kalman filter* algorithm [51], that takes into account the detailed distribution of material in the detectors and the full magnetic field map. After a first processing producing a rough list of reconstructed *track objects*, a refinement procedure is applied by adding hits not associated in the first processing or removing hits with low probability.

With this procedure, a track-based candidate list which will be used in the analysis is created. This is the *Charged Tracks list*, the basic list containing all tracks that are found by the track reconstruction algorithm. The mass hypothesis used is always the one of a charged pion.

Further requirements are then applied to obtain lists of charged tracks satisfying tighter conditions. The selection involves the transverse momentum of the particle P_T and the distance of closest approach (DOCA) in the z direction and on the xy plane. The selection criteria for the reconstructed charged particle lists are illustrated in Table 4.6.

Charged track list	Description
chargedTracks	Charged particle tracks in SVT and/or DCH with pion mass hypothesis assigned.
goodTracksVeryLoose	*chargedTracks* with: $P < 10$ GeV/c; $\mathrm{DOCA}_{xy} < 1.5$ cm; -10 cm $\leq \mathrm{DOCA}_z \leq 10$ cm Number of DCH hits ≥ 0.
goodTracksLoose	*goodTracksVeryLoose* with: $P_T > 0.1$ GeV/c; Number of DCH hits ≥ 10.
goodTracksTight	*goodTracksLoose* with: $\mathrm{DOCA}_{xy} < 1$ cm; $\mathrm{DOCA}_z \leq 3$ cm Number of DCH hits ≥ 20.

Table 4.6: Lists of reconstructed charged particle tracks stored in the BABAR event database. DOCA is the distance of closest approach of a track to the interaction point.

4.3.2 Particle identification criteria

The charged particle tracks pass through PID procedures and then are organized in particle candidate lists. The lists differ by the selection method used, the selection condition applied, and type of particle. There are many lists for each type of particle candidate, $e, \mu, \pi, K, p, K^0_s, \pi^0$ and a candidate can be present in more than one list.

The *BABAR* particle identification is performed by using many discriminant variables available from all sub-detectors. A good identification is feasi-

ble applying simple requirements to each of those variables, but better results were obtained using advanced techniques that combine information from different quantities to have a higher discriminant power. Techniques such as likelihood ratio, neutral network or *bagged decision tree* [52] are currently used.

- Cut-based methods (Micro) impose to a charged particle a set of selection criteria based on simple cuts. If the candidate passes these criteria, it is assumed to be of the tested particle type.
- Likelihood selectors (LH) use PID variables to calculate a likelihood for a track to be originated from a given particle type. The likelihood is based on measured quantities from different subdetectors. They are compared to the expectation values for the different particle hypotheses. A specific selection algorithm requires the likelihood to be above a certain value to assign the particle type to the track. Alternatively, it requests that the likelihood for a given hypothesis be larger than the ones for the other particle types.
- Neural Network selectors (NN) use a set of input variables from the *BABAR* subdetectors. The neutral network algorithm are trained to identify the wanted particle type and produce one single output variable. If the output for any particle hypothesis is larger than a preset value, this hypothesis is assigned to the charged particle.
- KM selectors [53] are based on Bagged decision tree (BDT) and Error Correcting output code (ECOC) Multiclass classifier technique [54]. The performance of these two selectors meets or exceeds that of previous neutral network and likelihood techniques.

For each method there are different selector conditions, depending if looser selection (higher efficiency but also higher mis-identification rate) or tighter selection (lower efficiency but also lower mis-identification rate) are requested. Each track satisfying or not a specific selector is flagged with a corresponding binary information. A track satisfying a tighter selector also satisfies the looser ones from the same method (i.e. selectors are nested). For each particle category (electrons, muons, pions and kaons) several methods are implemented.

Neutrals particle classification is performed with a similar procedure.

Pion identification

For this analysis we use two different selector methods, both of them implemented in the most recent release of the *BABAR* software.

Both charged tracks of the signal events are required to be pions with the tighter pion condition. Furthermore, to minimize the muon misidentification, we also require that tracks do not belong to the looser muon condition list.

For the pions identification we adopt an ECOC-based classifier. Characteristics of this method, variables adopted for the selection and selector performance, are illustrated in reference [55]. 31 variables are used for the binary classifiers including: momentum, charge, polar and azimuthal angle of the track, DIRC, SVT and DCH likelihoods for the 5 particles hypotheses p, π, e, μ, K, SVT and DCH hits and layers information and EMC cluster propertys.

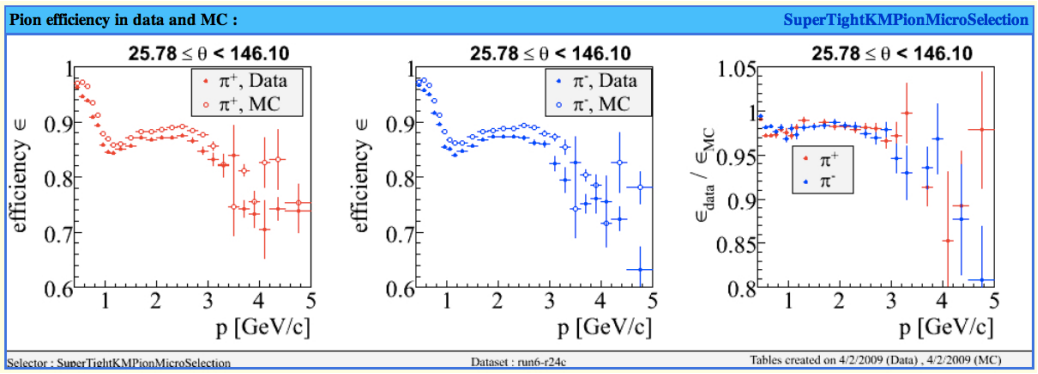

Figure 4.3: Pion efficiency in Data and MC for the SuperTight condition of the ECOC-based classifier list.

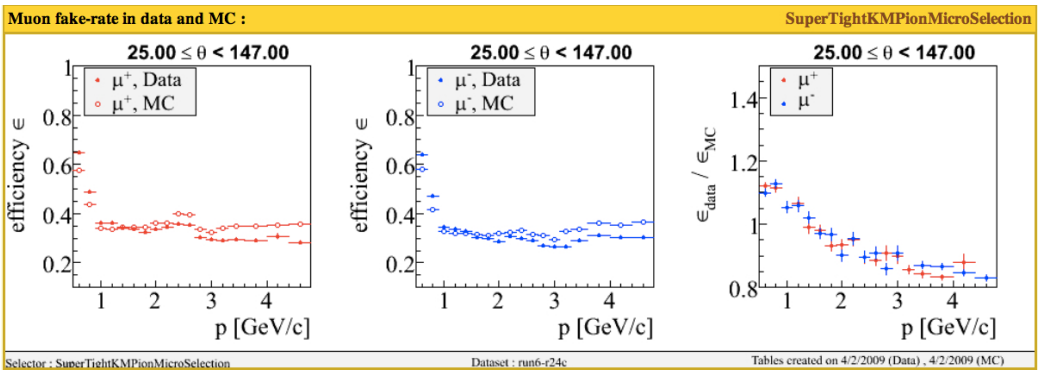

Figure 4.4: Muon contamination in Data and MC for the SuperTight condition of the ECOC-based classifier list.

All the information illustrating the characteristics of each list can be found in the *BABAR* documentation archive. We report here the plots of interest for our selection (from Fig 4.3 to Fig 4.11).

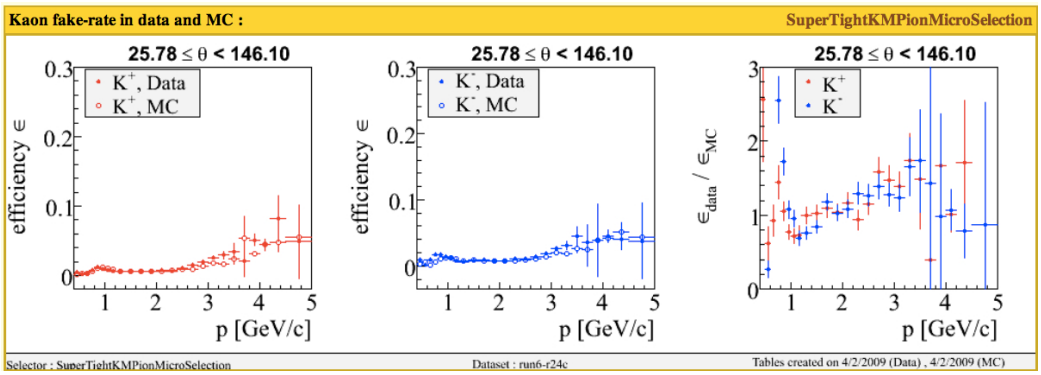

Figure 4.5: Kaon contamination in Data and MC for the SuperTight condition of the ECOC-based classifier list.

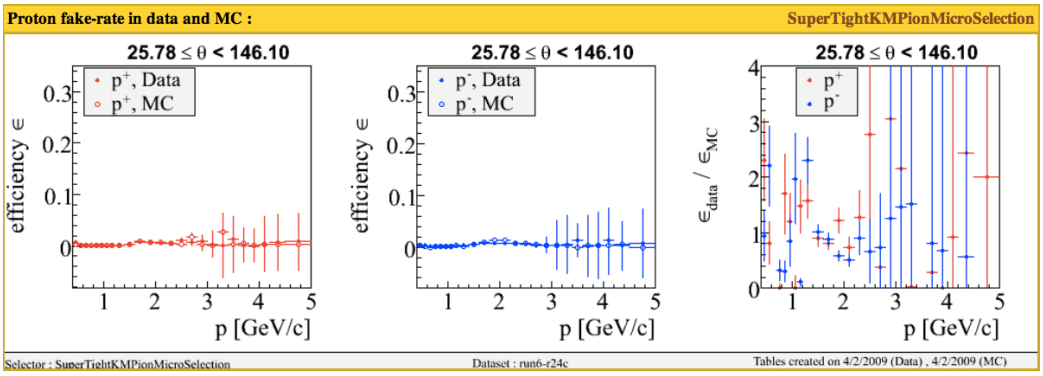

Figure 4.6: Proton contamination in Data and MC for the SuperTight condition of the ECOC-based classifier list.

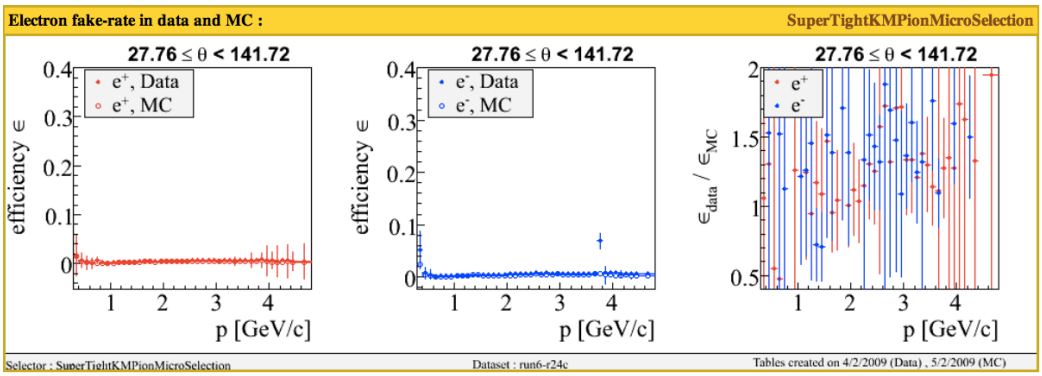

Figure 4.7: Electron contamination in Data and MC for the SuperTight condition of the ECOC-based classifier list.

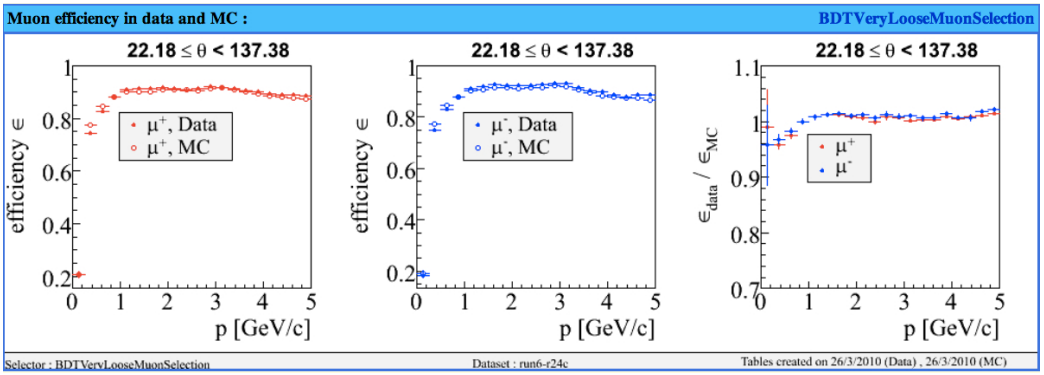

Figure 4.8: Muon efficiency in Data and MC for the VeryLoose condition of the BDT muon selection list.

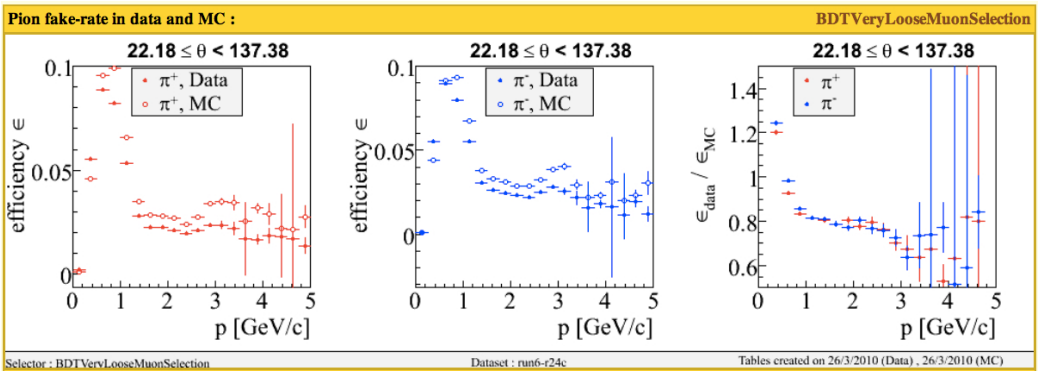

Figure 4.9: Pion contamination in Data and MC for the VeryLoose condition of the BDT muon selection list.

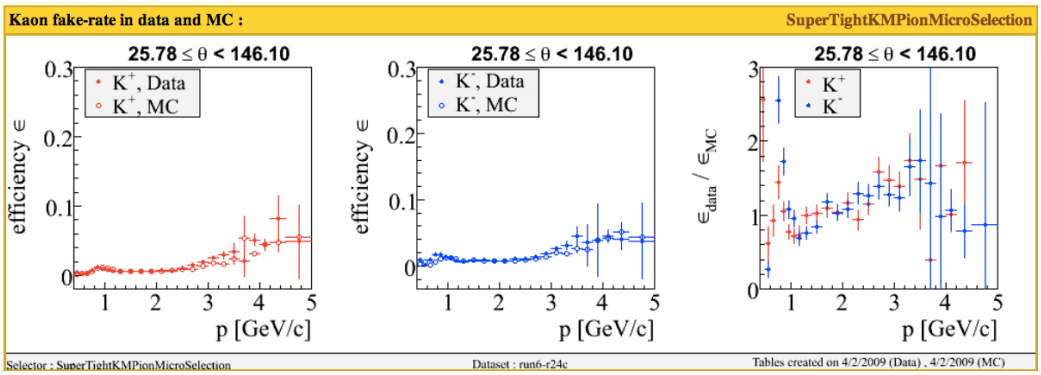

Figure 4.10: Kaon contamination in Data and MC for the VeryLoose condition of the BDT muon selection list.

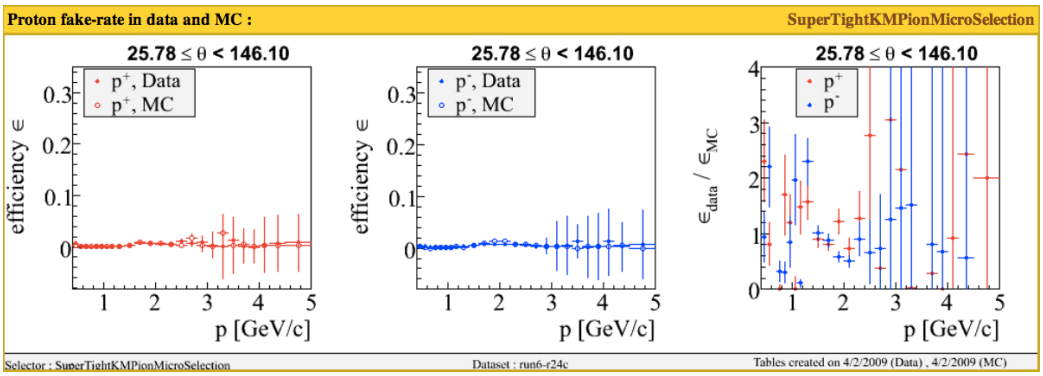

Figure 4.11: Proton contamination in Data and MC for the VeryLoose condition of the BDT muon selection list.

The efficiency in selecting pions for Data and MC with the SuperTight condition of the ECOC list is shown in Fig. 4.3. Muon, Kaon, proton and electron fake-rate are shown in Figures 4.4, 4.5, 4.6 and 4.7, respectively.

The Muon contamination rate is of the order of 40%. As anticipated, a better signal purity can be reached by setting the additional requirement that the two tracks must not belong to the VeryLoose condition of the BDT classifier Muon list.

BDT Muon Selector characteristics, variables adopted for the selection and selector performance are extensively treated in reference [56]. For the track classification 30 variables are used. Momentum, charge, polar angle of the track and, in addition to the EMC, DCH and DIRC information, also hits, number of strips and geometrical hits characteristics of the IFR are used. The efficiency for the VeryLoose condition of this list in selecting muons is shown in Fig. 4.8. Pion, Kaon and proton fake-rate are shown in Figures 4.9, 4.10 and 4.11, respectively.

As we can see, requiring the two charged tracks not to belong to the VeryLooseMuon list, almoust 90% of the muon contamination is removed at a cost of a few percent reduction in the pion efficiency.

4.3.3 Additional requirements

In $(85.35 \pm 0.07)\%$ [57] of cases τ leptons decay in one prong. The main τ decay branching ratios are listed in Table 4.7. The signal represented by both tau leptons decaying via $\tau^{\pm} \to \pi^{\pm}\nu_{\tau}$ constitutes $\simeq 1.2\%$ of the total $\tau^{+}\tau^{-}$ sample.

In addition to the requirement on the two charged tracks, we make a cut on the event missing energy: 1.0 GeV $< E_{miss} < 9.0$ GeV. With this condition

Tau decay mode	Branching ratio
$\tau^- \to \mu^- \bar{\nu}_\mu \nu_\tau$	$(17.41 \pm 0.04)\%$
$\tau^- \to e^- \bar{\nu}_e \nu_\tau$	$(17.83 \pm 0.04)\%$
$\tau^- \to \pi^- \nu_\tau$	$(10.83 \pm 0.06)\%$
$\tau^- \to \rho^- (\pi^- \pi^0) \nu_\tau$	$(25.52 \pm 0.09)\%$
$\tau^- \to a_1^- (\pi^- \pi^0 \pi^0) \nu_\tau$	$(10.87 \pm 0.11)\%$
3 prongs	$(14.57 \pm 0.07)\%$

Table 4.7: Branching ratios of the main τ decays [57].

we reduce the $e^+e^- \to \mu^+\mu^-$ background characterized by a missing energy distribution sharp and centered in zero and the background in which one or both tau leptons decay leptonically via $\tau^\pm \to l^\pm \nu_\tau \nu_l$: in these channels there are more than two neutrinos in the final state, therefore the missing energy is higher than in the signal events.

At this stage, the filters applied do not select the decay $\tau^\pm \to \pi^\pm \nu$ with respect to $\tau^\pm \to \rho^\pm \nu$ where the charged track is equally represented by a pion. To discriminate from the $\rho^\pm$ decays background a preliminary condition is imposed requiring that there are no reconstructed π^0 in the Loose π^0 list.

The purity of the selected sample and the signal efficiency for the skimmed $\tau^+\tau^-$ MC sample after each selection requirement are shown in Table 4.8.

	Signal purity	Signal efficiency
Thrust magnitude > 0.9	1.2 %	65 %
Both charged tracks: SuperTightPion NOT VeryLooseMuon	3.4 %	38 %
$1.0 < E_{miss} < 9.0$ GeV	3.2 %	35 %
Number of reconstructed π^0 loose $= 0$	20 %	31 %
Energy of each neutral cluster < 600 MeV	29 %	30 %

Table 4.8: Sample purity and signal efficiency with respect to the skimmed $\tau^+\tau^-$ MC sample, after each cut.

After the requirements on the π^0, the $\tau^+\tau^-$ sample has a purity of 20%. In spite of the requirement of no $\pi^0 loose$ in the event, $\rho^\pm$ contamination is still high: 42% of selected events have at least one of the two τ leptons decaying via $\tau^\pm \to \rho^\pm \nu_\tau$. To increase the sample purity reducing $\rho^\pm$ background, neutral clusters must be analysed. Boths $\rho^\pm$ and $\pi^\pm$ events can be characterized by reconstructed neutral clusters. A threshold on energy > 20 MeV

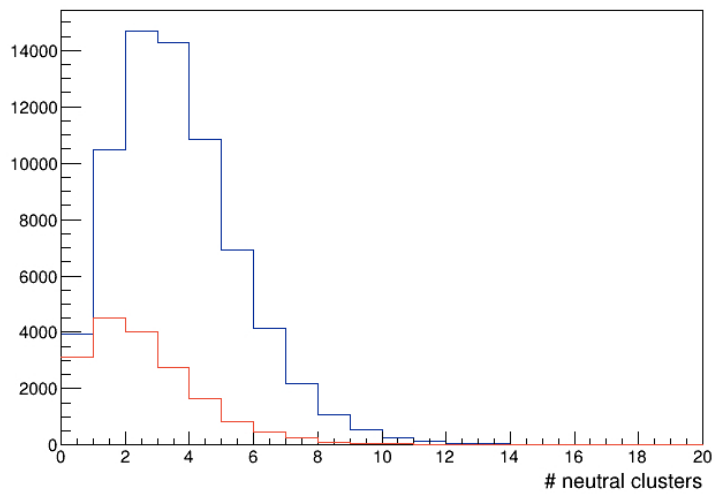

Figure 4.12: Number of neutral clusters for background events (blue) and signal events (red).

is used to define a cluster. In the first case, the photons of the $\pi^0 \to \gamma\gamma$ can fail the π^0 algorithm reconstruction requirement for the π^0 list resulting in a single neutral track. In the second case, the calorimeter electronic noise can produce some fake neutral clusters. Physical and fake neutrals should be discriminated.

In Fig.4.12 the number of neutral custers for signal and background events is shown. In Fig. 4.13 the energies of neutral clusters for signal and background events are shown. To select the signal we add the requirement that all the neutral cluster energies must be less than 600 MeV. Also the effect of this cut is illustrated in Table 4.8. The final $\tau^+\tau^-$ sample has a purity of 29%.

At this stage a Multivariate Analysis is introduced to improve the selection. Only the cases with 0, 1, 2, and 3 neutral clusters have been treated. In Table 4.9 we show the composition of these four selected sample, obtained with the MC normalized to the data luminosity of 100 fb^1. The purities of the total samples, considering also the non $\tau^+\tau^-$ contribution, are of 40%, 35%, 30.4% and 18% respectively.

4.4 ROOT's Boosted Decision Tree (BDT)

The last step of the selection is performed with the Root's MultiVariate Analysis (MVA) classifiers, in particular the Boosted Decision Tree (BDT) method, illustrated in Appendix 3, is employed.

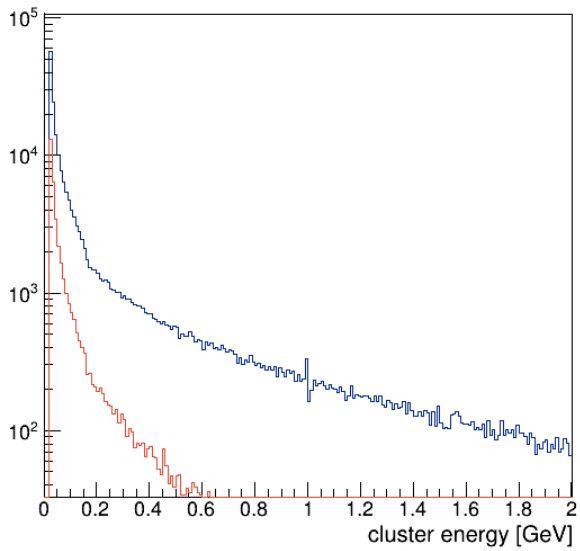

Figure 4.13: Neutral cluster energies for background events (blue) and signal events (red) in log scale.

Event type	0 neutral cluster	1 neutral cluster	2 neutral clusters	3 neutral clusters
$\tau^+\tau^- \to (\pi\pi)$	19762	32659	33103	27212
$\tau^+\tau^- \to (\pi\rho)$	2626	14169	23772	45609
$\tau^+\tau^- \to (\pi\mu)$	12622	17944	15749	11705
$\tau^+\tau^- \to (\pi e)$	963	1827	1943	1939
$\tau^+\tau^- \to (\rho\rho)$	227	1058	3002	12716
$\tau^+\tau^- \to (\mu\mu)$	1309	1456	1003	625
$\tau^+\tau^- \to (ee)$	7	12	14	9
$\tau^+\tau^- \to (\rho\mu)$	608	3684	5787	9685
$\tau^+\tau^- \to (\rho e)$	68	310	520	1225
$\tau^+\tau^- \to (\mu e)$	152	227	182	180
$\tau^+\tau^- \to$ others	7835	16481	21058	35522
$\mu^+\mu^-$	1280	1595	1180	862
$c\bar{c}$	-	3	6	16
$u\bar{u}, d\bar{d}, s\bar{s}$	75	211	336	1114
B^+B^-, B^0B^0	-	-	-	-
bhabha	1377	1309	1092	1051

Table 4.9: Sample composition for events with 0, 1, 2, 3 neutral clusters. The number of events obtained with the MC has been normalized to data luminosity. The two particles under parenthesis in the left column indicate the identity of the two τ decays.

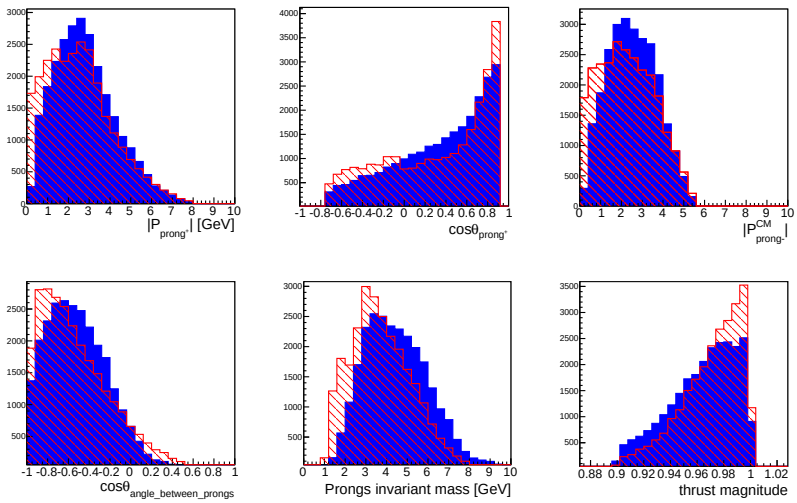

Figure 4.14: BDT0 input variables. Signal (blue) and background (red) distributions for: module of the positive prong momentum (top left), $cos\theta$ of the positive prong track (top middle), module of the negative prong in the center of mass frame system (top right), cosine of the angle between the two prong tracks (bottom left), invariant mass of the two prongs (bottom middle), thrust magnitude (bottom right).

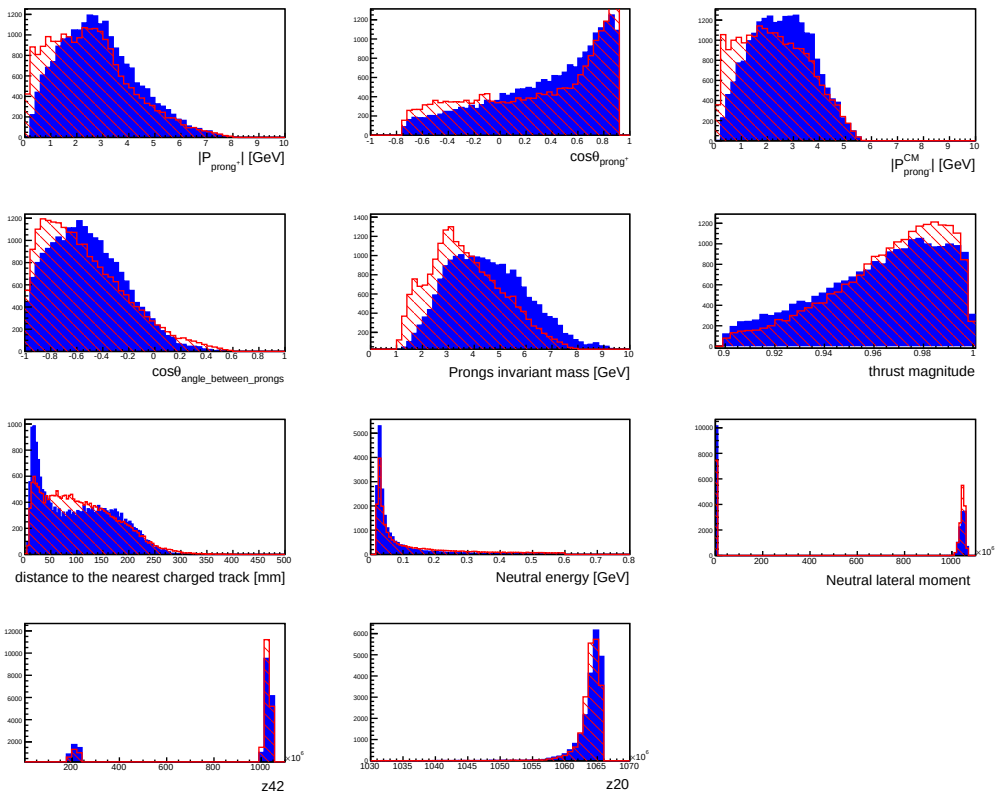

Figure 4.15: BDT1 input variables. Signal (blue) and background (red) distributions for: module of the positive prong momentum (first line left), $cos\theta$ of the positive prong track (first line middle), module of the negative prong in the center of mass frame system (first line right), cosine of the angle between the two prong tracks (second line left), invariant mass of the two prongs (second line middle), thrust magnitude (second line right), distance of neutral to the nearest charged track (third line left), neutral cluster energy (third line middle), neutral lateral moment (third line right), absolute value of the complex Zernike(4,2) moment (fourth line left), absolute value of the complex Zernike(2,0) moment (fourth line middle).

The multivariate software package integrated within Root, called TMVA (Toolkit for Multivariate Data Analysis), has been developed to optimize event selection. TMVA is a toolkit which contains a large variety of multivariate classification algorithms, cut optimization algorithms, likelihood estimators, linear and non-linear neural networks and boosted decision trees. TMVA manages simultaneously the training, testing and performance evaluation of all these classifiers. The analysis is performed in two independent steps, first the training phase, where the multivariate classifiers are trained, tested and evaluated, and then an application phase where selected classifiers are applied to the concrete classification problem they have been trained for.

For this analysis we have built up four different BDTs, one for the case with no neutrals in the event, one for the case with only one neutral, one for the case with two neutrals and one for the case with three neutrals. In the following we refer to these BDTs with the notation BDT0, BDT1, BDT2, BDT3 respectively.

BDT0 has been implemented with 6 variables illustrated in Fig4.14: the module of the positive prong momentum, the $cos\theta$ of the positive prong track, the module of the negative prong in the center of mass frame system, the cosine of the angle between the two prong tracks, the invariant mass of the two prongs and the thrust magnitude.

BDT1 has been implemented with 11 variables illustrated in Fig4.15, the same 6 variables of the BDT0 plus the 5 variables, relatives to the neutral clusters: distance to the nearest charged track, energy, lateral moment, absolute value of the complex Zernike(4,2) and absolute value of the complex Zernike(2,0), these last three variables are related to the cluster geometry and to the Zernike polynomials used to describe the cluster [58].

BDT2 and BDT3 have been implemented with 14 and 18 variables, the same 6 variables of the BDT0 plus variables relatives to the neutral clusters. The neutrals are ordered with decreasing energy. For each neutral the distance to the nearest charged track, the energy, the lateral moment and the absolute value of the complex Zernike(4,2) have been used. In Fig 4.16 we show the BDT2 variables.

For an efficient BDT method application the variables should not be strongly correlated. In Figures 4.17, 4.18, 4.19, and 4.20 we show the linear correlation coefficients for signal (a) and background (b) for BDT0, BDT1, BDT2 and BDT3 respectively.

In Figures 4.21, 4.22, 4.23 and 4.24 the BDT output distributions for signal and background for BDT0, BDT1, BDT2 and BDT3 respectively are presented. Test samples (histograms) and training samples (points) are superimposed, showing good agreement. For each data event, the BDT output can be calculated by means of the weight files produced by the Toolkit, start-

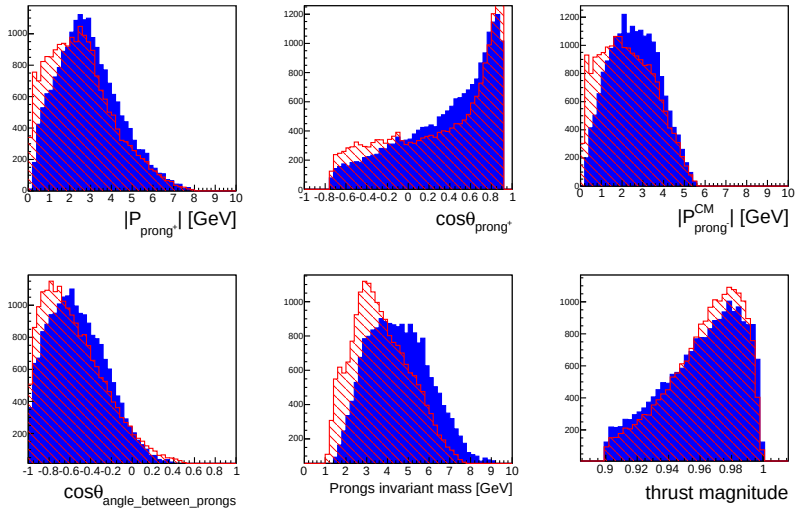

(a) Signal (blue) and background (red) distributions for: module of the positive prong momentum (top left), *cosθ* of the positive prong track (top middle), module of the negative prong in the center of mass frame system (top right), cosine of the angle between the two prong tracks (bottom left), invariant mass of the two prongs (bottom middle), thrust magnitude (bottom right).

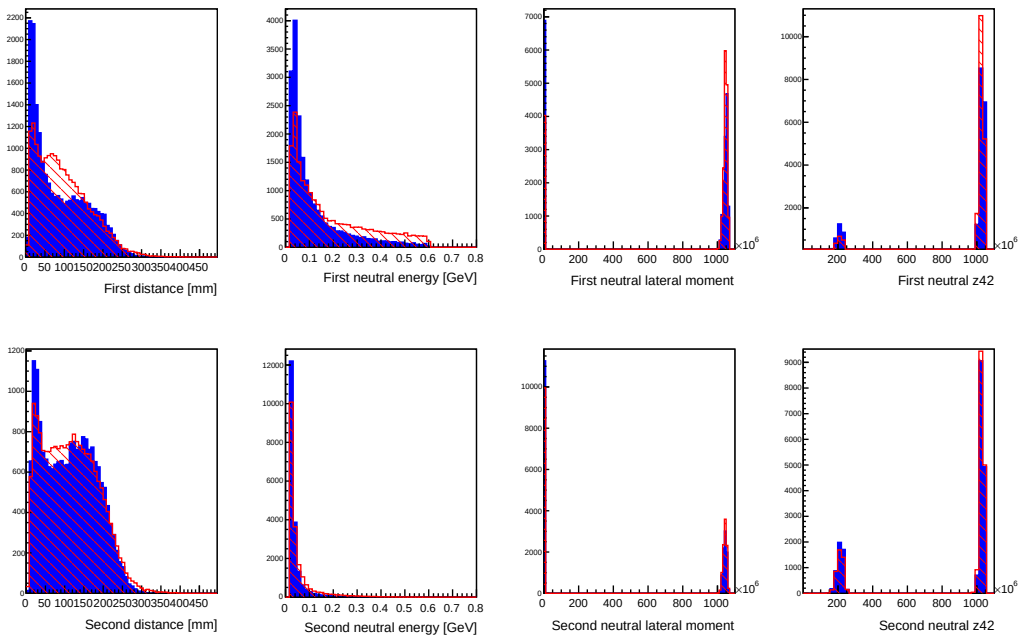

(b) Signal (blue) and background (red) distributions for, from the left: distance of neutral to the nearest charged track, neutral cluster energy, neutral lateral moment and absolute value of the complex Zernike(4,2) moment, for the first (top) and the second (bottom) neutral cluster.

Figure 4.16: BDT2 input variables.

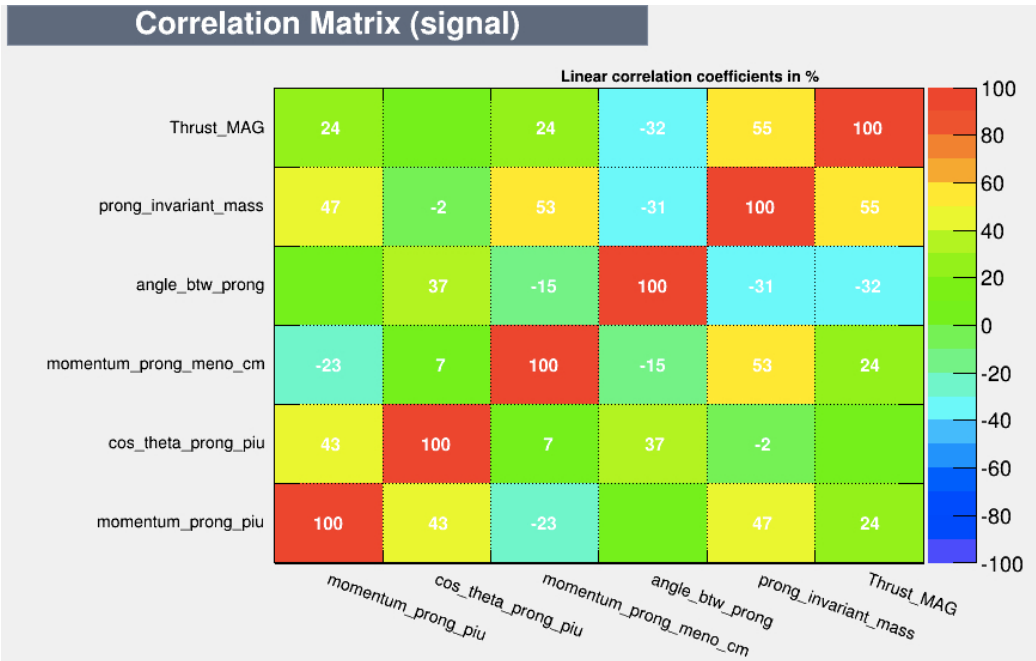

(a)

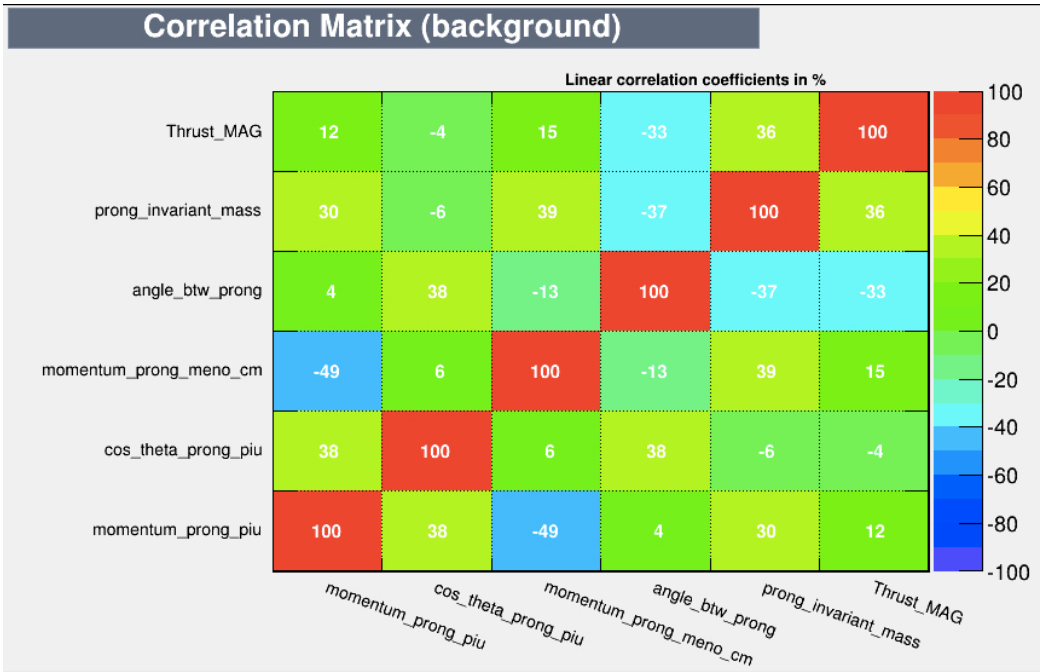

(b)

Figure 4.17: Linear correlation coefficients between the BDT0 variables for the signal (a) and background (b) sample.

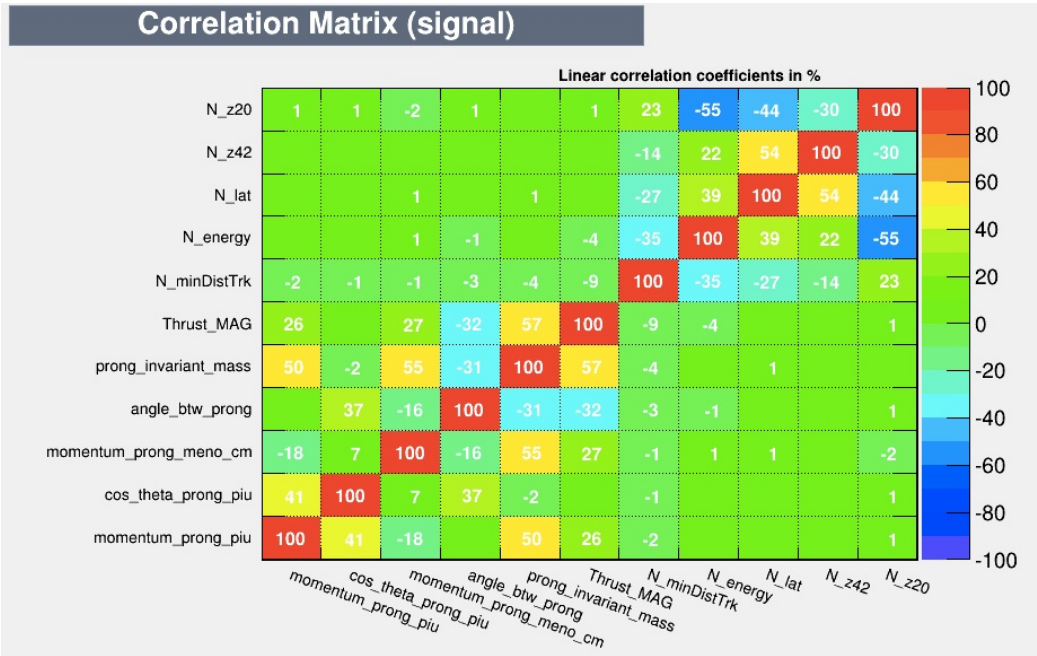

(a)

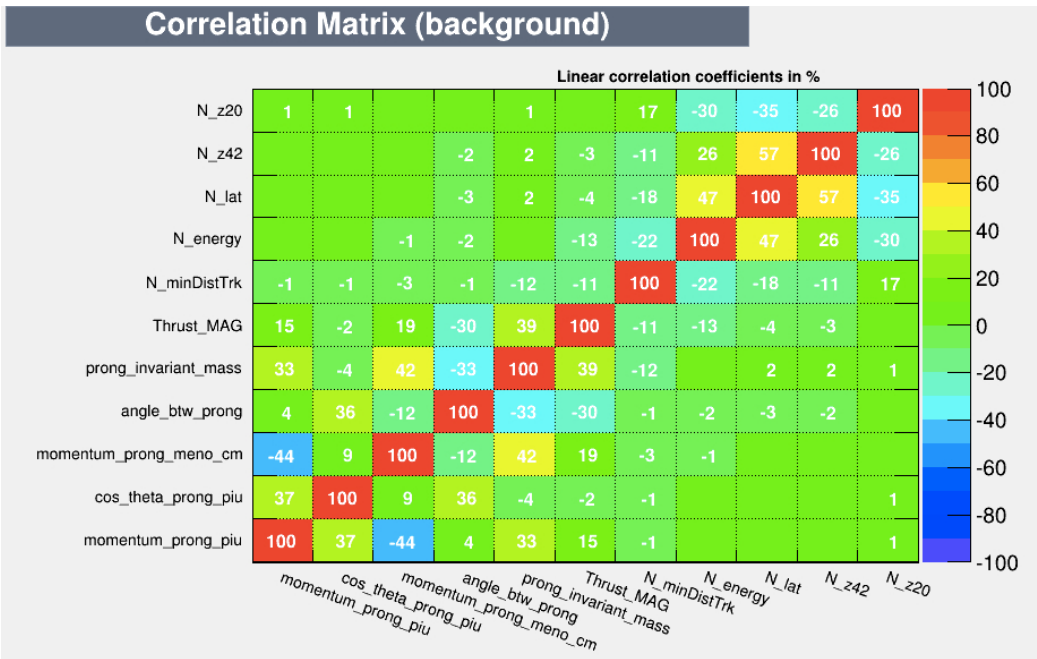

(b)

Figure 4.18: Linear correlation coefficients between the BDT1 variables for the signal (a) and background (b) sample.

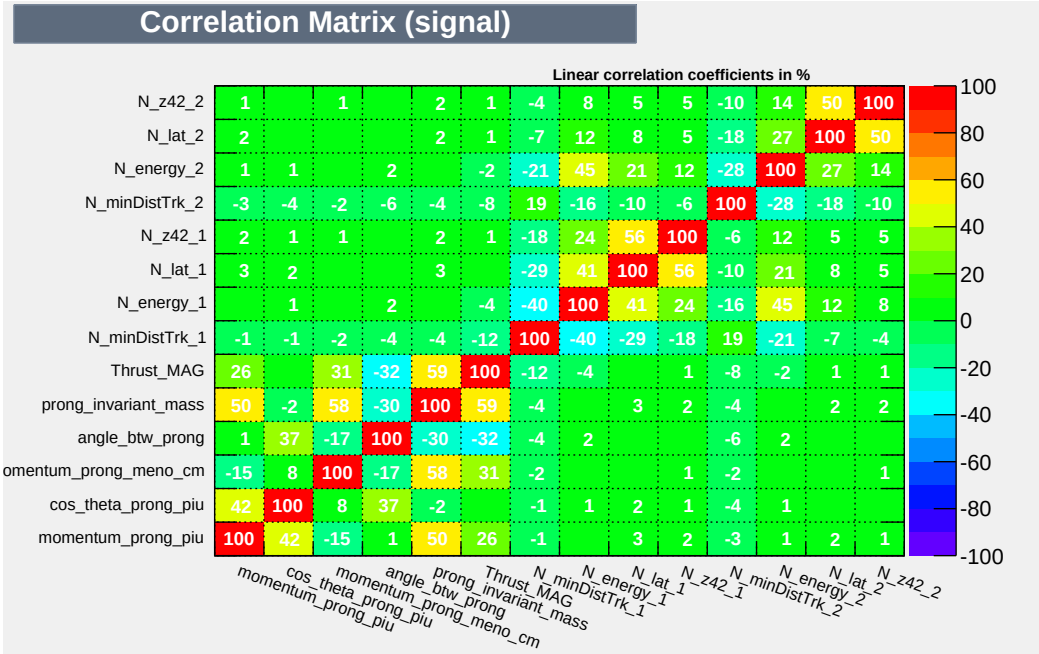

(a)

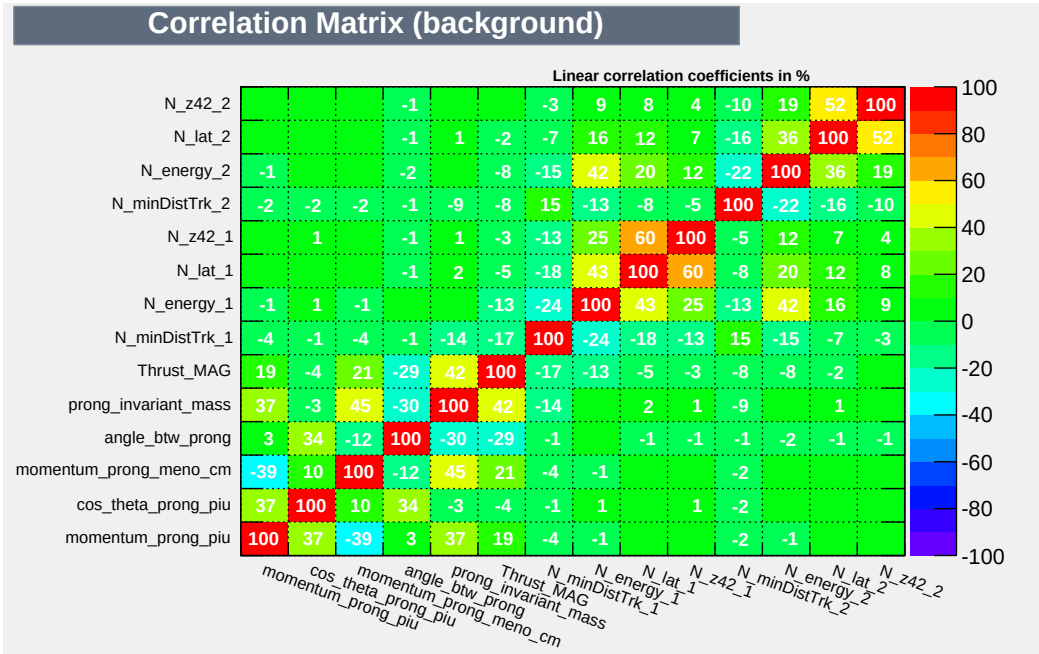

(b)

Figure 4.19: Linear correlation coefficients between the BDT2 variables for the signal (a) and background (b) sample.

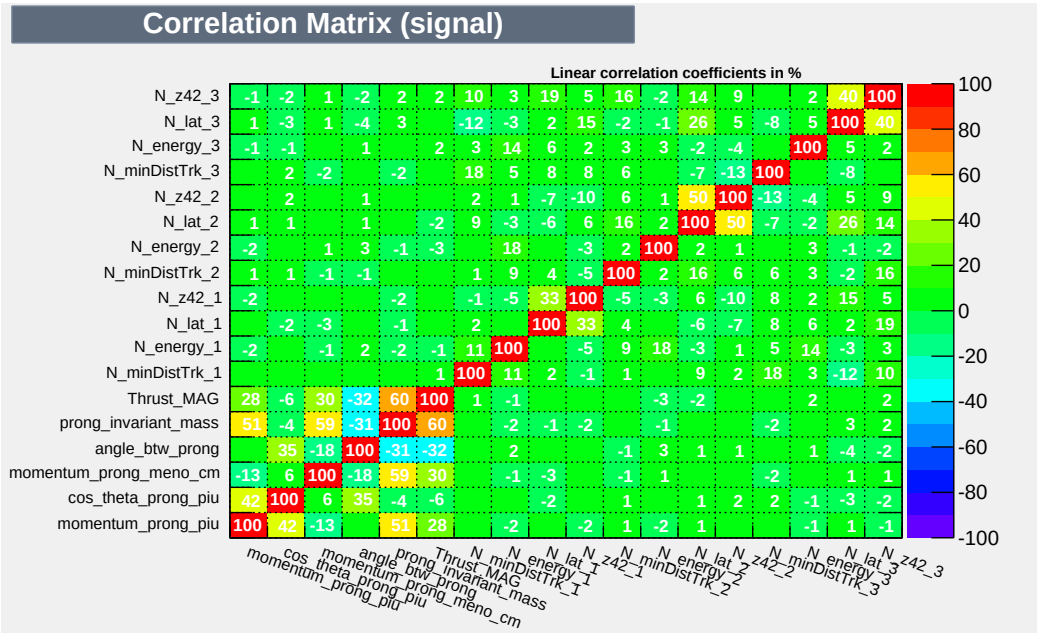

(a)

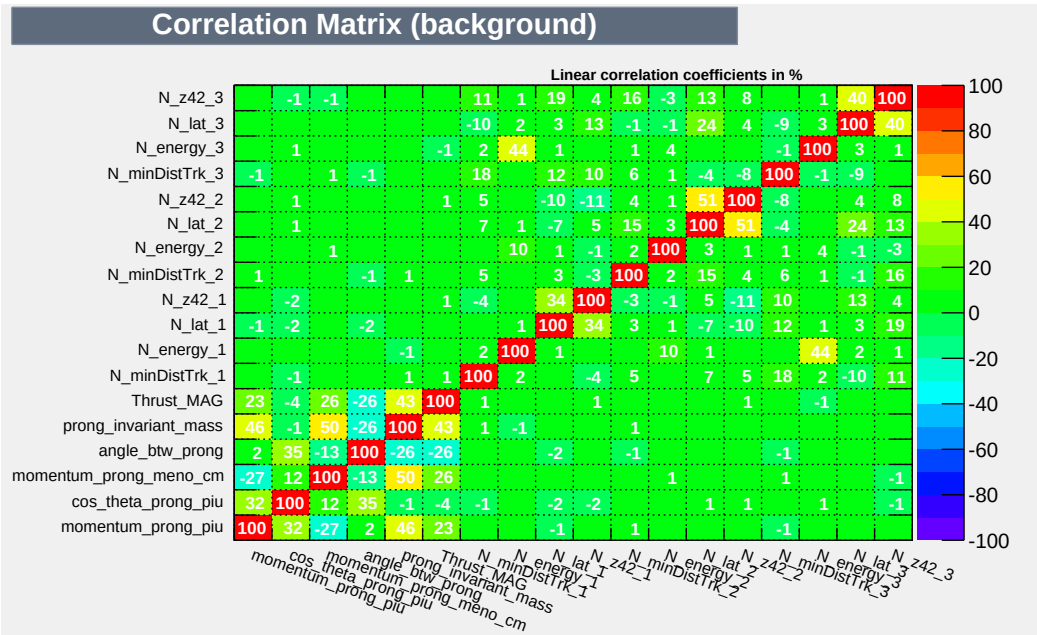

(b)

Figure 4.20: Linear correlation coefficients between the BDT3 variables for the signal (a) and background (b) sample.

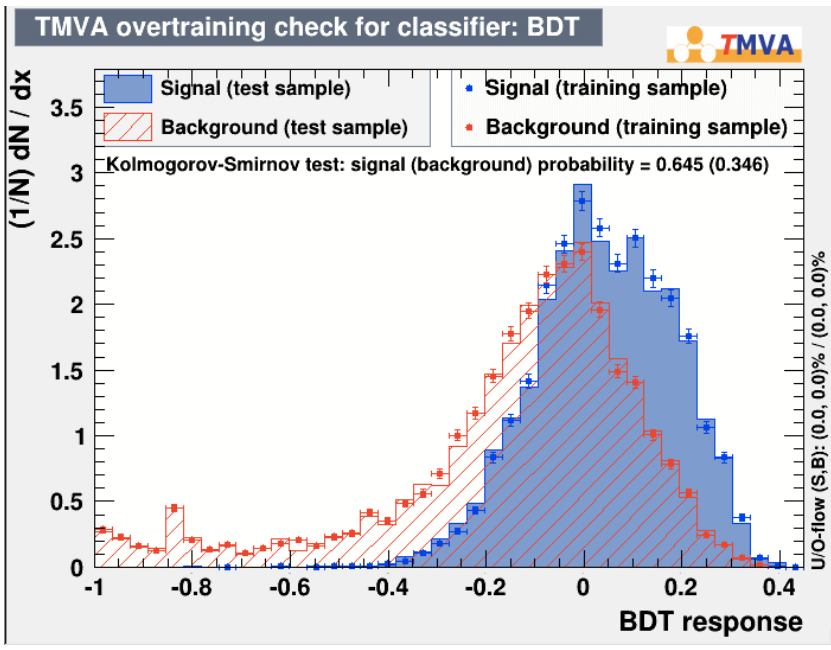

Figure 4.21: BDT0 output for signal and background, test and training sample are superimposed.

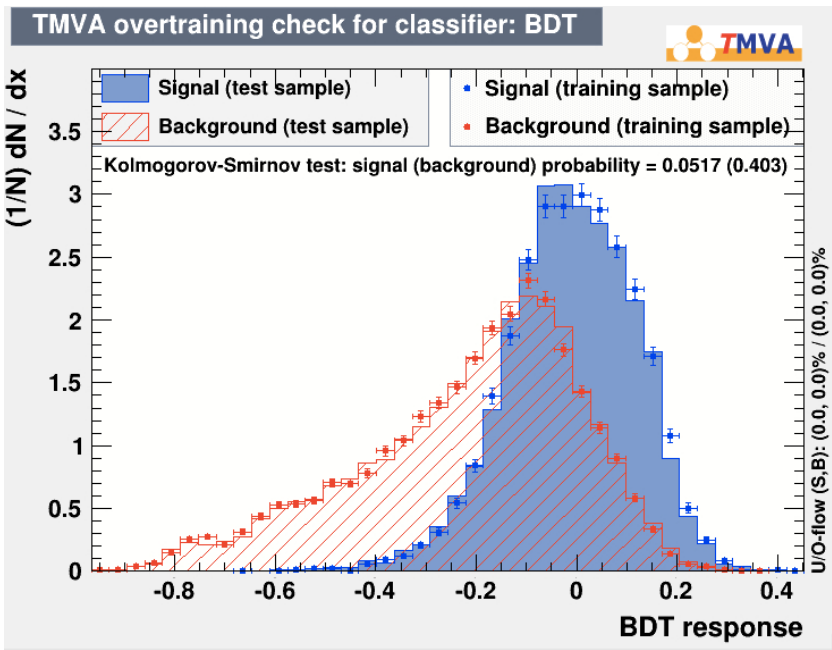

Figure 4.22: BDT1 output for signal and background, test and training sample are superimposed.

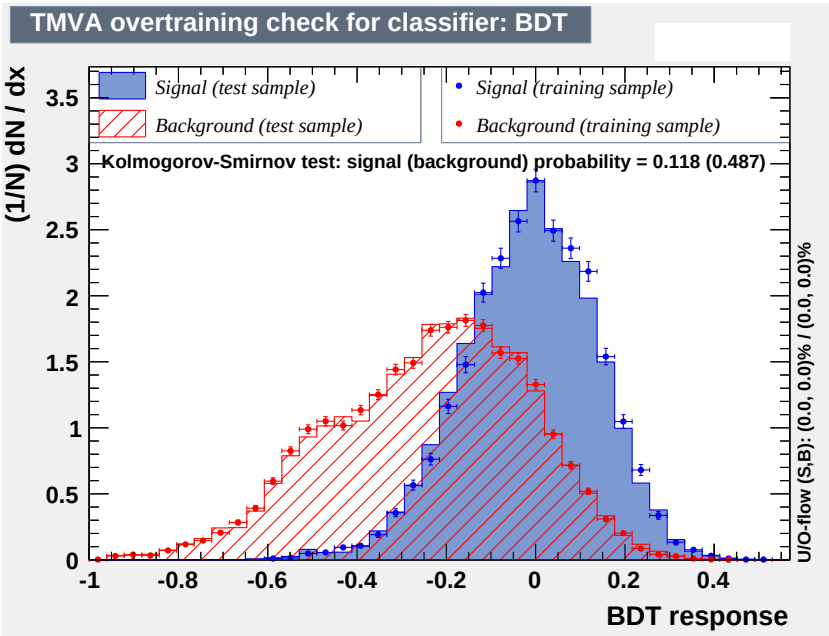

Figure 4.23: BDT2 output for signal and background, test and training sample are superimposed.

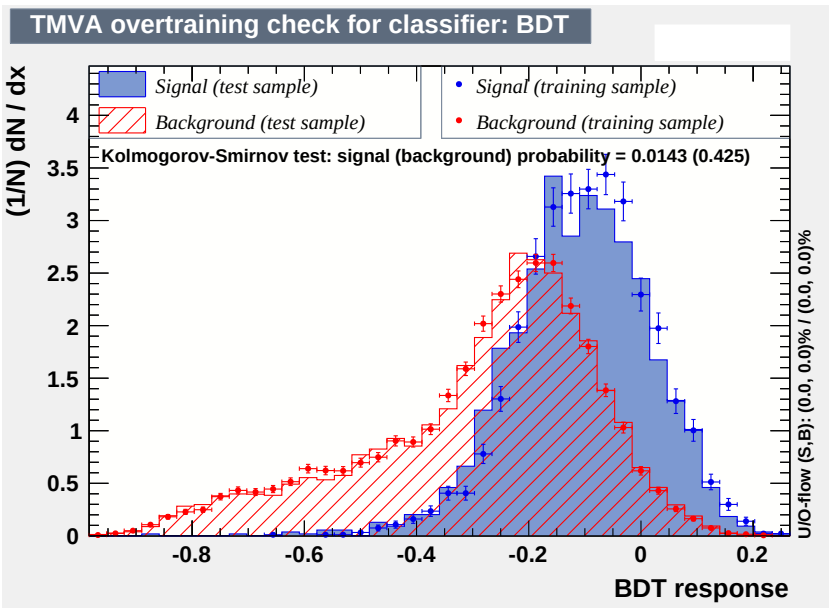

Figure 4.24: BDT3 output for signal and background, test and training sample are superimposed.

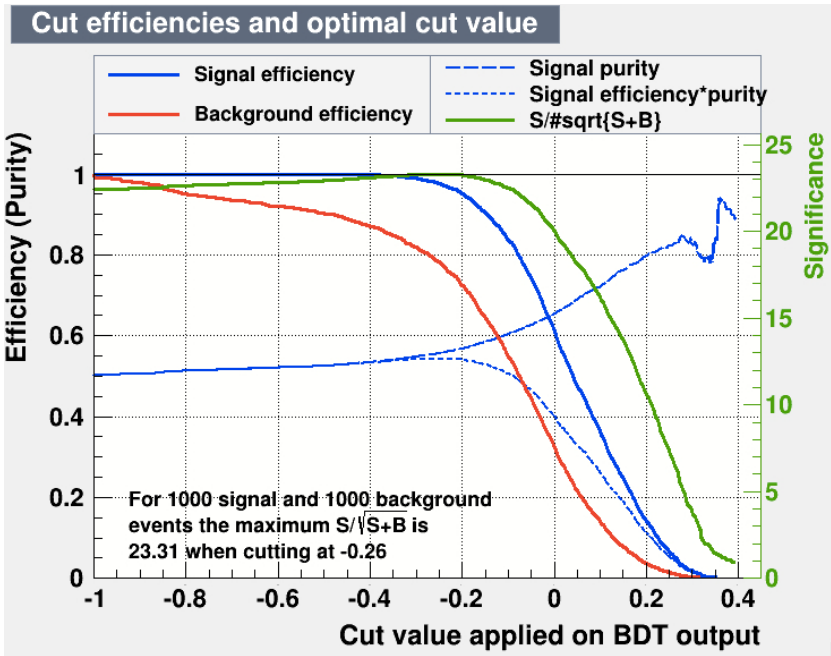

Figure 4.25: BDT0 performance vs output variable cut.

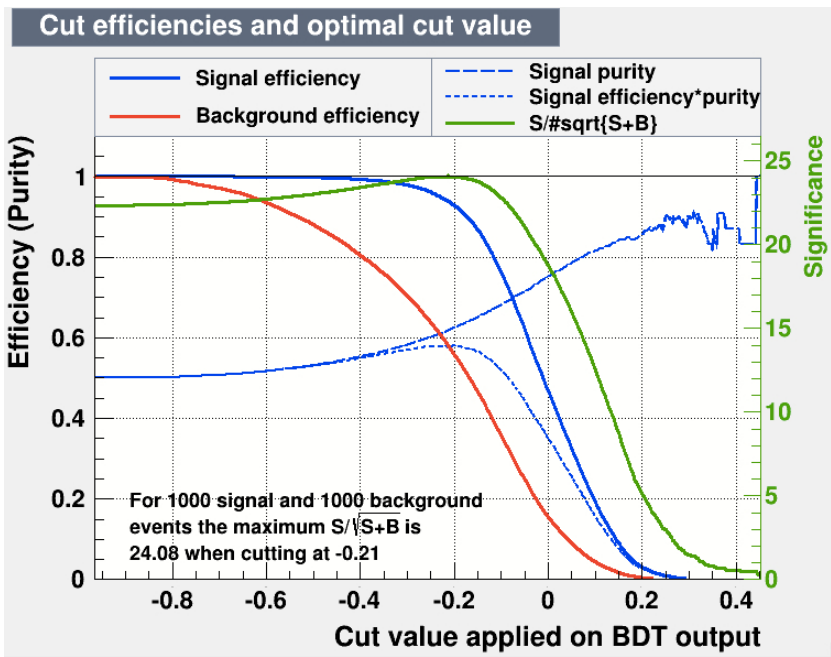

Figure 4.26: BDT1 performance vs output variable cut.

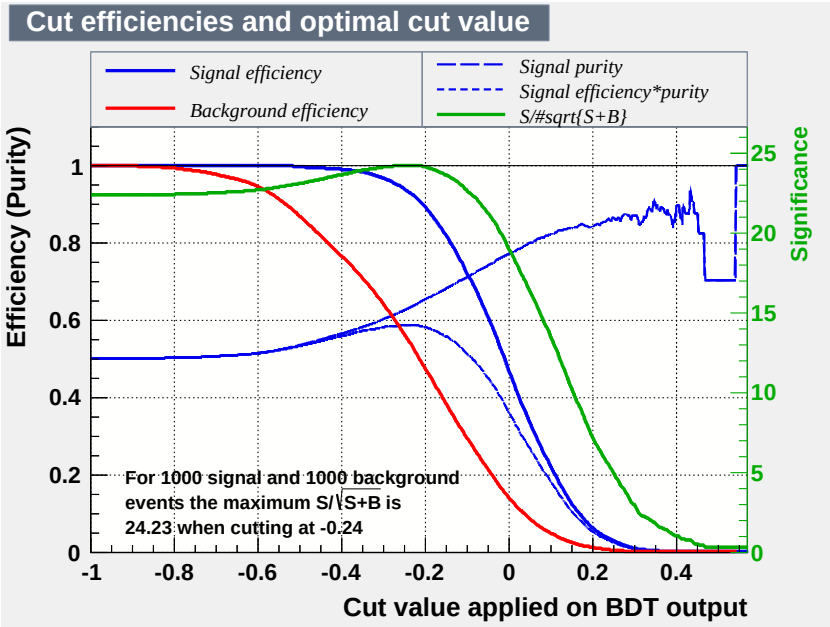

Figure 4.27: BDT2 performance vs output variable cut.

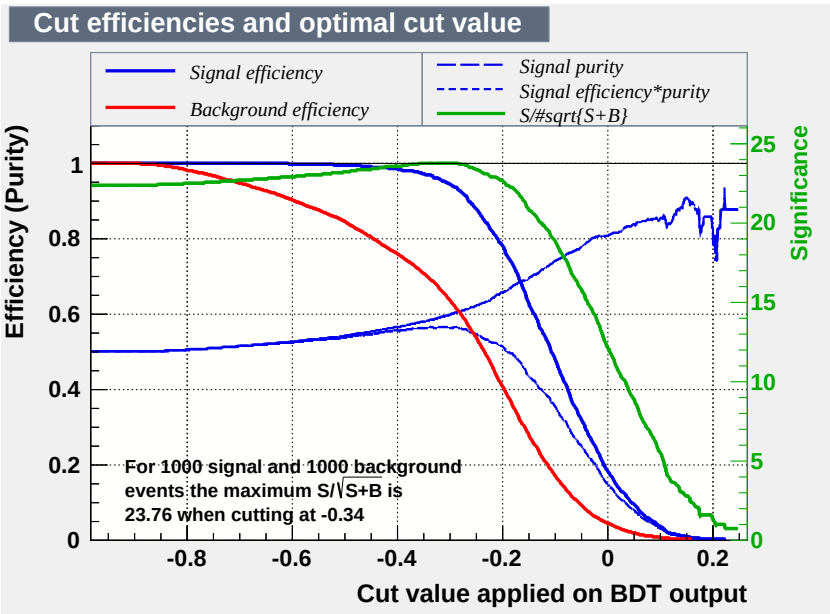

Figure 4.28: BDT3 performance vs output variable cut.

ing from the values in the event of the variables used in the BDT analysis. Once the BDT output is calculated, a cut on this variable is applied. The choice of the cut value depends on the desired compromise between purity and efficiency.

In Figures 4.25, 4.26, 4.27 and 4.28, the BDT performance vs the ouput variable cut for BDT0, BDT1, BDT2 and BDT3 respectively are shown. For each BDT cut value, the signal efficiency (blue line), the background efficiency (red line), the signal purity (blue dashed line), the signal efficiency $\times$ purity (blue dotted line) and the sensitivity $S/\sqrt{S+B}$ (green line) are reported.

The BDT output cuts we have chosen for the events selection are BDT0 output $>$ 0, BDT1 output $>$ 0, BDT2 output $>$ 0 and BDT3 $>$ -0.1. A study for the BDT cuts optimization will be done in the next future to further improve the analysis.

Different MultiVariate Analysis methods have also been compared. In Fig 4.29 the background rejection vs signal efficiency of the BDT (blue), Neutral Network (red), Fisher (green) and Likelihood (black) methods applied to our case are compared for the BDT1 and BDT3 cases. The different classifiers are comparable, with a better performance for the BDT case.

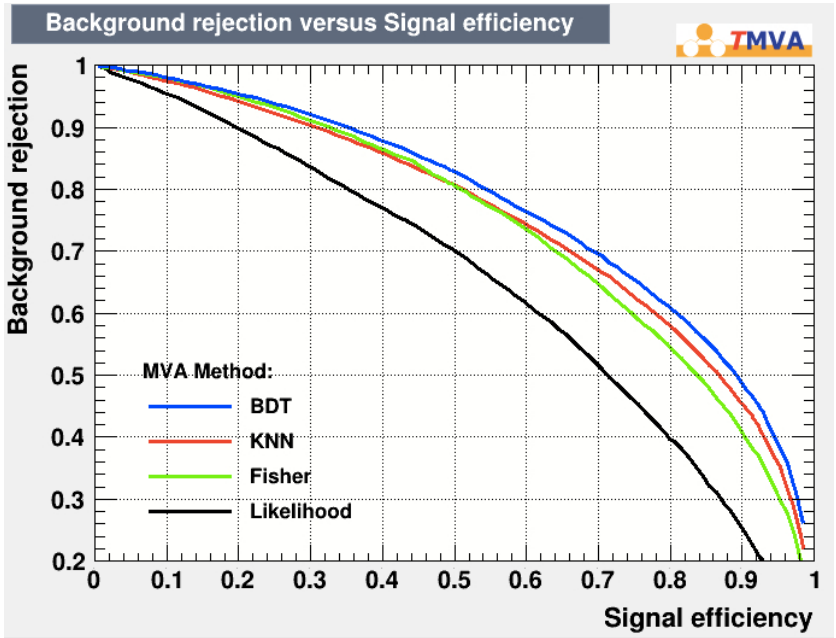

(a)

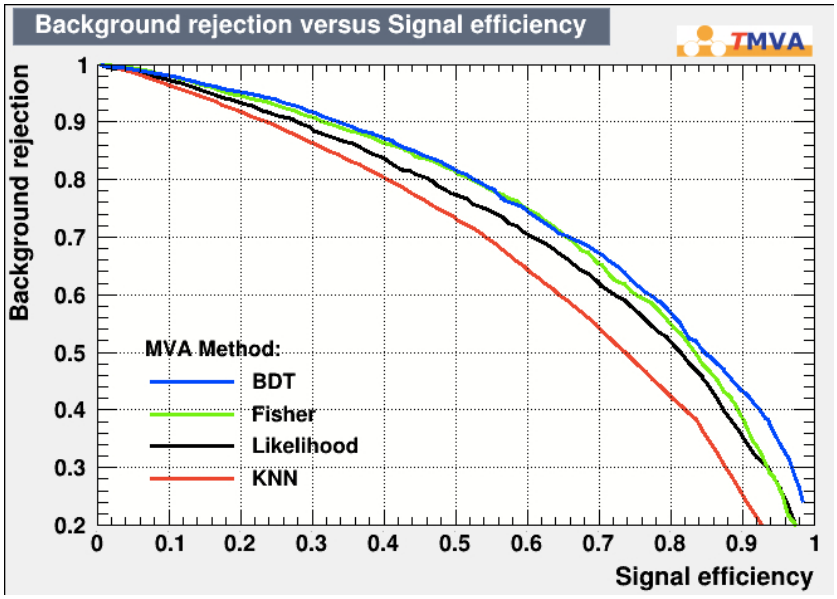

(b)

Figure 4.29: Background rejection vs signal efficiencies for four different Multivariate Analysis methods: BDT, Likelihood, Fisher and ANN for BDT0 (a) and BDT3 (b).

Chapter 5

Results

In this chapter we report the preliminary results obtained with the subsample of 100 fb^{-1} illustrated in the previous chapter. As a first step a detailed comparison between data and MC of the selected sample is performed, the agreement is found to be good, a crucial issue since the τ EDM measurement is a MC-based analysis.

After reconstructing the flight direction and the spin vector of the τ leptons, the observables described in subsection 2.1.1 are measured on the selected data sample.

The MC sample is used to estimate the τ EDM sensitivity. Particular attention is devoted to the EDM effect simulation in the background events. As we will show in the following, we are not able to simulate the d_τ effect for all the τ decay modes because, for some of them, the τ spin reconstruction formula is too complex and we are forced to make some conservative assumption.

A preliminary result is reported.

5.1 Sample composition

In Table 5.1 we show the selected MC sample composition for the four chategories for which the BDT cuts are applied. The number of MC events is normalized to the Data luminosity of 100 fb^{-1}. The reported event numbers do not give the final signal to background ratio because, as will be illustrated in section 5.3, the τ momentum reconstruction procedure will increase the sample purity. In particular this procedure removes more than 80% of the background not coming from τ-pairs events.

Event type	0 neutral cluster BDT0 > 0	1 neutral cluster BDT1 > 0	2 neutral clusters BDT2 > 0	3 neutral clusters BDT3 > -0.1
$\tau^+\tau^- \to (\pi\pi)$	15457	25424	30069	10569
$\tau^+\tau^- \to (\pi\rho)$	822	3786	14462	8139
$\tau^+\tau^- \to (\pi\mu)$	6210	9136	10795	1704
$\tau^+\tau^- \to (\pi e)$	267	443	543	119
$\tau^+\tau^- \to (\rho\rho)$	50	140	963	982
$\tau^+\tau^- \to (\mu\mu)$	479	617	812	50
$\tau^+\tau^- \to (ee)$	3	2	4	0
$\tau^+\tau^- \to (\rho\mu)$	135	569	2574	696
$\tau^+\tau^- \to (\rho e)$	25	43	110	47
$\tau^+\tau^- \to (\mu e)$	41	63	88	13
$\tau^+\tau^- \to$ others	4541	8432	13373	5075
$\mu^+\mu^-$	1244(128)	1516(144)	1152(136)	639(80)
$c\bar{c}$	-	-	-	-
$u\bar{u}, d\bar{d}, s\bar{s}$	30(19)	67(46)	159(103)	125(63)
B^+B^-, B^0B^0	-	-	-	-
bhabha	1126(244)	1072(163)	970(197)	495(75)

Table 5.1: Number of events selected in the MC sample of each cathegory, normalized to the Data luminosity of 100 fb^{-1}. The BDT cuts are indicated. For the not $\tau^+\tau^-$ background the events that survive to the τ flight direction reconstruction procedure are listed in parentheses.

5.2 Data-MC comparison

In Fig. 5.1 we show the momentum module and the *cosθ* distributions for the positive and negative prong tracks for the Data and MC samples selected.

The Data-MC agreement is very good. This important result makes us confident that the EDM sensitivity evaluation will be reliable.

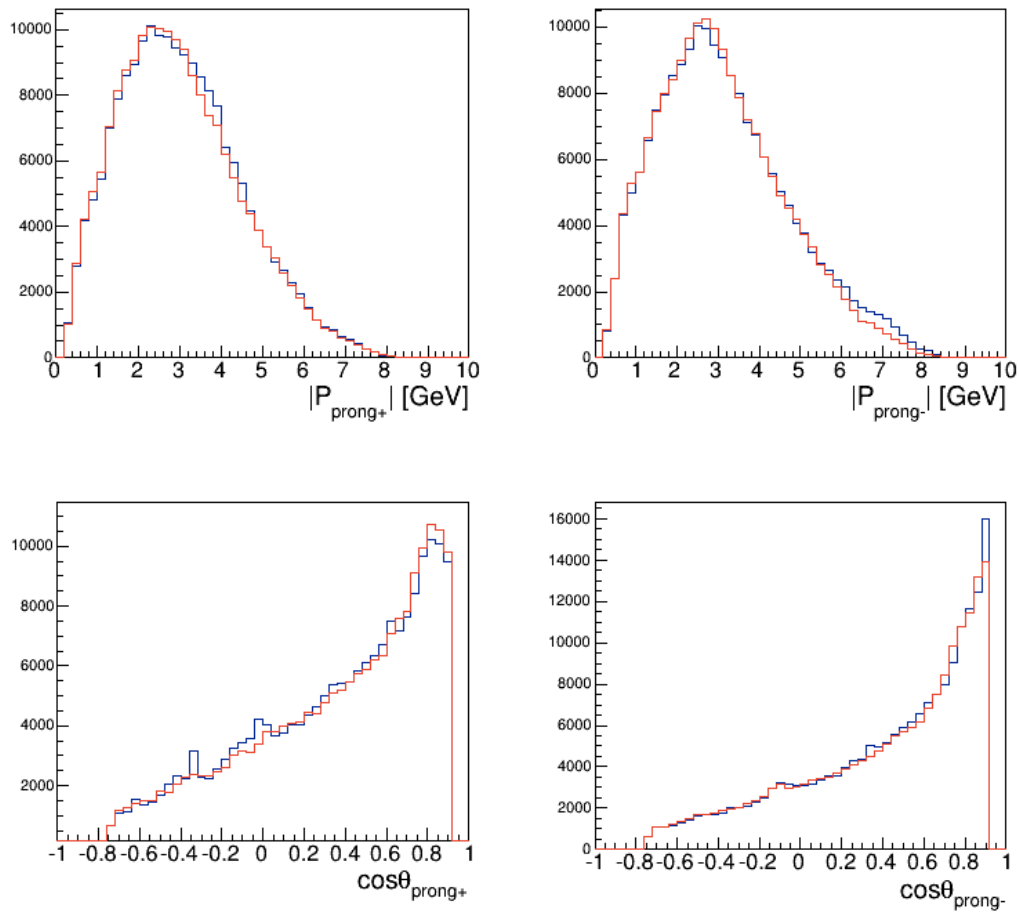

Figure 5.1: Data (blue) and MC (red) comparision for: momentum modul distribution for the positive prong (top left) and for the negative prong (top right), *cosθ* distribution for the positive prong track (bottom left) and for the negative prong track (bottom right).

5.3 Tau momentum reconstruction

In Fig. 5.2 we show the cosine of the angle between the true τ momentum and the reconstructed flight direction for one of the two solutions for all the τ-pair MC events. The plot for the other solution is similar.

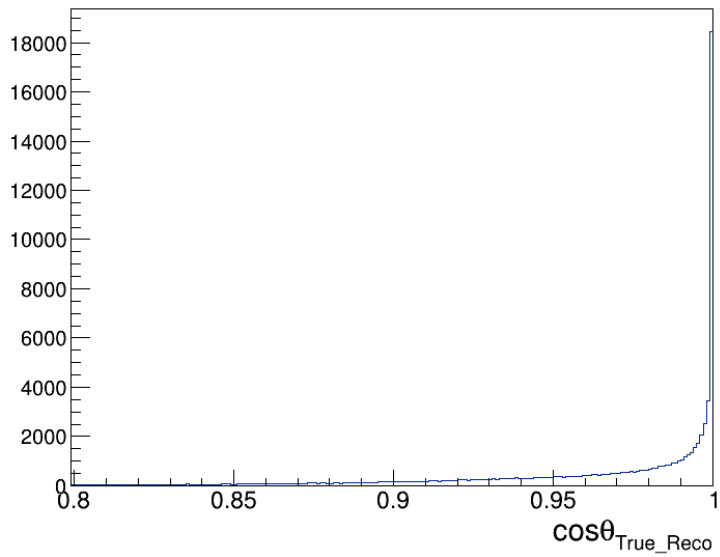

Figure 5.2: Cosine of the angle between the true τ momentum and the reconstructed flight direction for one of the two solutions for all the τ-pair MC events.

In Fig. 5.3 and Fig. 5.4 we show the same distribution for the signal $\tau^+\tau^- \to \pi^+\pi^-\nu_\tau\bar{\nu}_\tau$ and for the $\tau^+\tau^-$ background MC events separately. The signal distribution is characterized by a very sharp peak at one, given by the right solutions ($\simeq 50\%$) and a long tail given by the incorrect solutions ($\simeq 50\%$). The background distribution has a much larger tail.

As we already discussed in the subsection 2.2.1 some events fail the τ flight direction reconstruction procedure: when the Δ in Eq. 2.13 is negative, there are no solutions for the intersection of the two cones constructed around the prong momenta. For the signal events this effect arises when, in case of hard initial state radiation, there is a reduction of the center of mass energy leading to an incorrect center of mass frame system transformation. For the background events this effect can arise because the reconstructed kinematics is miscalculated and leads to non-intersecting cones. The events with $\Delta < 0$ are lost.

The signal lost events are about 12%, the τ-pair background lost events are about 20%. For the background not coming from τ-pairs as $\mu^+\mu^-$ events, bhabha and $u\bar{u}, d\bar{d}, s\bar{s}$, not reported in the plots, the cones do not intersect

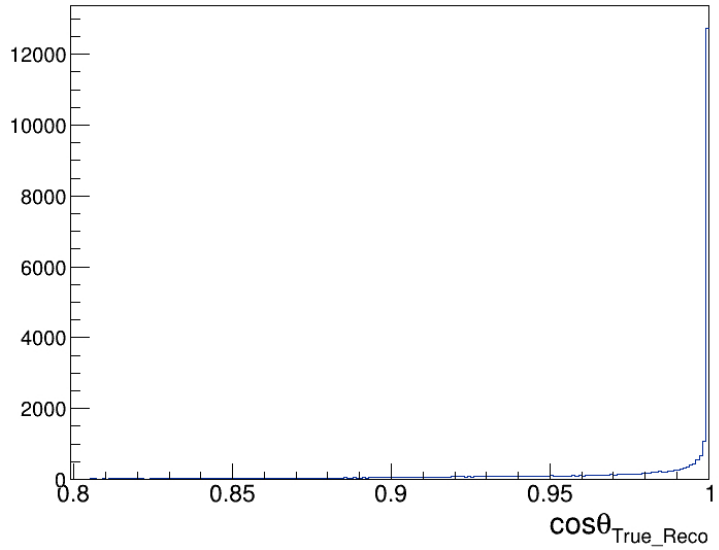

Figure 5.3: Cosine of the angle between the true τ momentum and the reconstructed flight direction for one of the two solutions for the MC singal events $\tau^+\tau^- \to \pi^+\pi^-\nu_\tau\bar{\nu}_\tau$.

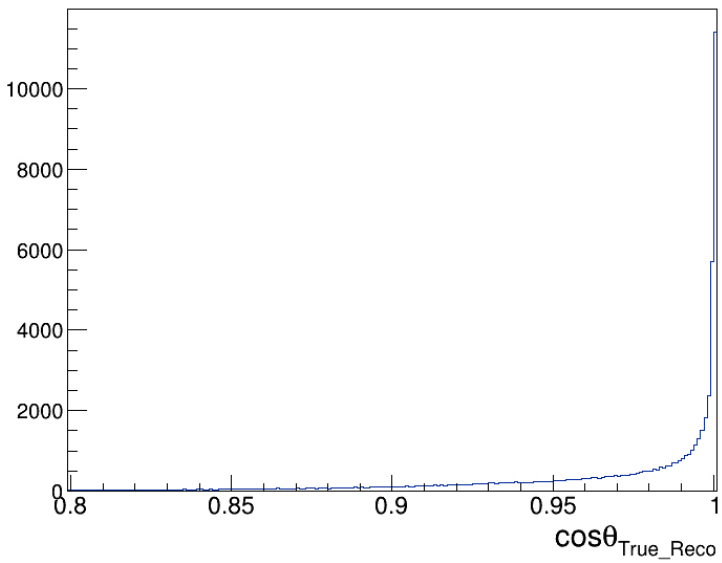

Figure 5.4: Cosine of the angle between the true τ momentum and the reconstructed flight direction for one of the two solutions for the MC $\tau^+\tau^-$ background events.

in about 80% of cases. As a consequence the τ flight direction reconstruction procedure increases the sample purity. In Table 5.2 we report the final purity of the MC samples used to measure the mean values of the optimal observables.

Sample composition	
Signal events ($\pi\pi$)	73923 events (47 %)
$\tau^+\tau^-$ background with **known** d_τ effect	54761 events (35 %)
$\tau^+\tau^-$ background with **unknown** d_τ effect	27379 events (17 %)
not $\tau^+\tau^-$ background	1400 events (1 %)

Table 5.2: Selected MC sample final composition after the τ momentum reconstruction procedure.

In Table 5.3 the total number of data selected is compared with the equally selected MC events normalized to the data luminosity.

MC events	157463
Data events	153820

Table 5.3: Number of MC events (normalized to the Data luminosity) and Data events for the selected sample.

5.4 Tau Spin Vector reconstruction

In Fig. 5.5 and Fig. 5.6 we show the two solutions for the reconstructed τ^+ and τ^- spin vectors respectively, for the τ-pairs MC selected sample. The dotted lines represent the signal distributions. The result is consistent with the distributions obtained for the spin with the ideal MC sample and shown in subsection 2.2.2.

5.5 Observable distributions

In Fig.5.7 we show the $\mathcal{O}_{Re}$ and $\mathcal{O}_{Im}$ (see Eq. 2.3) distribution for Data and MC samples. In Fig. 5.8 we highlight the signal contribution to the $\mathcal{O}_{Re}$ and

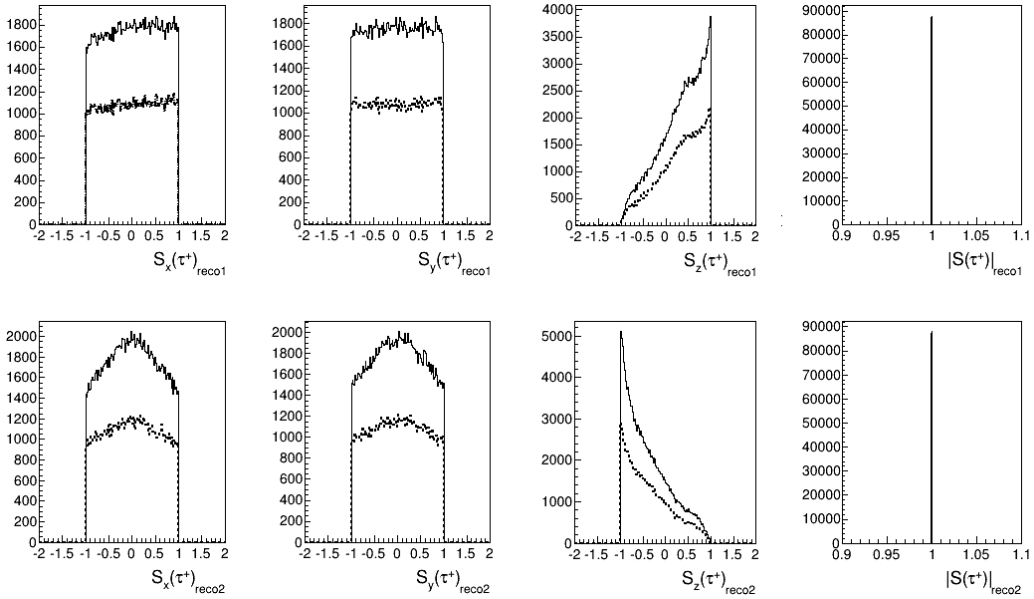

Figure 5.5: Distribution of the τ^+ spin vector components and module, for the $\tau^+\tau^-$ selected MC events. Top: $+\Delta$ solution. Bottom: $-\Delta$ solution. The dotted lines represent the signal.

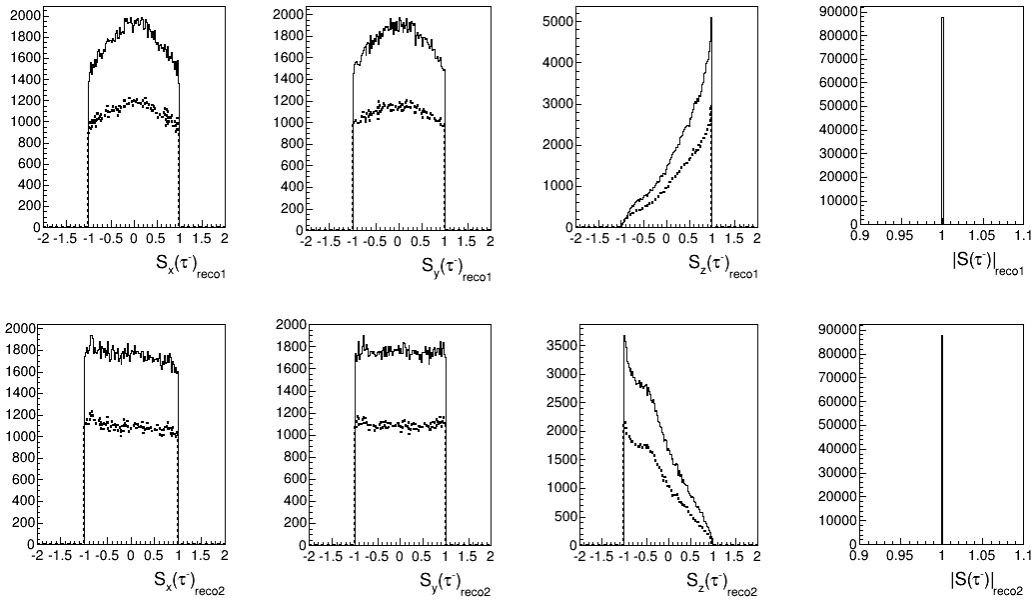

Figure 5.6: Distribution of the τ^- spin vector components and module, for the $\tau^+\tau^-$ selected MC events. Top: $+\Delta$ solution. Bottom: $-\Delta$ solution. The dotted lines represent the signal.

$\mathcal{O}_{Im}$ given by the MC distributions. In Table 5.4 we report the means of the real and imaginary observable distributions of Data with their statistical error.

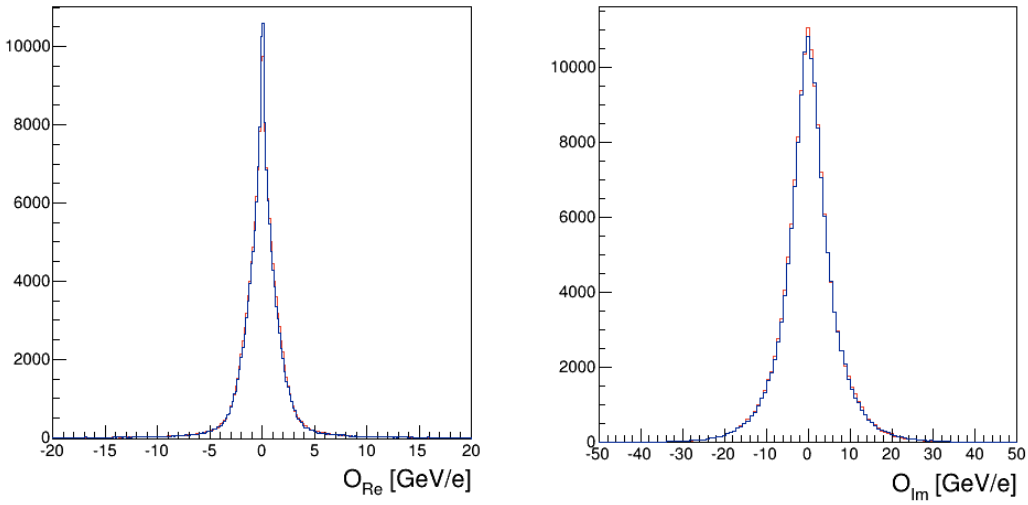

Figure 5.7: Real (left) and imaginary (right) observable distributions for the data (blue) and MC (red) samples.

$\langle \mathcal{O}_{Re} \rangle_{Data}$ [GeV/e]	-0.0006 ± 0.0051
$\langle \mathcal{O}_{Im} \rangle_{Data}$ [GeV/e]	0.148 ± 0.018

Table 5.4: Mean values of the real and imaginary observable Data distributions.

5.6 EDM sensitivity evaluation

For the τ EDM sensitivity evaluation we introduce in the selected MC sample different values of the EDM and measure the observable means in the different cases. As already mentioned in section 2.3, the effect of $d_\tau \neq 0$ is modeled weighting each event by the ratio (Eq. 2.26):

$$w = \frac{(\mathcal{M}^2_{prod})_{EDM}}{\mathcal{M}^2_{SM}} = \frac{\mathcal{M}^2_{SM} + Re(d_\tau)\mathcal{M}^2_{Re} + Im(d_\tau)\mathcal{M}^2_{Im} + |d_\tau|^2\mathcal{M}^2_{d^2}}{\mathcal{M}^2_{SM}},$$

where the matrix elements $\mathcal{M}^2_{SM}$, $\mathcal{M}^2_{Re}$, $\mathcal{M}^2_{Im}$ and $\mathcal{M}^2_{d^2}$, given explicitely in Equations 1.23, 1.24, 1.25 and 1.26, depend on the τ^+ momentum in the center of mass frame system and on the τ^+ and τ^- spin vectors. To calculate

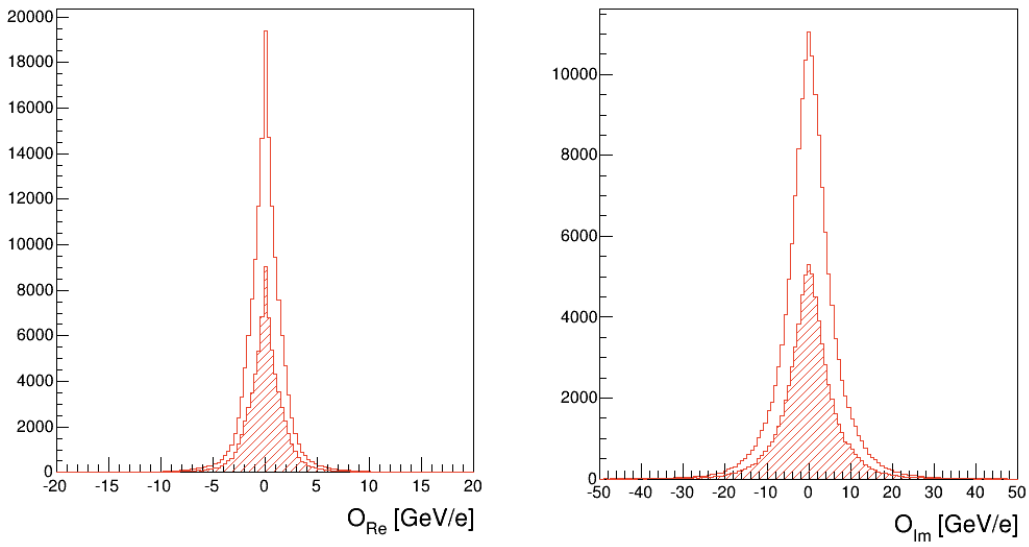

Figure 5.8: Real (left) and imaginary (right) observable distributions for the MC sample, the dashed line is the signal contribution.

the physical EDM effect we have to use the MC truth information. The true τ^+ momentum is known, but the true τ lepton polarization information is not stored in the MC truth.

The application of a dedicated package, TauSpinner [59], capable of extracting the τ polarization from the daughters angular distribution is under consideration but for the time being we know the spin reconstruction analytical formulae only for the cases illustrated in subsection 2.2.2, $\tau^\pm \to \pi^\pm \nu_\tau$, $\tau^\pm \to \rho^\pm(\pi^\pm\pi^0)\nu_\tau$, and $\tau^\pm \to l^\pm \nu_\tau \nu_l$. Then, only if the two tau leptons decay in a combination of these four possibilities, we are able to correctly simulate the $d_\tau \neq 0$ effect.

Not only the signal is affected by the dipole moment, also the $\tau^+\tau^-$ background is sensitive to the EDM value. However for the background events the observables are calculated with the wrong $(\pi\pi)$ assumption and a reduced sensisivity is expected. A detailed study of the different samples behaviour is necessary to understand the sample purity importance and to reach an estimate of the systematics.

In Fig. 5.9 we show the correlation between $\langle \mathcal{O}_{Re} \rangle$ ($\langle \mathcal{O}_{Im} \rangle$) and $Re(d_\tau)$ ($Im(d_\tau)$) for the MC sample selected considering only the signal events, in Fig. 5.10 we show the same plots for the background events for which the matrix elements and the EDM effect can be calculated.

At this stage, we don't know the real sensitivity to the EDM of the whole background. For the moment we make the conservative assumption that

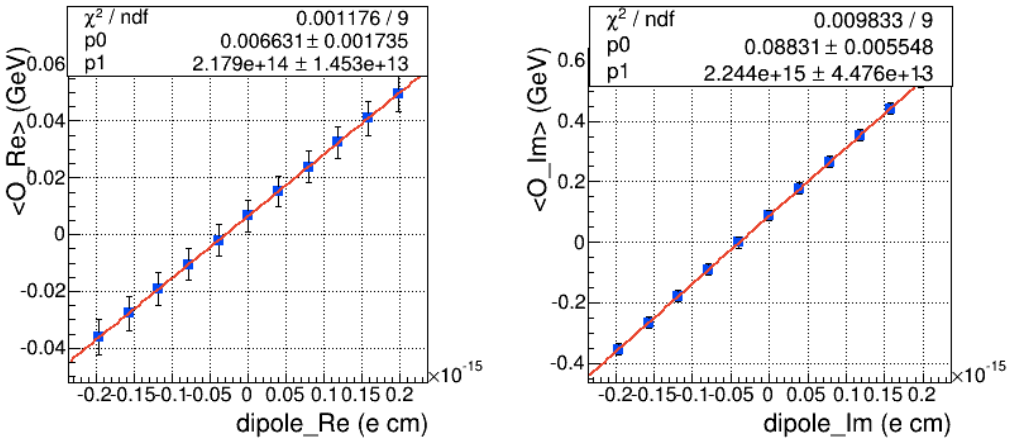

Figure 5.9: Real (left) and imaginary (right) observable mean vs real and imaginary dipole moment variation for the signal ($\pi\pi$) MC events.

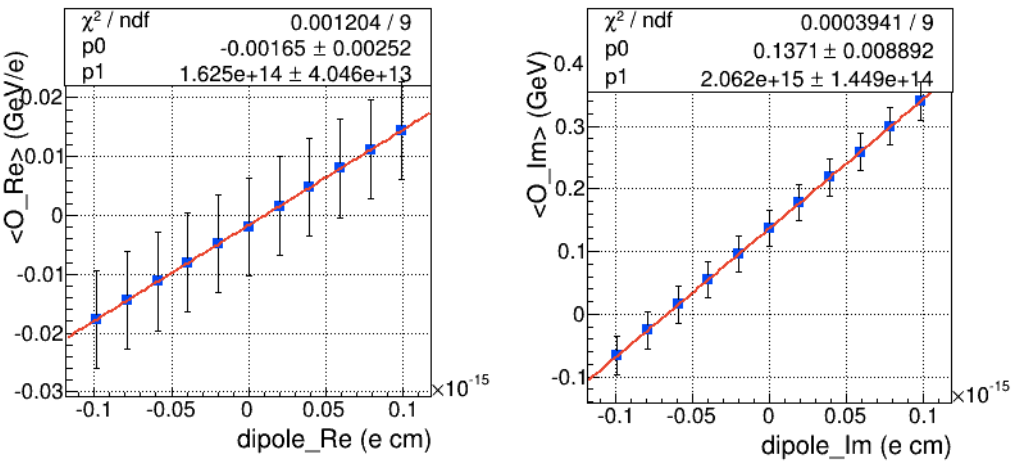

Figure 5.10: Real (left) and imaginary (right) observable mean vs real and imaginary dipole moment variation for the MC background for which we are able to correctly simulate the EDM effect.

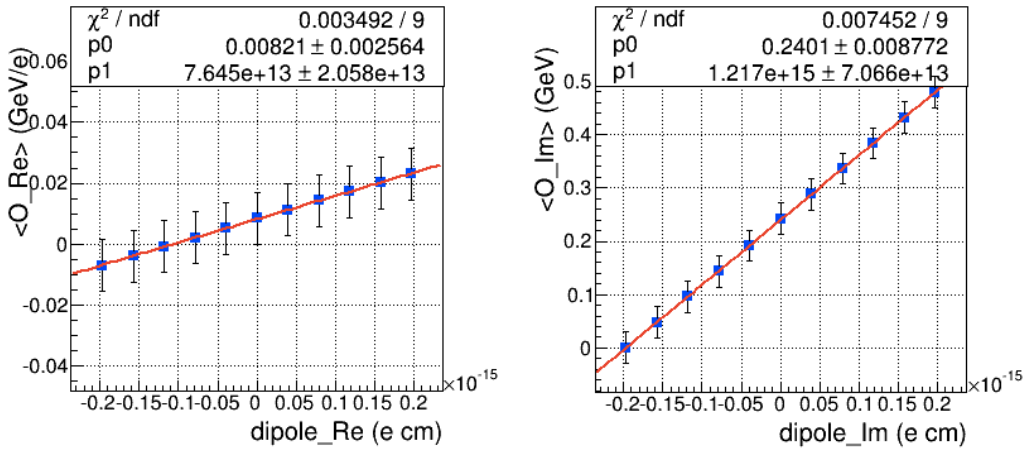

Figure 5.11: Real (left) and imaginary (right) observable mean vs real and imaginary dipole moment variation for the $(\pi\rho)$ background, the less sensitive to the τ EDM.

the background with unknown EDM effect will behave as the less sensitive backgorund to the EDM, that is the $(\pi\rho)$ background, which sensitivity is illustrated in Fig 5.11.

a^S_{Re} $(10^{14}e^{-1}\text{cm}^{-1})$	2.18 ± 0.14
a^S_{Im} $(10^{15}e^{-1}\text{cm}^{-1})$	2.24 ± 0.04
a^{KB}_{Re} $(10^{14}e^{-1}\text{cm}^{-1})$	1.62 ± 0.40
a^{KB}_{Im} $(10^{15}e^{-1}\text{cm}^{-1})$	2.06 ± 0.14
$a^{\pi\rho}_{Re}$ $(10^{14}e^{-1}\text{cm}^{-1})$	0.76 ± 0.20
$a^{\pi\rho}_{Im}$ $(10^{15}e^{-1}\text{cm}^{-1})$	1.22 ± 0.07

Table 5.5: Fit results for the slope parameter of the $\langle\mathcal{O}_i\rangle$ vs d_τ trend. S is the signal sample, KB is the $\tau^+\tau^-$ background sample for which the EDM effect is known and $\pi\rho$ is the $(\pi\rho)$ background sample.

In Table 5.5 we report the slope parameter values a_i given by a linear fit for all the considered samples: signal sample, treatable background sample and $(\pi\rho)$ sample.

We expect that the highest sensisivity is obtained for the pure signal sample. Nevertheless also the $\tau^+\tau^-$ background has a significant sensitivity to the EDM and the most appropriate trade-off between efficiency and purity must be found to optimize the results.

In Table 5.6 we report the real and imaginary offset values b^T_{Re} and b^T_{Im} for the full data-like MC samples selected. These values are given by the real

and imaginary observable distribution means with $d_\tau = 0$. The real offset b^T_{Re} is compatible with zero, the imaginary offset b^T_{Im} has a value far from zero revealing an intrinsic asymmetry. This result is expected. As mentioned in subsection 1.5.1, the $\mathcal{M}^2_{Re}$ matrix element is related to the spin projection on the beam and τ flight direction transverse plane, on the contrary the $\mathcal{M}^2_{Im}$ matrix element is related to the spin projection along the beam and τ flight direction axis. In the first case a very small asymmetry could appear due to the small *BABAR* tilt between the detector and the beam axis, while in the second case, the PEP-II boost brought to a significant asymmetry in the *BABAR* detector acceptance. This feature can introduce a correlation between the imaginary observable mean and the BDT cuts.

$b^T_{Re}[GeV/\mathrm{e}]$	0.0046 ± 0.0037
$b^T_{Im}[GeV/\mathrm{e}]$	0.136 ± 0.013

Table 5.6: b_{Re} and b_{Im} values. The offsets are given by the real and imaginary MC observable distribution means respectively, in the $d_\tau = 0$ case.

5.7 EDM measurement

Starting from the linear relations:

$$\langle \mathcal{O}_{Re} \rangle = a_{Re} \cdot Re(d_\tau) + b_{Re},$$
$$\langle \mathcal{O}_{Im} \rangle = a_{Im} \cdot Im(d_\tau) + b_{Im},$$

and calculating the effective sensitivities a_i^{eff} (where $i = Re, Im$) as:

$$a_i^{eff} = a_i^S \cdot f_S + a_i^{KB} \cdot f_{KB} + a_i^{\pi\rho} \cdot f_{UB}, \tag{5.1}$$

where f_S, f_{KB} and f_{UB} indicate the signal and the treatable and untreatable background fractions, we can extract a preliminary estimate of the real and imaginary part of the τ EDM:

$$Re(d_\tau) = (2.32 \pm 3.66) \times 10^{-17}\, e\,\mathrm{cm},$$
$$Im(d_\tau) = (0.61 \pm 1.12) \times 10^{-17}\, e\,\mathrm{cm},$$

The values are compatible with a zero EDM. The measurement sensitivity is better than the Belle one scaled at the same luminosity.

Different BDT cuts must be considered to optimize the sensitivity and systematic errors must be evaluated.

5.8 Systematic errors evaluation

The main systematic effects under evaluation are:

- **Data - MC discrepancy**

  A critical point of this analysis lies in the full MC simulation, since the conversion parameters from the observables to the EDM are extracted using the MC with different EDM values. The systematic uncertainties in the knowledge of the detector acceptance and efficiency must not be studied independently because the relevant systematic effects are automatically reflected into a mismatch between data and MC. A detailed study of the systematic error related to the data-MC discrepancy will be performed.

- **Background fake rate**

  The determination of the sample purity, based on simulation, leads to a systematic effect on the parameters describing the EDM offset and sensitivity, since the background contamination affects the relation between $\langle \mathcal{O}_i \rangle$ and EDM. The purity uncertainty and its effect on the EDM sensitivity must be evaluated.

- **Observable means evaluation**

  It has been verified that the mean values of the observable distributions, both in data and MC samples, significantly change with the different BDT output cuts. Data and MC results are consistent but a more detailed study of the mean values trends must be performed.

- **Treatment of background with unknown EDM effect**

  For about 17% of events we are unable to correctly calculate the EDM effect. Different assumption on the behaviour of this background give different results. The study of these differences allows an evaluation of the related systematics.

- **Initial state radiation**

  The initial state radiation effect is not considered in the τ-pair rest frame system reconstruction, because radiated photons are not detected. In the hard radiation cases the lack of information could modify the EDM effect calculation. Both MC and data are analized with the same undetected radiation, nevertheless we plan to switch off the initial state radiation in the MC to study possible systematics on the EDM sensitivity evaluation.

Conclusions

Results

In this thesis a preliminary *BABAR* measurement of the τ electric dipole moment (EDM) has been performed. The τ EDM search is a measurement of the CP violation in the leptonic sector. A non-zero EDM would indicate the presence of new physics beyond the Standard Model (SM), since SM does not predict any appreciable effect in the lepton sector at the experimental sensitivity, while new physics can produce larger CP-violation. This CP-violation effect is expected to be enhanced for τ leptons due to their large mass. A zero EDM measurement with high sensitivity sets new constraints to new physics theories.

The analysis was performed on 100 fb^{-1}, a fraction of the whole data sample accumulated by the *BABAR* experiment at the PEP-II asymmetric e^+e^- collider built at SLAC (California) with a center of mass energy of $\sqrt{s} = 10.58$ GeV. In the collisions τ-pairs are copiously produced via the process $e^+e^- \to \tau^+\tau^-$.

The *optimal observable method* was adopted to extract the τ EDM, which uses all the experimentally available information of the spin and momenta of the τ decays, and maximizes the sensitivity to the EDM.

Presently only one final state in the decay of τ-pairs has been analysed: $\tau^- \to \pi^-\nu_\tau$, $\tau^+ \to \pi^+\bar{\nu}_\tau$. The analysis started with the $\pi^\pm$ decay channel because the double body decay ensure the best τ flight direction reconstruction and it is simpler, not requiring the π^0 reconstruction in the calorimeter. The event selection was performed in two steps, a cut-based preselection followed by a multivariate analysis (BDT).

The conversion parameters leading from the observables to the EDM value are extracted with a full Monte Carlo (MC) where different EDM hypoteses have been simulated. The effect of the electric dipole moment on the means of the optimal observable distributions $\langle \mathcal{O}_i \rangle$ was studied.

The preliminary result for the real and imaginary part of the τ EDM, obtained with the 100 fb^{-1} sample, corresponding to about 80 millions of

τ-pairs produced, is:

$$Re(d_\tau) = (2.32 \pm 3.66) \times 10^{-17}\, e\,\mathrm{cm},$$
$$Im(d_\tau) = (0.61 \pm 1.12) \times 10^{-17}\, e\,\mathrm{cm}.$$

The results are consistent with zero-EDM and show no evidence of CP-violation. For the time being, only the statistical error was evaluated and here reported. Thanks to the larger selection efficiency of the present analysis, the statistical sensitivity to the τ EDM in the $\pi^+\pi^-\nu_\tau\bar{\nu}_\tau$ final state is better compared to the previous Belle experiment measurement when rescaled to the same luminosity (30 fb^{-1}). A complete evaluation of the systematic uncertainties still has to be performed.

Analysis extension and improvement

After systematics evaluation, next steps to optimize and complete the τ EDM measurement at *BABAR* will be the following:

- optmize the BDT output cut value for the signal events selection to reach the best compromise between purity and efficiency, ensuring the highest EDM sensitivity;
- extend the analysis to the full *BABAR* data sample of 425 fb^{-1};
- add the $\tau^\pm \to \rho^\pm\nu_\tau$ channel to the analysis. This τ decay has a branching ratio $\sim 25\%$, ensuring higher statistics. The τ flight direction reconstruction algorithm is the same as in the $\tau^\pm \to \pi^\pm\nu_\tau$ case, with the advantage that the anglurar distribution of the $\rho^\pm \to \pi^\pm\pi^0$ decay products provides information on the τ spin which survives the averaging procedure between the two τ momentum solutions. Consequently the observable distributions for the ρ decay events are wider, resulting in a higher EDM sensitivity.

Appendix A

Optimal Observables

Let us consider the general problem of observing the change in the differential cross section due to the addition of any small coupling. Define the differntial cross section:

$$\sigma(\phi) = d\phi, \tag{A.1}$$

where ϕ represents the relevant phase-space variables being considered. If there is a small contribution to the differential cross section controlled by a parameter λ, the differential cross section can be expanded in terms of λ as

$$\sigma = \sigma_0 + \lambda\sigma_1. \tag{A.2}$$

if one has an ideal detector that records accurately the value of ϕ for each event that occurs, any method for determining the value of λ amounts to weighting the events with a phase-space-dependent function $f(\phi)$ and calculating the quantity

$$f^{(1)}(\lambda) = \int f(\phi)\sigma(\phi)d\phi, \tag{A.3}$$

as compared to the value if $\lambda = 0$:

$$f^{(1)}(0) = \int f(\phi)\sigma_0(\phi)d\phi. \tag{A.4}$$

Thus, the change due to the presence of λ is given by

$$\delta_f = f^{(1)}(\lambda) - f^{(1)}(0) = \lambda \int f(\phi)\sigma_1(\phi)d\phi. \tag{A.5}$$

We must now compare δ_f with the error in measuring $f^{(1)}$. If n events are recorded, this error will be given by

$$\Delta f = \sqrt{\frac{\int f^2(\phi)\sigma(\phi)d\phi}{n\int \sigma(\phi)d\phi}}, \tag{A.6}$$

Let us now define the *resolving power* R of the function f in terms of the appropriately normalized ratio of these two quantities by

$$R = \frac{1}{n\lambda^2}\frac{\delta_f^2}{(\Delta f)^2} = \frac{(f^{(1)}(\lambda) - f^{(1)}(0))^2}{\lambda^2 \int f(\phi)^2\sigma(\phi)d\phi \int \sigma(\phi)d\phi} = \frac{\left[\int f(\phi)\sigma_1 d\phi\right]^2}{\int \sigma(\phi)d\phi \int f^2(\phi)\sigma_0 d\phi}. \tag{A.7}$$

Thus, the statistical significance S with which the presence of a nonzero value of λ may be ascertained is

$$S = \frac{\delta_f}{\Delta f} = \lambda\sqrt{nR}. \tag{A.8}$$

The larger the value of R, the more effective f is for measuring λ, so that one would like to use a function f for which R is maximal.

In order to find such an optimal function, which we will denote f_{opt}, it is useful to decompose an arbitrary function f as

$$f = A \cdot \frac{\sigma_1}{\sigma_0} + \hat{f}, \tag{A.9}$$

where

$$A = \frac{\int f\sigma_1 d\phi}{\int \frac{\sigma_1^2}{\sigma_0}d\phi}. \tag{A.10}$$

Therefore, $\hat{f}$ has the property that $\int \hat{f}\sigma_1 d\phi = 0$.

Clarly, rescaling f does not change the value of R; therefore, without loss of generality we take $A = 1$. Thus, if we expand the definition of R to lowest order in λ and use the above decomposition, we obtain

$$R\int \sigma(\phi)d\phi = \frac{\left(\int f\sigma_1 d\phi\right)^2}{\int f^2\sigma_0 d\phi} = \frac{\left(\int \frac{\sigma_1^2}{\sigma_0}d\phi\right)^2}{\int \frac{\sigma_1^2}{\sigma_0}d\phi + \int \hat{f}^2\sigma_0 d\phi}. \tag{A.11}$$

Examining the denominator we note that if $\hat{f}$ is nonzero, the expression $\int \hat{f}^2\sigma_0 d\phi$ is positive, and since the expression $\int \sigma_1^2/\sigma_0 d\phi$ is also always positive, R is maximized when $\hat{f} = 0$. R is therefore maximized when

$$f = f_{opt} = \frac{\sigma_1}{\sigma_0} \tag{A.12}$$

A.0.1 Comparision with a likelihood fit

Let's compare the optimal observable method with the maximum-likelihood fit method. Using the differential cross section given in Eq. A.2, the likelihood function $\mathcal{L}(\phi_i, \lambda)$ can be written as

$$\mathcal{L}(\phi_i, \lambda) \sim \prod_i \sigma(\phi_i) = \prod_i \left[\sigma_0(\phi_i) - \lambda\sigma_1(\phi_i)\right]. \tag{A.13}$$

The true parameter λ_0 maximizes the likelihood and satisfies the equation

$$\frac{\partial}{\partial\lambda} log\mathcal{L} \mid_{\lambda=\lambda_0} = \sum_i \frac{\sigma_1(\phi_i)}{\sigma_0(\phi_i) + \lambda_0\sigma_1(\phi_i)} = \sum_i \frac{f(\phi_i)}{1 + \lambda_0 f(\phi_i)} = 0, \tag{A.14}$$

where $f = \sigma_1/\sigma_0$, and it is the same as the optimal observable given in Eq.A.12. Clearly, the likelihood $\mathcal{L}$ depends only on the optimal observable f. If the parameter λ_0 is small. we can obtain $\sum_i f_i(1 - \lambda_0 f_i) = 0$. Then, the following equation can be given:

$$\sum_i f_i = \lambda_0 \sum_i f_i^2 = \lambda_0 \int \left(\frac{\sigma_1}{\sigma_0}\right)^2 (\sigma_0 + \lambda\sigma_1) d\phi \simeq \lambda_0 \int \frac{\sigma_1^2}{\sigma_0} d\phi. \tag{A.15}$$

$$\langle\mathcal{O}\rangle = \frac{\sum_i f_i}{\sum_i} = \lambda_0 \frac{\int \frac{\sigma_1^2}{\sigma_0} d\phi}{\int \sigma(\phi) d\phi}. \tag{A.16}$$

Therefore, the likelihood fit method gives the same expression for the observable mean. This result indicates that these two methods are characterized by the same sensitivity.

Appendix B

$\boldsymbol{\tau}$ spin vector reconstruction formula

We consider the decay

$$\tau^{-(+)} \to \nu_\tau(\overline{\nu}_\tau) + \rho^{-(+)} \to \nu_\tau(\overline{\nu}_\tau) + \pi^{-(+)} + \pi^0 \,, \tag{B.1}$$

with coupling constants, particle momenta and polarization vector as shown in the Fig B.1.

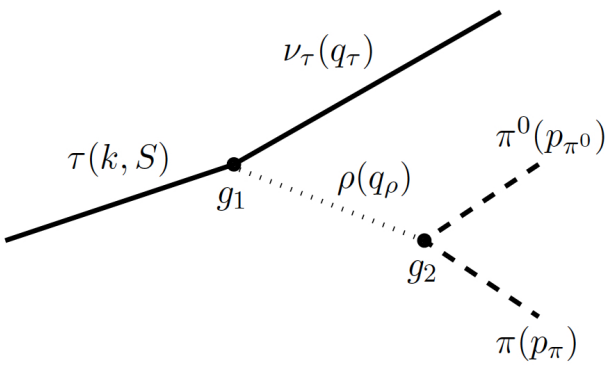

Figure B.1: Diagram of the $\tau^\pm \to \rho^\pm \nu_\tau \to \pi^\pm \pi^0 \nu_\tau$ decay. The notation for coupling constants, particle momenta and polarization vector used in the calculation are shown.

The corresponding Feynman amplitude is

$$\mathcal{M} = g_1\, \overline{u}(q_\tau)\gamma^\mu(1-\gamma_5)u_S(k)\, \frac{1}{D_\rho(q_\rho^2)}\, g_2\, p_\mu \,, \tag{B.2}$$

where $D_\rho(q_\rho) = q_\rho^2 - M_\rho^2 + i\Gamma_\rho M_\rho$ is the inverse propagator of the ρ vector

meson and: $q_\rho^\mu = (p_\pi + p_{\pi^0})^\mu$, $p_\mu = (p_\pi - p_{\pi^0})_\mu$. We introduce the spin-projection operator for the τ as

$$\mathcal{M} = g_1\, \overline{u}(q_\tau)\gamma^\mu(1-\gamma_5)\,\frac{1+\gamma_5 \not{S}}{2}\,u(k)\,\frac{1}{D_\rho(q_\rho^2)}\,g_2\,p_\mu\,, \tag{B.3}$$

with this form we are free to sum over all the spin polarizations to obtain the usual traces without loosing information about the τ polarization. Indeed we have

$$\begin{aligned}
|\mathcal{M}|^2 &= \frac{|g_1|^2\,|g_2|^2}{|D_\rho(q_\rho^2)|^2}\mathrm{Tr}\left[\not{q}_\tau\gamma^\mu(1-\gamma_5)\frac{1+\gamma_5\not{S}}{2}(\not{k}+m_\tau)\frac{1+\gamma_5\not{S}}{2}\gamma^\nu(1-\gamma_5)\right]p_\mu p_\nu \\
&= \frac{|g_1|^2\,|g_2|^2}{|D_\rho(q_\rho^2)|^2}\mathrm{Tr}\left[\not{q}_\tau\not{p}(1-\gamma_5)\frac{1+\gamma_5\not{S}}{2}(\not{k}+m_\tau)(1+\gamma_5)\not{p}\right] \\
&= \frac{|g_1|^2\,|g_2|^2}{|D_\rho(q_\rho^2)|^2}\mathrm{Tr}\left[\frac{1+\gamma_5\not{S}}{2}(\not{k}+m_\tau)(1+\gamma_5)\not{p}\not{q}_\tau\not{p}(1-\gamma_5)\right] \\
&= \frac{1}{2}\frac{|g_1|^2\,|g_2|^2}{|D_\rho(q_\rho^2)|^2}\Big\{\mathrm{Tr}\left[(\not{k}+m_\tau)(1+\gamma_5)\not{p}\not{q}_\tau\not{p}(1-\gamma_5)\right] + \\
&\qquad\qquad \mathrm{Tr}\left[\gamma_5\not{S}(\not{k}+m_\tau)(1+\gamma_5)\not{p}\not{q}_\tau\not{p}(1-\gamma_5)\right]\Big\} \\
&= \frac{1}{2}\frac{|g_1|^2\,|g_2|^2}{|D_\rho(q_\rho^2)|^2}\mathrm{Tr}\left[(\not{k}+m_\tau)(1+\gamma_5)\not{p}\not{q}_\tau\not{p}(1-\gamma_5)\right]\times \\
&\left\{1 + S^\mu\frac{\mathrm{Tr}\left[\gamma_5\gamma_\mu(\not{k}+m_\tau)(1+\gamma_5)\not{p}\not{q}_\tau\not{p}(1-\gamma_5)\right]}{\mathrm{Tr}\left[(\not{k}+m_\tau)(1+\gamma_5)\not{p}\not{q}_\tau\not{p}(1-\gamma_5)\right]}\right\}\,,
\end{aligned} \tag{B.4}$$

where $(1+\gamma_5\not{S})/2$ is idempotent and commutes with $\not{k}$. The first term is the unpolarized expression and the four-vector which multiplies S^μ is the **polarimeter four-vector** h_μ introduced in Eq. 1.14 of Chapter 2.

The trace at denominator is

$$
\begin{aligned}
&\mathrm{Tr}\left[(\not{k}+m_\tau)(1+\gamma_5)\not{p}\not{q}_\tau\not{p}(1-\gamma_5)\right] \\
&= \mathrm{Tr}\left[\not{k}\not{p}\not{q}_\tau\not{p}\right] \underbrace{-\mathrm{Tr}\left[\not{k}\not{p}\not{q}_\tau\not{p}\gamma_5\right] + \mathrm{Tr}\left[\not{k}\gamma_5\not{p}\not{q}_\tau\not{p}\right]}_{=8i\epsilon^{\alpha\beta\gamma\delta}k_\alpha p_\beta q_{\tau\gamma}p_\delta=0} \\
&\underbrace{-\mathrm{Tr}\left[\not{k}\gamma_5\not{p}\not{q}_\tau\not{p}\gamma_5\right]}_{=\mathrm{Tr}[\not{k}\not{p}\not{q}_\tau\not{p}]} + m_\tau \underbrace{\mathrm{Tr}\left[\not{p}\not{q}_\tau\not{p}\right]}_{=0} - m_\tau \underbrace{\mathrm{Tr}\left[\not{p}\not{q}_\tau\not{p}\gamma_5\right]}_{=0} \\
&+ m_\tau \underbrace{\mathrm{Tr}\left[\gamma_5\not{p}\not{q}_\tau\not{p}\right]}_{=0} - m_\tau \underbrace{\mathrm{Tr}\left[\gamma_5\not{p}\not{q}_\tau\not{p}\gamma_5\right]}_{=0} \\
&= 2\mathrm{Tr}\left[\not{k}\not{p}\not{q}_\tau\not{p}\right] \\
&= 8\left[2(kp)(q_\tau p) - (kq_\tau)p^2\right].
\end{aligned}
\tag{B.5}
$$

The trace at numerator has the same pieces but with an additional factor $\gamma_5\gamma^\mu$, and we have

$$
\begin{aligned}
&\mathrm{Tr}\left[\gamma_5\gamma^\mu(\not{k}+m_\tau)(1+\gamma_5)\not{p}\not{q}_\tau\not{p}(1-\gamma_5)\right] \\
&= \underbrace{\mathrm{Tr}\left[\gamma_5\gamma^\mu\not{k}\not{p}\not{q}_\tau\not{p}\right]}_{=0} - \underbrace{\mathrm{Tr}\left[\gamma^\mu\not{k}\not{p}\not{q}_\tau\not{p}\right]}_{=0} + \underbrace{\mathrm{Tr}\left[\gamma^\mu\not{k}\not{p}\not{q}_\tau\not{p}\right]}_{=0} \\
&\underbrace{-\mathrm{Tr}\left[\gamma^\mu\not{k}\not{p}\not{q}_\tau\not{p}\gamma_5\right]}_{=0} + m_\tau \underbrace{\mathrm{Tr}\left[\gamma_5\gamma^\mu\not{p}\not{q}_\tau\not{p}\right]}_{=4i\epsilon^{\mu\alpha\beta\gamma}p_\alpha q_{\tau\beta}p_\gamma=0} - m_\tau\mathrm{Tr}\left[\gamma^\mu\not{p}\not{q}_\tau\not{p}\right] \\
&- m_\tau\mathrm{Tr}\left[\gamma^\mu\not{p}\not{q}_\tau\not{p}\right] + m_\tau \underbrace{\mathrm{Tr}\left[\gamma^\mu\not{p}\not{q}_\tau\not{p}\gamma_5\right]}_{=4i\epsilon^{\mu\alpha\beta\gamma}p_\alpha q_{\tau\beta}p_\gamma=0} \\
&= -2m_\tau\mathrm{Tr}\left[\gamma^\mu\not{p}\not{q}_\tau\not{p}\right] \\
&= -8m_\tau\left[2(q_\tau p)p^\mu - p^2 q_\tau^\mu\right].
\end{aligned}
\tag{B.6}
$$

By using the previous results, the polarimeter four-vector is

$$
h^\mu = -m_\tau \frac{2(q_\tau p)p^\mu - p^2 q_\tau^\mu}{2(kp)(q_\tau p) - (kq_\tau)p^2}. \tag{B.7}
$$

The space component in the τ rest frame is

$$
\vec{h}' = -m_\tau \frac{2(q_\tau p)\vec{p}' - p^2\vec{q}_\tau'}{2(kp)(q_\tau p) - (kq_\tau)p^2}, \tag{B.8}
$$

where $\vec{p}\,'$ and $\vec{q}\,'_\tau$ stand for the space components of the corresponding four-vectors in this frame.

By exploiting the four-momentum conservation

$$q_\tau = k - p_\pi - p_{\pi^0}\,, \tag{B.9}$$

the scalar products

$$p(p_\pi + p_{\pi^0}) = (p_\pi + p_{\pi^0})(p_\pi - p_{\pi^0}) = 0\,, \quad \Longrightarrow \quad pq_\tau = pk\,, \tag{B.10}$$

and the four-vector (see Eq. 1.21 of Chapter 2)

$$H^\nu = 2(p_\pi - p_{\pi^0})^\mu \big[(p_\pi - p_{\pi^0})k\big] + (p_\pi + p_{\pi^0})^\mu p^2 = 2p^\mu(pk) + (p_\pi + p_{\pi^0})^\mu p^2\,,$$

the polarimeter four-vector becomes

$$\begin{aligned} h^\mu &= -m_\tau \frac{2(pk)p^\mu - p^2(k - p_\pi - p_{\pi^0})^\mu}{2(kp)^2 - \big[m_\tau^2 - k(p_\pi + p_{\pi^0})\big]p^2} \\ &= -m_\tau \frac{H^\mu - p^2 k^\mu}{2(kp)^2 + k(p_\pi + p_{\pi^0})p^2 - m_\tau^2 p^2} \\ &= -m_\tau \frac{H^\mu - p^2 k^\mu}{kH - m_\tau^2 p^2}\,, \end{aligned} \tag{B.11}$$

and the space component in the τ rest frame is ($\vec{k}\,' = 0$)

$$\vec{h}\,' = -m_\tau \frac{\vec{H}\,' - p^2 \vec{k}\,'}{kH - m_\tau^2 p^2} = -\frac{m_\tau \vec{H}\,'}{kH - m_\tau^2 p^2}\,. \tag{B.12}$$

The value, $\vec{h}$, of this three vector in a generic frame, as for instance that of the $\tau^+\tau^-$ pair, where the τ^- four momentum is $k = (E_\tau, \vec{k})$, with $\vec{k} \neq 0$, is related to that in the τ rest frame via the Lorentz transformations of a four-vector: $t = (t, \vec{t}\,) \to t' = (t'^0, \vec{t}\,')$, is

$$\begin{aligned} \vec{t}\,' &= \vec{t} + \frac{\gamma - 1}{\vec{\beta}^2}\left(\vec{\beta}\cdot\vec{t}\,\right)\vec{\beta} + \gamma\, t^0 \vec{\beta} \\ t'^0 &= \gamma\left(t^0 + \vec{\beta}\cdot\vec{t}\,\right) \end{aligned} \tag{B.13}$$

where, the boost is given by the actual four-momentum $k = (E_\tau, \vec{K})$, *i.e.*

$$\vec{\beta} = -\frac{\vec{k}}{k^0} = -\frac{\vec{k}}{E_\tau} \qquad \gamma = \frac{1}{\sqrt{1 - \vec{\beta}^2}} = \frac{E_\tau}{m_\tau}\,. \tag{B.14}$$

To verify these formulae we can use them for the τ four-momentum itself, to obtain the value in the rest frame starting from a generic frame, indeed we get

$$\begin{aligned}
\vec{k}\,' &= \vec{k} + \frac{E_\tau - m_\tau}{m_\tau \vec{k}^2/E_\tau^2}\left(\frac{\vec{k}^2}{E_\tau}\right)\frac{\vec{k}}{E_\tau} - \frac{E_\tau}{m_\tau}E_\tau\frac{\vec{k}}{E_\tau} = \vec{k} + \left(\frac{E_\tau}{m_\tau} - 1\right)\vec{k} - \frac{E_\tau}{m_\tau}\vec{k} = 0 \\
k'^0 &= \gamma\left(E_\tau - \frac{\vec{k}^2}{E_\tau}\right) = \frac{E_\tau}{m_\tau}\frac{E_\tau^2 - \vec{k}^2}{E_\tau} = m_\tau\,.
\end{aligned} \tag{B.15}$$

The boost of the $\vec{H}$ three-vector to $\vec{H}'$ of eq. (B.12)

$$\begin{aligned}
\vec{H}' &= \vec{H} + \frac{E_\tau/m_\tau - 1}{E_\tau^2 - m_\tau^2}\,\frac{E_\tau^2}{E_\tau^2}\,(\vec{k}\cdot\vec{H})\,\vec{k} - \frac{H^0\vec{k}}{m_\tau} \\
&= \vec{H} + \frac{(\vec{k}\cdot\vec{H})\,\vec{k}}{m_\tau(E_\tau + m_\tau)} - \frac{H^0\vec{k}}{m_\tau}\,,
\end{aligned} \tag{B.16}$$

and then

$$\vec{h} = -\frac{1}{kH - m_\tau^2 p^2}\left(-H^0\vec{k} + m_\tau\vec{H} + \frac{(\vec{k}\cdot\vec{H})\,\vec{k}}{E_\tau + m_\tau}\right)\,, \tag{B.17}$$

and using $\vec{S} = -\vec{h}$ we have

$$\vec{S} = \frac{1}{kH - m_\tau^2 p^2}\left(-H^0\vec{k} + m_\tau\vec{H} + \frac{(\vec{k}\cdot\vec{H})\,\vec{k}}{E_\tau + m_\tau}\right)\,. \tag{B.18}$$

The τ spin vector reconstruction formula for the case $\tau \to \rho\nu_\tau$ (Eq. 1.21) is now demonstrated. The procedure for the other τ decay channels is similar.

Appendix C

Boosted Decision Tree

The boosted decision tree is a machine learning technique widely used outwith particle physics [42]. The goal of decision trees is to extend the simple cut-based analysis into a multivariate technique by continuing to analyse events that fail a particular criterion. Mathematically, a decision tree is a sequence of binary operations (AND, OR) used to split the data into signal and background. Trees are trained using a set of known signal and background events (*training sample*) and tested using a separate set of data (*test sample*). The algorithm begins by considering all events to start on one node, the root node. All the events are then separated in turn into two children nodes - one most likely to be signal, the other mostly to be background - using the discriminating variable, taken from the variables set $\vec{x}$, which gives the best calculated separation value, or the splitting decision, for the given set of events. Events which pass the splitting decision are labelled as signal (S), while those which fail the decision are labelled as background (B). The algorithm is then applied recursively to these new nodes. The splitting stops when a given number of final nodes (called leaf nodes) are obtained, or until a node has too few events (quantity that can be set). The leaf nodes are classified as signal or background depending on the majority of events belonging to it, or its associated purity (signal fraction over the total training sample in this node). The most important part of the decision tree building process is determining the goodness of separation of signal and background events (the splitting criteria) and the optimal value at which to do this. An example of decision tree is shown in Fig.C.1.

A collection of decision trees is constructed using a procedure known as boosting. With boosting, the training events which where misclassified, i.e. a signal event falling on a background leaf or viceversa, have their weights increased (or boosted) and a new tree is formed. In this way many trees are build up, a forest of trees (the number of trees can be setted). The classifier

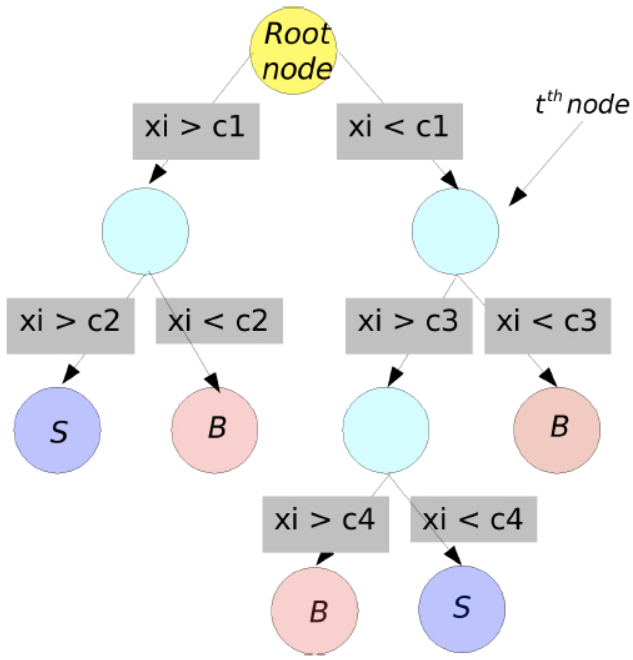

Figure C.1: Example of a decision tree. In each node a different splitting criteria between signal and background using a specific variable is applyed.

result for the ith tree is taken as $+1$ if the event falls on a signal leaf and -1 if the event fall on a background leaf. The final classifier result is then taken as a weighted sum of the individual trees.

The result of the training phase is the creation of weight files for each classifier which contains configuration options, controls and training weights. The trained classifiers are then applied to the test data, providing a scalar output upon which an event can be classified as either signal or background.

Bibliography

[1] M. Kobayashi and T. Maskawa. *Prog. Theor. Phys.*, **49**(652), 1973.

[2] B. Aubert et al. (Babar Collaboration). *Phys. Rev. Lett*, **87**(091801), 2001.

[3] K. Abe et al (Belle Collaboration). *Phys. Rev. Lett.*, **87**(091802), 2001.

[4] J. C. Schmidt B. C. Regan, E. D. Commins and D. Demille. *Phys. Rev. Lett.*, **88**(071805), 2002.

[5] K. Sangsterm D. Cho and E. A. Hinds. *Phys. Rev. Lett.*, **63**(2559), 1989.

[6] P. G. Harris et al. *Phys. Rev. Lett.*, **82**(904), 1999.

[7] J. Bailey et al. (CERN-Mainz-Daresbury Collaboration). *Nucl. Phys.*, **B150**(1), 1987.

[8] M. J. Booth. hep-ph/9301293.

[9] U. Mahanta. *Phys. Rev.*, **D54**(3377), 1996.

[10] B. H. J. McKellar K. G. He and S. Pakvasa. *Int. J. Mod. Phys*, **A4**(5011), 1989.

[11] M. Acciarri et al. (L3 Collaboration). *Phys. Lett.*, **B434**(169), 1998.

[12] K. Ackerstaff et al. (OPAL Collaboration). *Phys. Lett.*, **B431**(188), 1998.

[13] H. Albrecht et al. (ARGUS Collaboration). *Phys. Lett.*, **B485**(37), 2000.

[14] D. Atwood and A. Soni. *Phys. Rev.*, **D45**(2405), 1992.

[15] K. Inami et al. (Belle Collaboration). *Phys. Lett.*, **B551**(16-26), 2003.

[16] W. Bernreuther and O. Nachtmann. *Phys. Rev. Lett.*, **63**(2789), 1989.

[17] Y. L. Wu and L. Wolfenstein. *Phys. Rev. Lett.*, **73**(1762), 1994.

[18] A. Soni and R. M. Xu. *Phys. Rev. Lett.*, **69**(33), 1992.

[19] W. Lu T. Huang and Z. Tao. *Phys. Rev.*, **D55**(1643), 1997.

[20] A. Brandenburg W. Bernreuther and P. Overmann. *Phys. Lett.*, **B391**(413), 1996.

[21] A. Brandenburg W. Bernreuther and P. Overmann. *Phys. Lett.*, **B412**(425), 1997.

[22] W. Buchmuller and D. Wyler. *Nucl. Phys.*, **B268**(621), 1986.

[23] S. T. Love C. N. Leung and S. Rao. *Z. Phys.*, **C31**(433), 1986.

[24] M. S. Bilenky and A. Santamaria. *Nucl. Phys.*, **B420**(47), 1994.

[25] J. Vidal G.A.Gonzalez-Sprinberg, A. Santamaria. *Nucl. Phys.*, **B582**(3), 2000.

[26] G. A. González-Sprinberg J. Bernabéu and Jordi Vidal. hep-ph/0211249v1. 2002.

[27] G. A. González-Sprinberg J. Bernabéu and J. Vidal. hep-ph/0404185v2. 2004.

[28] O. Nachtmann W. Bernreuther and P. Overmann. *Phys. Rev.*, **D48**(78), 1993.

[29] S. Jadach B. F. L. Ward and Z. Was. *Nucl. Phys. Proc.*, **347 Suppl. 116**(73), 2003.

[30] S. Jadach et al. *Comput. Phys. Commun.*, **76**(361), 1993.

[31] M. Davier et al. *Phys. Lett.*, **B306**(411), 1993.

[32] Y. Tsai. *Phys. Rev.*, **D4**(2821), 1971.

[33] J.H. Kuhn S. Jadach and Z. Was. *Comput. Phys. Commun.*, **64**(275), 1991.

[34] Simone Pacetti. *Private communication.*

[35] B. Aubert et al. (Babar Collaboration). *Nucl. Instr. and Method*, **A479**(1), 2002.

[36] PEP II. - an asymmetric b factory, conceptual design report. *SLAC-418, LBL-5379*, 1993.

[37] M. H. Kelsey et al. *Nucl. Instr. and Method*, **A536**(206), 2004.

[38] I. Adam et al. *SLAC-PUB-8783*, 2001.

[39] B. Lewandowski et al. *Nucl. Instr. and Method*, **A494**(302), 2002.

[40] F. Anulli et al. *Nucl. Instr. and Method*, **A409**(542), 1998.

[41] W. Menges. The *BABAR* muon system upgrade. *IEEE Nucl. Sci. Symp. Conf. Rec.*, **5**(1470-1474), 2006.

[42] A. Hoecker et al. Tmva 4 user guide. *Data Analysis, Statistics and Probability*, arXiv:physics/0703039, 2009.

[43] Babar Collaboration. *Babar Physics Book*, SLAC-R-504, 1998.

[44] C. Touramanis et al. *Babar Analysis Document*, **n. 229**.

[45] D. j. lange. *Nucl. Instr. and Method.*, **A462**(152-155), 2001.

[46] Stephen Mrenna Torbjorn Sjostrand and Peter Skands. Pythia 6.4 physics and manual. hep-ph/0603175, 2006.

[47] P. Golonka et al. *Comput. Phys. Commun.*, hep-ph/0312240, 2006.

[48] S. Agostinelli et al. *Nucl. Instr. and Method.*, **A506**(250-303), 2003.

[49] Swagato Banerjee et. al. Cm2 skims for $e^+e^- \to \mu^+\mu^+$ and $e^+e^- \to \tau^+\tau^+$ events (tauqed2). *Babar Analysis Document*, **n. 760**(Version 1), 2003.

[50] Swagato Banerjee et. al. Nano and micro level selection for $e^+e^- \to \mu^+\mu^+$ and $e^+e^- \to \tau^+\tau^+$ events. *Babar Analysis Document*, **n. 739**(Version 2), 2003.

[51] Pierre Billoir. *Nucl. Instr. and Method*, **A225**(352-366), 1984.

[52] I. Narsky. Optimization of signal significance by bagging decision tree. arXiv:physics/0507157.

[53] Piti Ongmongkolkul. New km selector. http://www.slac.stanford.edu/BFROOT/www/Organization /CollabMtgs/2008/detOct08/Tues2b/piti.pdf.

[54] Thomas G. Dietterich and Ghulum Bakiri. Solving multiclass learning problems with error-correcting output codes. *Journal of Artificial Intelligence Research*, **2**(263-286):http://www.jair.org/media/105/live–105–1426–jair.pdf, 1995.

[55] Piti Ongmongkolkul et al. Particle identification using error correction output code multiclass classifier. *Babar Analysis Document*, **n. 2199**(Version 3), 2011.

[56] A.V. Telnov C.O. Vuosalo and K.T. Flood. Muon identification using decision tree. *Babar Analysis Document*, **n. 1853**(Version 3), 2010.

[57] J. Beringer et al. *(Particle Data Group), Phys. Rev*, **D86**(010001), 2012.

[58] R. Sinkus and T. Voss. *Nucl. Instr. and Method*, **A391**(360), 1997.

[59] Z. Was Z. Czyczula, T. Przedzinski. Tauspinner program for studies on spin effect in tau production at the lhc. *arXiv:1201.0117 [hep-ph]*, 2012.

Acknowledgment

Grazie a Giuseppe Finocchiaro per il contributo che ha avuto in questo lavoro, per l'ironia con cui mi tratta e per la pazienza.

Grazie a Riccardo de Sangro, Ida Peruzzi e Marcello Piccolo. Grazie a Ida per aver ottenuto da Simone Pacetti le formule di ricostruzione di spin. Grazie a Simone per averle calcolate e per aver discusso insieme a me. Grazie davvero a Riccardo, non solo per aver partecipato al mio lavoro, ma anche per avermi sostenuto in tutti i collaboration meetings, da Ferrara a SLAC, occupandosi di me. Grazie a tutte le persone che mi hanno scarrozzato per la California: Matteo Rama, Alessandro Pilloni, Eugenia Puccio, Andrea Dotti. Grazie anche a Nicola Neri, Gabriele Simi e Alessandra Filippi per la gita in bici sul Golden Gate. Grazie a Tina Cartaro, con Antonio e Pietro, per la loro accoglienza ed ospitalità. Grazie ad Isabella Garzia per aver risposto con pazienza a tutte le mie domande.

I would like to thank you all the people that kindly answer to my copious email giving a contribution to my Babar analysis work: Abi Soffer, Swagato Banerjee, Aleksandra Adametz, Matt Bellis, Bipul Bhuyan, Francesco Renga, Riccardo Faccini, Tina Cartaro, David Brown, Marcello Rotondo, the *BABAR* spokesman Michael Roney, and especially Benjamin Oberhof. Thank you very much to Ian M Nugent for the TauSpinner suggestion.

Grazie infinite ad Alberto Lusiani per aver seguito il mio lavoro ed avermi dato sempre il consiglio giusto al momento giusto. Grazie al PAC Fabio Anulli. A lui un grazie particolarmente intenso, per avermi fatto conoscere la California ed avermi aiutato e seguito con la sua gentilezza, per essere stato presente al mio esame interno di dottorato.

Grazie a Claudio Gatti per avermi dato l'occasione di partecipare agli stage estivi. Grazie al mio *padre scientifico* Riccardo Faccini per avermi formato, prendendo le mie conoscenze e restituendomi una professione, grazie perché continua a preoccuparsi di me. Grazie anche a Fernando Ferroni, perché so che mi sorveglia. Grazie a Carlo Dionisi per avermi incoraggiato mentre ritiravo il premio della SIF.

Grazie al gruppo pranzo *mmm buono*: Barbara, Tommaso, Emiliano,

Danilo, Ricci e Matteo, per la loro costante partecipazione. Grazie a Flavio Archilli per i consigli, tecnici e non. Grazie ad Alessio Sarti per le risposte sul codice nella chat del pranzo. Grazie ad Antonio Castelli e Valerio Ippolito per avermi risposto da qualsiasi luogo e a qualsiasi ora a tutte le mie domande su root. Grazie a Valerio Bortolotto per la lezione privata sulle BDT.

Grazie a Filippo Ceradini e a Roberto Tenchini per aver letto questa tesi con cura.

Grazie a Emiliano che la stamperà e a Vale che la consegnerà e grazie a Lollo che la caricherà sul sito, a lui grazie anche per aver condiviso con me questi tre anni. Grazie ancora a Giancarlo Piredda per il sostegno e i consigli preziosi. Grazie a mio padre per esserci sempre. Nonostante le ansie che gli procuro e quelle che mi trasmette, gli sono debitrice. Grazie a mia madre perchè riesce a farmi distrarre, ribaltando a modo suo la gerarchia delle priorità. Grazie agli amici, sempre presenti quando ne ho bisogno e che si fanno in quattro per me.